Effectiveness Factor of Thin-Layer IrO$_2$ Electrocatalyst: Influence of Catayst Loading and Electrode Kinetics

THÈSE N^O 4181 (2008)

PAR

Erika HERRERA CALDERON

Master M.G.P. Spécialité Électrochimie, Institut National Polytechnique de Grenoble, St-Martin d'Hères, France
et de nationalité Mexicaine

EPFL

ÉCOLE POLYTECHNIQUE
FÉDÉRALE DE LAUSANNE

Suisse
2008

Abstract

Dimensionally Stable Anodes (DSA$^{®}$) are electrodes composed of a metal support and an oxide coating (catalyst). Particularly in this thesis, the Ti/IrO$_2$ electrode was used for the study of the fraction of the surface which participates effectively in the investigated reactions (effectiveness factor, E_f). Four reactions with different kinetics have been investigated: (a) Fe^{3+}/Fe^{2+} (fast reaction), (b) O$_2$ and (c) Cl$_2$ evolutions (slow reactions), and (d) isopropanol oxidation (complex reaction involving redox catalysis). This study has allowed us to apply for the first time in electrocatalysis the term, effectiveness factor, E_f, used before in other fields like in heavy metals recovery with 3D electrodes and in heterogeneous catalysis.

On the other hand, in order to achieve the main objective of this thesis, an analytical and a qualitative approach was proposed. Furthermore, the Ti/IrO$_2$ electrodes were characterized electrochemically using the cyclic voltammetry (CV) technique in which the voltammetric charge was measured at different potential scan rates, potential windows, and electrolyte temperatures using various Ti/IrO$_2$ loadings. From the voltammetric charge, two contributions were found. The first contribution is related to the double layer capacitance and the second with the redox couples present on the electrode surface.

The first reaction investigated in this work was the Fe^{3+}/Fe^{2+} redox couple. In the first part of the investigation of this reaction, the CV technique was used; however, some issues related to the uncompensated electrolyte resistance were encountered. Therefore the effectiveness factor for this particular case was not possible to obtain. On the other hand, using rotating Ti/IrO$_2$ disk electrodes (RDE) for the same reaction, the effectiveness factor, E_f, has been estimated, however, this value is much lower than the predicted one.

The other investigated reactions in this work were O$_2$ and Cl$_2$ evolutions. The investigated kinetics of both reactions showed that the evolution of chlorine is much faster than that of oxygen. The effectiveness factor, E_f, for the oxygen evolution was close to the unity for all IrO$_2$ loadings, contrary to the chlorine reaction that decreased with the loading. This behaviour was predicted according to what is given in the analytical approach.

The last reaction investigated in this work was the oxidation of isopropanol. In this case a model was proposed based on three main reactions: Electrochemical IrO_2 oxidation to IrO_3, chemical oxidation of isopropanol via IrO_3, and chemical decomposition of IrO_3 to IrO_2. The effectiveness factor, for the electrochemical reaction seemed not to correlate with the loading, whereas for the chemical one, it diminished with the loading.

Résumé

Les anodes dimensionnellement stables (Dimensionally Stable Anodes (DSA®)) sont des électrodes composées d'un substrat métallique et d'une couche d'oxyde (catalyseur). Dans cette thèse, l'électrode Ti/IrO$_2$ a été utilisée pour l'étude de la fraction de surface qui participe activement dans les réactions étudiées (facteur d'efficacité, E_f). Quatre réactions de différente cinétique ont été examinées: (a) Fe^{3+}/Fe^{2+} (réaction rapide), (b) évolution d'O$_2$ et (c) du Cl$_2$ (réactions lentes), et (d) oxydation d'isopropanol (réaction complexe avec catalyse redox). Cette étude nous a permis d'appliquer pour la première fois en électrocatalyse le terme de facteur d'efficacité, E_f, utilisé avant dans d'autres domaines comme dans la récupération des métaux lourds par des électrodes 3D et dans la catalyse hétérogène.

D'un autre côté, afin d'atteindre l'objectif principal de cette thèse, une approche analytique et qualitative a été proposée. En outre, les électrodes Ti/IrO$_2$ ont été caractérisées en utilisant la technique de voltamétrie cyclique (VC) dans laquelle la charge voltamétrique a été présentée pour différentes vitesses de balayage, fenêtres de potentiel, et de températures d'électrolyte en utilisant plusieurs électrodes Ti/IrO$_2$ avec un dépôt de masse d'IrO$_2$ différente. De la part de la charge voltamétrique, deux contributions ont été constatées. La première contribution a été liée à la capacité de la double couche et la seconde, à la présence des couples redox à la surface de l'électrode.

La première réaction examinée dans ce travail est celle du couple redox Fe^{3+}/Fe^{2+}. Dans la première partie de l'étude de cette réaction, la technique de VC a été utilisée; cependant, quelques problèmes reliés à la décompensation de la résistance de l'électrolyte ont été rencontrés. Par conséquent, le facteur d'efficacité dans ce cas, n'a pas pu être obtenu. Au contraire, lorsque des électrodes de Ti/IrO$_2$ tournantes à disque (RDE) pour la même réaction ont été utilisées, le facteur d'efficacité, E_f, a pu être estimé; toutefois, la valeur est plus basse que celle prédite.

Les autres réactions examinées dans ce travail étaient celles de l'évolution d'O$_2$ et Cl$_2$. La cinétique de ces deux réactions a montré que la réaction de l'évolution du chlore est beaucoup plus rapide que celle de l'oxygène. Le facteur d'efficacité, E_f, pour l'évolution

d'oxygène était proche de l'unité pour toutes les électrodes de différentes masses déposées, au contraire de la réaction du chlore qui, elle, a diminuée avec la masse déposée. Ce comportement était prévu selon l'approche analytique donnée.

La dernière réaction étudiée dans ce travail était l'oxydation de l'isopropanol. Dans ce cas, un modèle a été proposé selon la base de trois réactions principales: Oxydation électrochimique d'IrO_2 en IrO_3, oxydation chimique de l'isopropanol via IrO_3, et la décomposition chimique de l'IrO_3 en IrO_2. Le facteur d'efficacité pour la réaction électrochimique ne présente aucune corrélation avec la masse déposée d'IrO_2, tandis que la réaction chimique, elle, diminue.

Mots-clés: Ti/IrO_2, charge voltamétrique, surface réelle, facteur d'efficacité, facteur de rugosité.

Acknowledgments

<div align="right">

To God
To my mother, grandmother,
my brothers and sisters-in-law and my family
To my love Jochen
To my friends from all around the world…

</div>

First of all I would like to give my special thanks to Prof. Comninellis for having accepted me as a PhD student in his group as well as Prof. Rolf Wüthrich and Dr. György Fóti for having guided me from the end until the end of this PhD work. Their continuous support, time, encouragement, and suggestions have guided me to get through with my research. I deeply appreciate their precious time they offered me for discussions which often cleared up my mind to continue.

Thanks to all the jury members: Prof. M.-O. Hongler, Prof. V. Stankovic, Dr. Ph. Mandin, Dr. W. Harbich, for having accepted to be part of the jury members as well as to read and evaluate my PhD work.

To Mme. Ingrid Margot and Mme. Evelyne Toubes for their help in all the administrative work.

Special thanks to the entire mechanic group, Pap and Edi for their technical support as well as their funny moments.

Another special thanks to Johnny Nussbaumer and Alexandros Katsaounis for their great contribution in my PhD research. Special thanks to Cesar Pulgarin for his nice advices and friendship.

Table of contents

X

List of symbols

Roman symbols

Symbol	Meaning	Usual units	Section references
a	(a) Specific electrode surface area	(a) 1/cm	(a) 3.4.1
	(b) Volume specific pore surface area	(b) 1/cm	(b) 10.1
	(c) Tafel constant	(c) V	(c) 7.2b
a_p	Specific particle area	1/cm	3.2-I.A, 3.5, 4.3.1, 6.4.2
a_{sp}	Specific surface area	cm^2/mg	4.3.3, 4.3.4, 6.4.2
A	(a) Electroactive species A	(a) –	(a) 3.3a, b
	(b) Geometric surface area	(b) cm^2	(b) 3.4.1c, 5.3.3, 6.4.1
A_g	(a) Geometric (projected) area	(a) cm^2	(a) 3.1, 4.3.4, 8.3
	(b) Cross-section of the differential element	(b) cm^2	(b) 3.2.1, 3.2.2
A_p	Internal pore surface area	cm^2	10.1
A_w	Real (wetted) surface area	cm^2	3.1, 4.3.4, 8.3
b	Tafel slope	V/dec	7.2b
c	Surface concentration	M, mol/cm^3	10.1
c^*	Bulk concentration of electroactive species	M, mol/cm^3	10.1
C	Concentration of electroactive species	M, mol/cm^3	5.3.2, 6.4.1

Symbol	Meaning	Usual units	Section references
C_A	Concentration of electroactive species A in the bulk of the electrolyte	M, mol/cm^3	3.3a, b, 3.4.1c, 3.5
$\overline{C_A}$	Average concentration of electroactive species A	M, mol/cm^3	3.3
$C_A(0)$	Concentration of electroactive species A at the Ti substrate	M, mol/cm^3	3.3
$C_A(1)$	Concentration of electroactive species A in the electrolyte	M, mol/cm^3	3.3
C_{ox}	Dimensionless concentration of species ox	–	10.1
C_{ads}	Adsorption capacitance	µF/cm^2	4.1
C_{ISP}^{ad}	Concentration of the adsorbed isopropanol at the surface of the electrode	M, mol/cm^3	8.3
C_{ISP}^{bulk}	Concentration of isopropanol in the bulk of the electrolyte	M, mol/cm^3	8.3
C_{dl}	Double-layer capacitance	µF/cm^2	4.1
C_{irr}	Irreversible redox surface capacitance	µF/cm^2	4.1
C_{red}	Dimensionless concentration of species red	–	10.1
d	a) Diameter of the cylindrical pores b) Atomic distances	(a) cm (b) Å	(a) 3.2.2, 3.5 (b) 4.3.1b, appendix chapter 4
d_p	Diameter of particle	cm	3.2, 4.3.1, 4.3.4, 6.4.2
D_A; $D_{Fe^{2+}}$	Diffusion coefficient of the electroactive species A; Fe^{2+} within the DSA® coating	cm^2/s	3.3, 3.4.1, 3.5

Symbol	Meaning	Usual units	Section references
D_{eff}	Effective pore diffusion coefficient of the electroactive species inside the porous electrode	cm^2/s	3.4.1, 3.4.2, 4.3.2c, 10.1, 10.2
E	Potential	V	6.4.1
E_a^{app}	Apparent activation energy	kJ/mol	4.3.2b
E_a^{eff}	Effective activation energy	kJ/mol	4.3.2c
ΔE	Characteristic potential difference used in the CV measurements: (a) If well defined anodic and cathodic peaks (if one electron reversible redox couple): $\Delta E = RT / F$ (b) Potential difference between the onset potential of the redox couple and the potential of peak current appearance (c) Potential window used in the voltammetric charge measurement (d) Potential drop between the working and reference electrode	(a) V (b) V (c) V (d) V	(a) 3.4.1a (b) 3.4.1a (c) 3.4.1a, 3.4.2, 4.3.2c (d) 6.3.2
ΔE_p	Potential difference between the anodic and cathodic potentials (E_{pa} and E_{pc}), respectively	V	5.3.2

Symbol	Meaning	Usual units	Section references
E_{eq}	Equilibrium potential	V	3.2
E_f	Effectiveness factor	-	Chapters 1-9
$E_f^{rel.}$	Relative effectiveness factor with respect to the lowest loading taken as reference	-	7.3, 7.3.1b, 7.3.2b
$(E_f^{rel.})_{chem.}$	Relative effectiveness factor for the chemical oxidation of the adsorbed isopropanol	-	8.3
$(E_f^{rel.})_{elect.}$	Relative effectiveness factor for the electrochemical oxidation of surface IrO_2 to IrO_3 via hydroxyl radicals	-	8.3
E_ℓ	Denotation of the electrodes loading	mg IrO_2/cm^2	4.2a
E^0	Standard potential of the IrO_3/IrO_2 couple	V	8.3
f	$\dfrac{F}{RT}$	1/V	5.3.2
F	Faraday constant	C/mol	3.2, 3.3b, 3.4.1c, 3.5, 5.3.2, 6.4.1, 6.4.2, 8.3
G^{ext}	Dimensionless current density produced at the external electrode-electrolyte interface	-	10.1
G^{int}	Dimensionless current density produced inside the porous electrode	-	10.1
G^{tot}	Dimensionless total current density	-	10.1
h	Depth of the Ti substrate circular slot	mm	4.2a

Symbol	Meaning	Usual units	Section references
I	Current	A	6.4.1, 7.2b, 7.3.1a, 7.3.2a
I_{lim}	Limiting current	A	6.4.1
$I_{lim,\,a}$	Anodic limiting current	A	6.4.1
$I_{lim,\,c}$	Cathodic limiting current	A	6.4.1
I_p	Peak current	A	3.4.1c, 10.2
I_{pa}	Anodic peak current	A, mA	5.3.3
$I_s(x)$	Local current within the differential element	A	3.2.1, 3.2.2
j	Current density	A/cm^2	3.2-III, 3.3b, 3.4.1c, 8.3
j^{ext}	Current density produced at the external electrode-electrolyte interface	A/cm^2	10.1
j^{int}	Current density produced inside the porous electrode	A/cm^2	10.1
j^{tot}	Total current density	A/cm^2	10.1
j_0	Exchange current density	A/cm^2, mA/cm^2	3.2-III, 3.2.1, 3.2.2, 3.5, 5.3.2, 6.4.1, 6.4.2, 7.3.1, 7.3.2
$(j_0)_{2D}$	Exchange current density measured with a polished Pt electrode (two dimensional, 2D)	A/cm^2	5.3.2, 6.4.2, 7.3

Symbol	Meaning	Usual units	Section references
$(j_0)_{3D}$	(a) Exchange current density (referred to 1cm^2 projected area) measured for a three dimensional (3D) IrO$_2$ electrode with a given loading (b) Average exchange current density in rotating disk electrode experiments	(a) A/cm^2 (b) A/cm^2	(a) 5.3.2, 7.3.1, 7.3.2 (b) 6.4.2
$(j_0)_{3D}^{ref}$	Exchange current density of the reference 3D (lowest loading)	A/cm^2	7.3
J_A	Flow of the active species A within the pore	mol/cm^{2}s	3.3a
k_c	Chemical rate constant	cm^3/mols	8.3
$(k_c)_{app}$	Apparent chemical rate constant	cm/s	8.3
$(k_c)_{app}^{ref}$	Apparent chemical rate constant for the lowest specific loading taken as reference	cm/s	8.3
k_d	Decomposition rate constant of the higher oxide IrO$_3$	1/s	8.3
k_e	Electrochemical rate constant	cm/s	3.3a, 3.4.1c, 3.5
k_1^e	Electrochemical rate constant for the forward reaction of oxidation of surface IrO$_2$ to IrO$_3$ via hydroxyl radicals	1/s	8.3

Symbol	Meaning	Usual units	Section references
k_{-1}^{e}	Electrochemical rate constant for the backward reaction of oxidation of surface IrO_2 to IrO_3 via hydroxyl radicals	1/s	8.3
$(k_1^{e,0})_{app}$	Apparent electrochemical standard rate constant	mol/cm^2s	8.3
$(k_1^{e,0})_{app}^{ref}$	Apparent electrochemical standard rate constant for the lowest specific IrO_2 loading taken as reference	mol/cm^2s	8.3
k^0	Standard electrochemical rate constant	cm/s	3.3b, 3.4.1c, 5.3.2, 6.4.2
K_1^2	Dimensionless number that includes parameters of morphology, apparent electrolyte conductivity, and kinetics of a reaction in the spherical particle configuration (SPC)	-	3.2.1, 6.4.2, 7.1, 7.3.1, 7.3.2
K_2^2	Dimensionless number that includes parameters of morphology, apparent electrolyte conductivity, and kinetics of a reaction in the cylindrical pore configuration (CPC)	-	3.2.2
L	Thickness of the coating	μm, cm	3.2-I-A, I-B, 3.2.1, 3.2.2, 3.3b, 3.4.1b, c, 3.4.2, 3.5, 4.3.2c, 4.3.4, 6.4.2, 7.2a, 7.3.1b, 7.3.2b, 10.1, 10.2

Symbol	Meaning	Usual units	Section references
L_{sp}	Specific length of the cracks per unit surface	1/cm	4.3.1a
m	Thiele modulus (dimensionless)	-	3.3, 3.5
m_{sp}	Specific loading	mg IrO_2/cm^2	4.3.3, 4.3.4, 5.3.2, 6.4.2, 7.2a, 7.3.1a, b, 7.3.2a, b, 8.3
m_{sp}^{ref}	Specific loading of the reference 3D electrode (lowest loading)	mg IrO_2/cm^2	7.3, 8.3
M	(a) Metal (b) Sum of two constants defined by limiting conditions	(a) - (b) -	(a) 2.1.3, 3.2-III, 8.1 (b) 3.2.1, 3.3
M_1	First constant defined by two limiting conditions	-	3.2.1, 3.3
M_2	Second constant defined by two limiting conditions	-	3.2.1, 3.3
n	Number of exchanged electrons in an electrochemical reaction	-	5.3.3, 8.3
N_p	Number of pores per cm^2	1/cm^2	3.2.2, 3.5, 10.1
p	Dimensionless potential	-	10.1
q^*	Voltammetric charge	mC/cm^2	4.3.2b, c
q^+	Anodic charge	mC, mC/cm^2	4.3.2a, 4.3.3
q^-	Cathodic charge	mC, mC/cm^2	4.3.2a, 4.3.3
q_{dl}^*	Double-layer charge	mC/cm^2	4.3.2c, 4.3.3
q_{redox}^*	Surface redox charge	mC/cm^2	4.3.2c, 4.3.3

Symbol	Meaning	Usual units	Section references
q_{sp}^*	Specific charge	mC/mg	4.3.3
r	(a) Radius of the particles (b) Electrochemical rate (c) Rotating disk electrode radius	(a) cm (b) mol/cm^{2}s (c) cm	(a) 3.2-I-A (b) 3.3b, 3.4.1c, 8.3 (c) 6.3.2
$r_{dec.}$	Rate of decomposition of surface IrO_3 to oxygen	mol/cm^{2}s	8.3
$r_{oxid.}$	Rate of the chemical oxidation of isopropanol by IrO_3	mol/cm^{2}s	8.3
R	(a) Molar gas constant (b) Apparent electrolyte resistance	(a) J/molK (b) Ω	(a) 3.2-III, 3.3b, 3.4.1c, 5.3.2, 6.4.1, 6.4.2 (b) 3.2.1
R_u	Uncompensated resistance between the working and reference electrode	Ω	5.3.2, 6.3.2, 7.2b, 7.3.1a, 7.3.2a
R_{ct}	(a) Charge-transfer resistance (b) Charge-transfer resistance	(a) Ωcm^2 (b) Ω	(a) 3.2.1, 3.2.2, 3.5, 6.4.2, 7.3.1b, 7.3.2b (b) 3.3
R_{ex}	External film resistance	Ω	3.3
R_p	Internal pore resistance	Ω	3.3
R_Ω	Ohmic resistance	Ωcm^2	3.2.1, 3.2.2, 3.5, 6.4.2, 7.3.1b, 7.3.2b
S	Active site	-	7.3.1a
S_p	Surface of one particle	cm^2	3.2, 4.3.4, 6.4.2
t	Time	s	10.1, 10.2

Symbol	Meaning	Usual units	Section references
T	(a) Temperature	(a) K; °C	(a) 3.2-III, 3.2.1, 3.2.2, 3.3b, 3.4.1c, 3.5, 6.4.1, 6.4.2, 7.2b, 8.3; 4.3.2b, c, 5.3.2, 6.3.2
	(b) Dimensionless time	(b) -	(b) 10.1
ΔT	Time discretization step	-	10.1
V_p	Volume of one particle	cm^3	3.2, 4.3.4, 6.4.2
V_{total}	Total volume	cm^3	3.2-I-A
V_{void}	Void volume of the coating	cm^3	3.2-I-A
x	Distance	cm	3.2-I-A, B, 3.2.1, 3.2.2, 3.3
Δx	Differential element	-	3.2.1, 3.2.2
ΔX	Space discretization step	-	10.1
X	Dimensionless distance	-	3.2-I-A, B, 3.2.1, 3.2.2, 3.3, 3.5, 10.1

Greek symbols

Symbol	Meaning	Usual units	Section references
α	Transfer coefficient	-	3.2-III, 3.3b, 3.4.1c, 8.3

Symbol	Meaning	Usual units	Section references
γ	(a) Apparent electrolyte conductivity (b) Dimensionless parameter related to the voltammetric measurement and the internal diffusion	(a) $1/\Omega$cm (b) -	(a) 3.2-II, 3.5 (b) 3.4.1c, 3.4.2, 10.1, 10.2
γ_{2D}	Roughness factor of a 2D electrode	-	6.4.1
γ_{3D}	Three-dimensional roughness factor	-	4.3.3, 4.3.4, 5.3.2, 6.4.2, 7.3, 7.3.1a, 8.3
γ_0	Bulk electrolyte conductivity	$1/\Omega$cm	3.2-II, 3.2.1, 3.2.2, 6.3.2, 6.4.2
δ	Diffusion layer thickness	μm	6.3.2
Γ_0	Density of IrO_2 active surface sites	mol/cm^2	8.3
ε	Void fraction of the electrode	-	3.2-I-A, 3.2-II, 3.2.1, 3.5, 4.3.1a, 4.3.4, 6.4.2, 7.2a
η	Overpotential	V	3.2-III, 3.3b, 3.4.1c
$\eta(x)$	Local overpotential at x	V	3.2.1, 3.2.2
$\eta(0)$	Overpotential at the Ti substrate position	V	3.2.1, 3.2.2, 3.5
$\eta(1)$	Overpotential in the electrolyte	V	3.2.1, 3.2.2, 3.5
$\bar{\eta}$	Average overpotential	V	3.2.1, 3.2.2
η_{corr}	Correction of the experimental overpotential	V	7.2b

Symbol	Meaning	Usual units	Section references
$\Delta\eta / \Delta I$	Derivative calculated from each pair of two consecutive experimental points	V/A	7.2b, 7.3.1a, 7.3.2a
Θ	Fraction of surface sites covered by IrO_3	-	8.3
λ	a) Dimensionless parameter related to the charge transfer reaction and the internal diffusion (b) Ionic concentration	(a) - (b) mol/cm^3	(a) 3.4.1c (b) Appendix chapter 6
λ'	Dimensionless parameter related to the charge transfer reaction and the internal diffusion (modified)	-	10.1
μ	Dimensionless parameter: $\mu = a \cdot L$	-	10.1
ν	Kinematic viscosity	cm^2/s	6.4.1
ρ	Bulk density of IrO_2	g/cm^3	4.3.4, 6.4.2
τ	Typical time constant	-	10.1
$\tau_{int.diff.}$	Time constant related to the internal pore diffusion	s	3.4.1b, c
$\tau_{react.}$	Time constant related to the charge transfer reaction	s	3.4.1c
$\tau_{volt.}$	Time constant related to the voltammetric measurements	s	3.4.1a, c
υ	Scan rate	V/s	3.4.1a, 3.4.2, 4.3.2a, b, c, 4.3.3, 5.3.2, 5.3.3
ø	Diameter of the circular slot of the electrode	mm	4.2a

Symbol	Meaning	Usual units	Section references
χ	Tortuosity	-	10.1
ψ	Related to ΔE_p	mV	5.3.2
ω	Angular velocity	1/s	6.4.1

Standard abbreviations

Symbol	Meaning	Usual units	Section references
ASTM	American Standards for Testing and Materials	-	4.3.1b, appendix chapter 4
CE	Counter electrode	-	4.2c
CPC	Cylindrical pore configuration	-	3.2-B, 3.2.2, 3.3, 6.4.2
CV	Cyclic voltammetry	-	3.4.1, 4.2c, 4.3.2a, 4.3.3, 5.1, 5.3.1, 2
DEMS	Differential electrochemical mass spectroscopy	-	2.1.3, 7.3.1a
DSA®	Dimensionally Stable Anodes	-	Chapters 1-9
EASA	Electrochemical active surface area	cm^2/mg	2.2, 4.3.3
HRSEM	High Resolution Scanning Electron Microscopy	-	4.3.1a
ISP	Isopropanol	-	8.3
HRSEM	High Resolution Scanning Electron Microscopy	-	4.3.1a
LSV	Linear Sweep Voltammetry	-	5.3.3
MSE	Mercurous sulfate electrode	-	4.2c, 4.3.2a, 4.3.3, 5.2, 5.3.1, 5.3.3, 6.4.1, 7.2a
RDE	Rotating disk electrode	-	6.3.1
rds	Rate-determining step	-	7.3.1a
RE	Reference electrode	-	4.2c

SHE	Standard hydrogen electrode	-	4.2c
SPC	Spherical particle configuration	-	3.2-A, 3.2.1, 6.4.2
WE	Working electrode	-	4.2c

Subscripts

Symbol	Meaning	Usual units	Section references
a	(a) Activation (b) Anodic	-	(a) 4.3.2, 4.3.2c (b) 6.4.1
A	Electroactive species	-	3.3, 3.3a, b, 3.4.1c, 3.5
ads	Adsorption	-	4.1
app	Apparent	-	8.3
c	Chemical	-	8.3
$chem.$	Chemical	-	8.3
$corr$	Correction	-	7.2b
ct	Charge-transfer	-	3.2.1, 3.2.2, 3.3, 3.5, 6.4.2, 7.3.1b, 7.3.2b
d	Decomposition rate constant	-	8.3
$dec.$	Decomposition of surface IrO_3	-	8.3
dl	Double-layer	-	4.1
e	Electrochemical rate constant	-	3.3a, 3.4.1c, 3.5
eff	Effective	-	3.4.1, 3.4.2, 4.3.2c, 10.1, 10.2
$elect.$	Electrochemical oxidation	-	8.3
eq	Equilibrium	-	3.2
ex	External	-	3.3
f	From E_f	-	Chapters 1-9

Symbol	Meaning	Usual units	Section references
Fe^{2+}	Electroactive species	-	3.3, 3.4.1, 3.5
g	(a) Geometrical	(a) -	(a) 3.1, 4.3.4, 8.3
	(b) From the cross-section of a differential element	(b) -	(b) 3.2.1, 3.2.2
$int.diff.$	Internal pore diffusion	-	3.4.1b, c
irr	Irreversible	-	4.1
ISP	Isopropanol	-	8.3
ℓ	Loading	-	4.2a
lim	Limiting	-	6.4.1
lim,a	Anodic limiting	-	6.4.1
lim,c	Cathodic limiting	-	6.4.1
ox	Ox species	-	10.1
$oxid.$	Oxidation	-	8.3
p	(a) Particle	(a) -	(a) 3.2, 4.3.1, 4.3.4, 6.4.2
	(b) Peak	(b) -	(b) 10.1
	(c) Pore	(c) -	(c) 3.2.2, 3.3, 3.5, 10.1
pa	Anodic peak	-	5.3.3
red	Red species	-	10.1
$redox$	Reduction-oxidation	-	4.3.2c, 4.3.3
s	From the local current	-	3.2.1, 3.2.2
sp	(a) Specific charge	(a) -	(a) 4.3.3
	(b) Specific length	(b) -	(b) 4.3.1a
	(c) Specific loading	(c) –	(c) 4.3.3, 4.3.4, 5.3.2, 6.4.2, 7.2a, 7.3, 7.3.1a, b, 7.3.2a, b, 8.3
	(d) Specific surface area	(d) -	(d) 4.3.3

Symbol	Meaning	Usual units	Section references
$total$	Total	-	3.2-I-A
$void$	Void	-	3.2-I-A
w	Wetted	-	3.1, 4.3.4, 8.3
Ω	Ohmic	-	3.2.1, 3.2.2, 3.5, 6.4.2, 7.3.1b, 7.3.2b
0	(a) From exchange current density (b) From density of IrO_2 active surface sites	(a) - (b) -	(a) 3.2-II, 3.2.1, 3.2.2, 3.5, 5.3.2, 6.4.1, 6.4.2, 7.3.1, 7.3.2 (b) 8.3
1	(a) From dimensionless number K from configuration SPC (b) Forward (c) Constant	(a) - (b) - (c) -	(a) 3.2.1, 6.4.2, 7.1, 7.3.1, 7.3.2 (b) 8.3 (c) 3.2.1, 3.3
-1	Backward	-	8.3
2	(a) From dimensionless number K from configuration CPC (b) Constant	(a) - (b) -	(a) 3.2.2 (b) 3.2.1, 3.3
$2D$	2-dimensional	-	5.3.2, 6.4.1, 6.4.2, 7.3
$3D$	3-dimensional	-	4.3.3, 4.3.4, 5.3.2, 6.4.2, 7.3, 7.3.1, 7.3.1a, b, 7.3.2a, b, 8.3

Superscripts

Symbol	Meaning	Usual units	Section references
ad	Adsorption	-	8.3
app	Apparent	-	4.3.2
$bulk$	Bulk (electrolyte)	-	8.3
e	Electrochemical	-	8.3
$e,0$	Electrochemical (standard)	-	8.3
eff	Effective	-	4.3.2c
ref	Reference	-	7.3, 8.3
$rel.$	Relative	-	7.3.1b, 7.3.2b, 8.3,
®	Registered trade mark	-	Chapters 1-9
0	Standard	-	8.3
*	(a) Bulk	(a) -	(a) 10.1
	(b) From voltammetric charge	(b) -	(b) 4.3.2a, b, c, 4.3.3
+	Anodic	-	4.3.2a, 4.3.3
−	Cathodic	-	4.3.2a, 4.3.3

Chapter 1

Introduction

The electrocatalytic activity of dimensionally stable anodes (DSA$^{®}$) is assigned to both intrinsic effects (electronic contribution) and surface area effects (geometric contribution). The electronic contributions are affected by the bond strength between the reaction intermediate and the electrode surface while the geometric contributions are related to the extension of the surface area. In addition, only the electronic contributions are linked with electrocatalysis, due to the fact that the activation energy of the reaction can strongly be affected by the nature of the electrode material. The distinction between electronic and geometric factors is of first importance for fundamental research and need to be evaluated.

In particular, DSA$^{®}$ electrodes are 3D devices which have a high working surface area. Nevertheless, rare are the systems where the totality of the surface area participates in the electrochemical reaction under investigation. As a matter of fact, due to the non-uniformity of the overpotential distribution and/or slow diffusion (relative to the reaction) within the coating, only part of the electrode surface participates effectively in the reaction. Therefore, in order to estimate the fraction of the electrode area which actually participates in the electrochemical reaction under investigation, the effectiveness factor, E_f, should be estimated.

The effectiveness factor has been used in other fields like in heavy metals recovery using 3D electrodes [1] or in heterogeneous catalysis [2]. However, this is the first time that the effectiveness factor has been adapted in electrocatalysis for studying its influence on the loading of DSA$^{®}$ (Ti/IrO$_2$) electrodes and on the kinetics of the investigated reactions. As a consequence, this work focuses on the estimation of the effectiveness factor, E_f, fraction of the surface which participates effectively in the investigated reactions such as:

(a) Fe^{3+}/Fe^{2+} (fast reaction), (b) O_2 and Cl_2 evolution (slow reactions), and (c) isopropanol oxidation (complex reaction involving redox catalysis).

In chapter 3, the theoretical aspects, in which two approaches have been used for the estimation of the effectiveness factor, are presented. The first approach is analytical (where two configurations have been used in order to describe the micro and macroporosity of the DSA$^{®}$ coating), while the second one is qualitative (where dimensionless numbers relating the time constants involved in the voltammetric measurements, internal diffusion and charge-transfer reaction are defined).

The voltammetric charge obtained from cyclic voltammetry (CV) measurements will be presented in chapter 4 using different potential scan rates, potential windows, and temperatures, for various Ti/IrO_2 loadings. Furthermore, in this chapter, in order to explain the influence of temperature and scan rates on the voltammetric charge, q^*, a model was proposed. In addition, the outer-inner surface model (Trasatti model) and the three capacitance model (Takasu model) have been considered in this model.

In chapter 5, the effectiveness of Ti/IrO_2 electrodes has been investigated using the Fe^{3+}/Fe^{2+} redox couple (as a fast probe reaction) and different loadings. Background current (voltammetric charge) and uncompensated electrolyte resistance are problems implicated in the electrochemical measurements. The experimental error on the standard rate constant, k^0, and on the effectiveness of the studied redox couple, due to the uncompensated electrolyte resistance, R_u, has been estimated.

In chapter 6, the effectiveness factor, E_f, of the Fe^{3+}/Fe^{2+} redox couple was estimated experimentally using Ti/IrO_2 rotating disk electrodes (RDE) and compared to the theoretical values using different IrO_2 loadings. For this purpose, steady-state polarization measurements were performed.

In chapter 7, the relative effectiveness factor, $E_f^{rel.}$, of the O_2 and Cl_2 evolution reactions have been estimated using different IrO_2 loadings and compared to the analytical approach given in chapter 3, section 3.2.1.

In chapter 8, the electrochemical oxidation of isopropanol was investigated on Ti/IrO_2 electrodes, to which a model has been proposed. The relative effectiveness factor, $E_f^{rel.}$, for the involved electrochemical and chemical reactions has been evaluated for different IrO_2 loadings.

Finally, chapter 9 summarizes the main results obtained in this thesis while chapter 10 shows some possible future ideas for the better evaluation of the effectiveness factor of the DSA$^®$ (3D) (Ti/IrO$_2$) electrodes.

References

1.   F. Coeuret, D. Hutin, A. Gaunand, *J. Appl. Electrochem.*, 1976, **6**, 417.

2.   O. Levenspiel, *Chemical Reaction Engineering*, Wiley Eastern Limited, 2$^{nd.}$ Edition, New Delhi, 1972, 473.

Chapter 2

Bibliography

In this chapter it will be given in brief the bibliography related to the dimensionally stable anodes, DSA®, particularly for Ti/IrO$_2$ electrodes. The first part focuses mainly on the success of the DSA® electrodes, their configuration and some of their potential applications. In the second part, investigations related to the effectiveness factor, E_f, of DSA® type electrodes will be presented.

2.1 Dimensionally Stable Anodes (DSA®)

2.1.1 History of the DSA® electrodes

Dimensionally Stable Anodes (DSA®) consist of a metal base (usually Ti) coated by a thin oxide coating. These anodes have been studied and successfully developed since the sixties [1, 2]. In 1964-1965, Henry Beer on one side and Oronzio De Nora-Diamond Division Researches on the other, started to investigate these electrodes for both chlorine and oxygen evolution reactions [3-5].

These electrodes have successfully replaced graphite anodes used in the chlor-alkali industry [6-8]. In fact, graphite had high overpotential for chlorine evolution and low stability due to the side reaction of O$_2$ evolution [9]. The big advantage of the DSA® electrodes is that they guarantee a lifetime of up to 10 years for at least what concerns the chlorine evolution process [10].

2.1.2 Configuration of the DSA® electrodes

Dimensionally stable anodes (DSA®), as presented in the previous paragraph, consist of a metal base having the right geometry, which supports metal oxide electrocatalysts for the desired reaction. In principal, the choice of the metal base and the electrocatalyst depends on the type of electrochemical process involved. For instance, in the Br_2 production from NaBr and HBr solutions, Ti, Ta, Nb, etc., are the proper metal bases, while $RuO_2 + TiO_2$ is the optimal coating. In the electrowinning of metals (Cu and Zn) from highly concentrated sulphuric solutions, Ti-Pd alloys are recommended as the metal base, whereas the suggested coatings include RuO_2, IrO_2, $RuO_2 + TiO_2$, and $Ir + IrO_2$ [11].

As seen above, generally, titanium is implied in the support of DSA® electrodes because of its excellent combination of mechanical properties, low density and corrosion resistance. On the other hand, a result due to the preparation of the DSA® electrode, by thermal treatment, is that titanium is partially oxidized forming a thin insulating layer of TiO_x between the base metal and the electrocatalyst, which strongly reduces the service life of the electrodes [12]. Zirconium, niobium, and tantalum are other metals that have been recommended [12-14], in which tantalum has appeared to be the most apt anode material, because of its high corrosion resistance in aggressive medium, due to the protective oxide film that is formed [15]. Nevertheless, its lower electrical resistivity, higher density, and higher cost compared to titanium have restricted its industrial applications. Therefore, p-silicon was later used in 2003 in our group by M. Panizza et al. because of its high anodic stability and reasonable cost for the application of organics oxidation [15].

Furthermore, another used support is the boron-doped diamond (BDD). At our laboratory, since 2003 with the work of I. Duo [16], she used the BDD as support in order to deposit IrO_2 nanoparticles. The idea of her work was to improve and better understand the electrocatalytic activity of the IrO_2 nanoparticles towards redox processes and the oxygen evolution reaction.

2.1.3 Potential applications of the DSA® electrodes

In the next section, we will pass briefly the most important electrochemical reactions in which the DSA® electrodes are applied:

6

a) <u>Cl_2 evolution reaction</u>:

The evolution of the DSA® type electrodes (Ti/RuO_2-TiO_2) has found solutions, in a very satisfying manner, to the issues associated with the electrochemical production of chlorine and caustic soda (in the chlor-alkali industry) [17]. These electrodes, however, evidence very poor performances when used as oxygen anodes [11].

b) <u>O_2 evolution reaction</u>:

IrO_2 as a catalyst for the O_2 evolution in DSA® electrodes, has acquired interest and is shown in [18, 19]. Previous work at our laboratory [20, 21], established, through a systematic investigation of various coatings, that the Ti/IrO_2-Ta_2O_5 (70-30%mol) coating deposited on Ti, showed the best performances of anodic stability and electrocatalytic activity, which are essential characteristics for industrial applications.

c) <u>Organics oxidation reactions</u>:

In our laboratory, it was demonstrated that regularly electrochemical oxidation of some organics in aqueous medium occurs, without any loss in the electrode activity, only at high potentials where simultaneous evolution of O_2 occurs [22, 23]. In addition, it has been found that the nature of electrode material influences strongly both the selectivity and the efficiency of the process [24-26]. In order to explain these observations, a general model for anodic oxidation of organics in acidic medium has been proposed [24-26]. This model allows distinguishing two limiting cases: 'active' and 'non-active' anode.

According to the typical proposed scheme for organics oxidation on metal oxides in acidic medium [25] given by our group already more than 10 years ago, the mechanism involves two parallel reaction paths as shown in Figure 2.1.
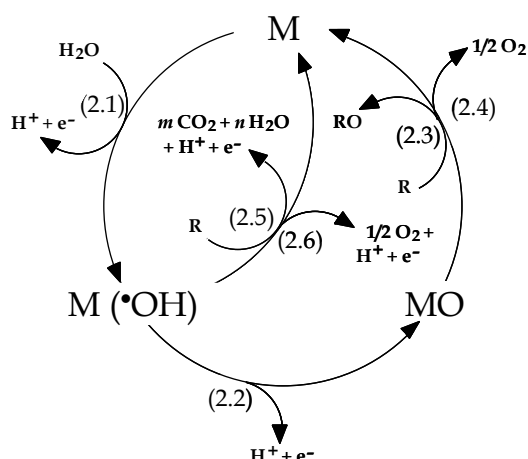
Figure 2.1: Scheme of the electrochemical oxidation of organic compounds on 'active' anodes (reactions (2.1), (2.2), (2.3), (2.4)) and on 'non-active' anodes (reactions (2.1), (2.5), (2.6)); M is an active site at the electrode surface.

In all cases, the initial step is the discharge of water molecules to form adsorbed hydroxyl radicals (reaction (2.1)). The electrochemical and chemical reactivity of the adsorbed hydroxyl radicals depends strongly on the nature of the used electrode material. Two extreme types of electrodes can be defined: 'active' and 'non-active' electrodes:

a) At 'active' (electrocatalytic) electrodes, there is a strong electrode (M) - hydroxyl radical ($^{\bullet}OH$) interaction. In this case, there is a possible transition of the oxygen from the hydroxyl radical to the anode surface resulting in the formation of a higher oxide (reaction (2.2)). The surface redox couple MO/M can act as mediator in the oxidation of organics (reaction (2.3)), which may result in the partial (selective) oxidation of organics. This reaction is in competition with the side reaction of oxygen evolution due to the chemical decomposition of the higher oxide (reaction (2.4)). Typical 'active' electrodes are Ti/IrO$_2$ and Ti/RuO$_2$.

b) At 'non-active' (non-electrocatalytic) electrodes, there is a weak interaction between the electrode surface (M) and hydroxyl radicals ($^{\bullet}OH$). In this case, the oxidation of organics is mediated by hydroxyl radicals, which may result in fully oxidized reaction products such as CO$_2$ (reaction (2.5)). This reaction is also in competition with the side reaction of hydroxyl radical discharge to oxygen (reaction (2.6)). Typical 'non-active' electrodes are Ti/SnO$_2$-Sb$_2$O$_5$ and p-Si/BDD.

The difference between 'active' and 'non-active' behavior and the fundamentals of the mechanism are supported by several experimental observations like those given by B. Marselli et al. [27].

For explaining the mechanistic behavior of the 'active' electrode, one recent example studied in our laboratory, is the work of S. Fierro et al. for the investigation of the oxygen evolution and formic acid oxidation on Ti/IrO_2 electrodes using $H_2^{18}O$ in differential electrochemical mass spectrometry (DEMS) [28, 29]. S. Fierro et al. [28] have demonstrated that the IrO_2 layer indeed participates in both the O_2 evolution reaction and organics oxidation; what confirmed the proposed model (see Figure 2.1). In addition, these authors have found that the oxygen evolution reaction on $Ir^{16}O_2$ in $H_2^{18}O$ containing electrolyte, results in the $Ir^{16}O^{18}O$ formation, according to reactions (2.7) and (2.8).

$$IrO_2 + H_2^{18}O \rightarrow Ir^{16}O^{16}O^{18}O + 2H^+ + 2e^- \tag{2.7}$$

$$2Ir^{16}O^{16}O^{18}O \rightarrow 2Ir^{16}O^{18}O + {}^{16}O_2 \tag{2.8}$$
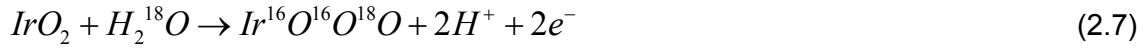
Additionally, these authors have observed that ^{18}O-labelled IrO_2 results in formation of $^{16}O^{18}O$ and $^{18}O_2$; what proves that the oxygen evolution proceeds via mediation of the IrO_3/IrO_2 redox couple. In the second part of their experiment [29], oxidation of formic acid was performed on $Ir^{16}O^{18}O$. During this experiment, $C^{16}O^{18}O$ evolution was observed showing that the IrO_2 coating participates in the oxidation process (see reaction (2.9)):

$$Ir^{16}O^{18}O + HC^{16}O^{16}OH \rightarrow Ir^{16}O^{16}O + C^{16}O^{18}O + 2H^+ + 2e^- \tag{2.9}$$
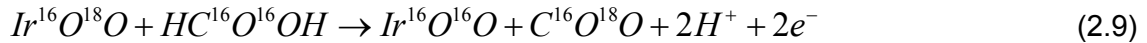
2.2 Estimation of the effectiveness factor, E_f, and the electrochemically active surface area (EASA)

The effectiveness factor has firstly been introduced by O. Levenspiel [30] in heterogeneous catalysis. It has been defined as the ratio of the actual reaction rate in the pore with respect to the rate unaffected by diffusion.

To the best of our knowledge, R. F. Savinell et al. [31] are the only researchers to introduce the term of effectiveness factor, E_f, for the DSA® electrodes, Ti/RuO$_2$ and Ti/IrO$_2$. However, these authors have not investigated the influence of the electrode kinetics on the effectiveness factor, E_f.

The measurement of the voltammetric charge can allow developing an empirical correlation between the voltammetric charge and the electrochemically active surface area (EASA). In fact, the voltammetric charge has been found to be directly related to the real surface area of the coating measured by Zn^{2+} ion adsorption [31].

2.3   References

1.   H. Beer, US 3 711 385, 1973.

2.   H. Beer, US 3 632 498, 1972.

3.   G. Bianchi, V. De Nora, P. Gallone and A. Nidola, US 3 616 445, 1971.

4.   G. Bianchi, V. De Nora , P. Gallone and A. Nidola, US 3 948 751, 1976.

5.   G. Bianchi, V. De Nora, P. Gallone and A. Nidola, US Appl. 778 736, 1968.

6.   A. T. Kuhn, *Industrial Electrochemical Processes*, Elsevier, New York, 1971.

7.   T. C. Jeffrey, P. A. Danna, H. S. Holden, in *Chlorine Bicentennial Symposium*, The Electrochemical Society, Princeton, New Jersey, 1974.

8.   K. Hass and P. Schmittinger, *Electrochim. Acta*, 1976, **21**, 1115-1126.

9.   H. V. K. Udupa, R.Thangappan, B. R. Yadav, P. Subbiah, *Chem. Age India*, 1972, **23**, 545.

10.   S. Trasatti, *Electrochim. Acta*, 2000, **45**, 2377-2385.

11.   S. Trasatti, *Electrodes of Conductive Metallic Oxides. Studies in Physical and Theoretical Chemistry*, Vol. 11B, Elsevier Scientific Publishing Company, Amsterdam, 1981, 627-628, 642.

12.   G. P. Vercesi, J. Rolewicz and Ch. Comninellis, *Thermochimica Acta*, 1991, **176**, 31-47.

13.   De Nora, A. Nidola, G. Trisoglio, G. Bianchi, Patent 1399576, 1973.

14.   F. Cardarelli, P. Taxil, A. Savall, Ch. Comninellis, G. Manoli, O. Leclerc, *J. Appl. Electrochem.*, 1998, **28**, 245-250.

15.   M. Panizza, L. Ouattara, E. Baranova, Ch. Comninellis, *Electrochem. Comm.*, 2003, **5**, 365-368.

16.   I. Duo, PhD EPFL, No. 2732, 2003.

17.   O. De Nora, *Chem. Eng. Techn.*, 1970, **42**, 222.

18. T. Shimamune, H. Kawauchi, S. Nakatsu, Y. Nishiki, R. Hayashi, *J. Electrochem. Soc.*, 1989, **89**, 555.

19. G. Lodi, A. De Battisti, G. Bordin, C. De Asmundis, and A. Benedetti, *J. Electroanal. Chem.*, 1990, **277**, 139-150.

20. J. Rolewicz, Ch. Comninellis, E. Plattner, and J. Hinden, *Chimia*, 1988, **42**, 75.

21. J. Rolewicz, Ch. Comninellis, E. Plattner, and J. Hinden, *Electrochim. Acta*, 1988, **33**, 573-580.

22. Ch. Comninellis and E. Plattner, *Chimia*, 1988, **42**, 250.

23. Ch. Comninellis and C. Pulgarin, *J. Appl. Electrochem.*, 1991, **21**, 703-708.

24. G. Foti, D. Gandini, Ch. Comninellis, A. Perret, W. Haenni, *Electrochem. Solid State Letters*, 1999, **2**, 228.

25. G. Foti, D. Gandini, Ch. Comninellis, in *Current Topics in Electrochemistry*, Vol. 5, Research Trends, Trivandrum, 1997, 71.

26. Ch. Comninellis and G. Foti, in *Modern Aspects of Electrochemistry*, R. White, B. E. Conway, C.G. Vayenas, Editors, Vol. 37, Kluwer Academic/Plenum Publishers, New York, 2004, 87.

27. B. Marselli, J. Garcia-Gomez, P. A. Michaud, M. A. Rodrigo and Ch. Comninellis, *J. Electrochem. Soc.*, 2003, **150**, D79-D83.

28. S. Fierro, T. Nagel, H. Baltruschat, Ch. Comninellis, *Electrochem. Comm.*, 2007, **9**, 1969-1974.

29. S. Fierro, T. Nagel, H. Baltruschat, Ch. Comninellis, *Electrochem. Solid State Letters*, 2008, **11**, E20-E23.

30. O. Levenspiel, *Chemical Reaction Engineering*, Wiley Eastern Limited, 2nd. Edition, New Delhi, 1972, 473.

31. R. F. Savinell, R. L. Zeller, and J. A. Adams, *J. Electrochem. Soc.*, 1990, **137**, 489-494.

Chapter 3

Theoretical treatment

In this chapter, two approaches have been used for the estimation of the effectiveness factor, E_f, (i.e. the fraction of the surface which participates effectively in the investigated reaction) of a DSA[®] coating: One being analytical and another one qualitative. In the analytical approach, two configurations have been used in order to describe the micro and macroporosity of the DSA[®] coating. Furthermore, two simplified conditions: Constant concentration (overpotential distribution) and constant overpotential (concentration distribution) have been considered.

Dimensionless numbers relating the time constant involved in the voltammetric measurements, internal diffusion and charge-transfer reaction, have been defined for the qualitative estimation of the effectiveness factor, E_f, under transient conditions (i.e. linear sweep and cyclic voltammetries).

Even if the proposed approaches have been used in other fields [1, 2], this is the first time that they have been adapted in electrocatalysis, particularly for DSA[®] electrode applications, for the investigation of different electrochemical reactions using various catalyst loadings.

3.1   Introduction

DSA[®] electrodes consist of an electrocatalytic porous coating of few micrometers thickness deposited on a usually Ti base metal. These electrodes are 3D devices and in

principle have high surface area. The real (wetted) surface area, A_w, is, of course, always larger than the geometric (projected) area, A_g, and the 3D roughness factor, γ_{3D}, is the ratio of the two:

$$\gamma_{3D} = \frac{A_w}{A_g} \hspace{6cm} (3.1)$$

Routinely prepared DSA® electrodes typically have a roughness factor of 100-200 [3]. However, rare are the systems where the totality of the real surface area participates in the electrochemical reaction under investigation.

In order to quantify the real (working) electrode area, which actually participates in the electrochemical reaction under investigation, the effectiveness factor, E_f, has been defined as the fraction of the surface which participates effectively in the investigated reaction.

For the estimation of the effectiveness factor, E_f, two main approaches have been used:

(a) An analytical approach which can allow the estimation of the effectiveness factor, E_f, considering two simplifying conditions, i.e. constant concentration of the electroactive species within the DSA® coating (section 3.2) and constant overpotential within the coating (section 3.3).

(b) A qualitative approach allowing the estimation of the effectiveness factor, E_f, under transient operation (section 3.4).

3.2 Overpotential distribution within the DSA® electrodes (constant concentration)

The aim of this section is to derive an analytical expression for the distribution of the overpotential within the porous structure of the coating. For this purpose, we have supposed that the concentration of the electroactive species within the porous coating

remains constant (both the exchange current density, j_0, and the equilibrium potential, E_{eq}, remain constant). Furthermore, we neglect the concentration overpotential, i.e. the bulk concentration of the electroactive species is equal to the concentration within the coating.

Under these conditions, three main factors can influence the distribution of overpotential within the DSA$^{®}$ coating:

- The morphology,
- The apparent electrolyte conductivity,
- The kinetics of the investigated electrochemical reaction.

I) <u>Morphology of the DSA$^{®}$ electrodes</u>

The morphological analysis of the coating has shown that the surface exhibits a cracked dried-mud look (see section 4.3.1, Figure 4.5). This structure can induce two types of porosity (void fraction):

(a) A microporosity due to the coating itself, consisted of nanoparticles of few nanometres diameter (see Figure 4.5b).
(b) A macroporosity due to the cracks of the coating (see Figure 4.5a).

In order to describe this heterogeneous structure of the coating, two configurations have been used:

- The spherical particle configuration (SPC) related to the microporosity
- The cylindrical pore configuration (CPC) related to the cracks of the coatings (macroporosity).

A) Spherical particle configuration (SPC): (Two parameter configuration: Void fraction: ε, particle diameter: d_p)

According to this configuration, a schematic representation of the DSA$^{\circledR}$ coating is shown in Figure 3.1. It is considered as a porous medium of void fraction, ε, which consists of spherical conducting particles with diameter, d_p.
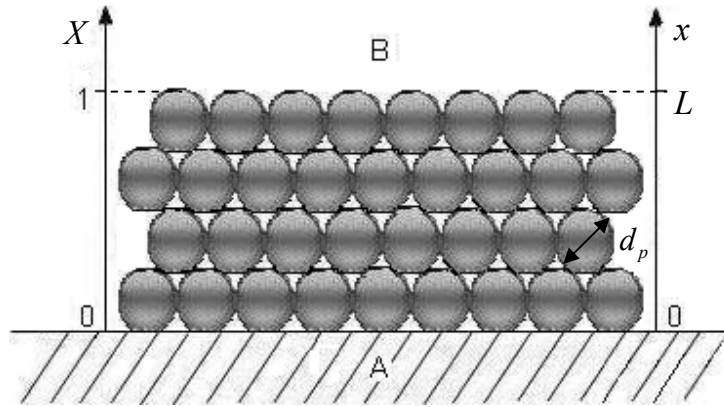
Figure 3.1: Schematic representation of the SPC configuration consisting of spherical particles with diameter, d_p, and void fraction, ε. (A) Ti substrate and (B) electrolyte. L is the thickness of the coating, $X = x / L$ is the dimensionless distance, and d_p is the diameter of the electrode particles.

The void fraction of the DSA$^{\circledR}$ coating, ε, is defined by the relation:

$$\varepsilon = \text{void volume/total volume} = \frac{V_{void}}{V_{total}} \text{ [-]} \tag{3.2}$$

where: V_{void}: Void volume of the coating [cm^3] and V_{total}: total volume [cm^3].

Furthermore, the specific particle area, a_p, has been defined by the relation:

$$a_p = \text{surface of the particle/volume of the particle} = \frac{4\pi r^2}{(4/3)\pi r^3} = \frac{6}{d_p} \text{ [1/cm]} \tag{3.3}$$

16

where: r : radius of the particles [cm] and d_p : diameter of the particles [cm].

B) Cylindrical pore configuration (CPC): (Two parameter configuration: Density of cylindrical pores: N_p , diameter of the cylindrical pores: d)

In this configuration, we consider that the DSA® coating is equivalent to a porous medium of cylindrical pores having a density, N_p [pores/cm²] and diameter, d [cm] as shown in Figure 3.2:
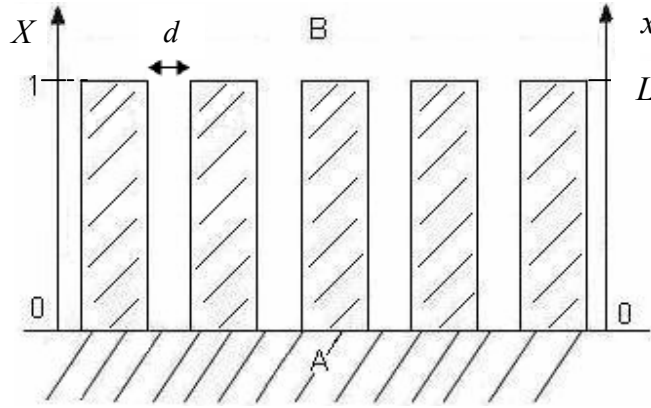
Figure 3.2: Schematic representation of the CPC configuration consisting of cylindrical pores with a density of N_p/cm² and diameter, d . (A) Ti substrate and (B) electrolyte. L is the thickness of the coating and X is the dimensionless distance.

II) Apparent electrolyte conductivity within the DSA® electrodes [1]

The apparent electrolyte conductivity within the DSA® coating, γ , will depend mainly on the void fraction of the DSA® electrode, ε . The relation is written as follows [1]:

$$\gamma = \gamma_0 \left(\frac{2\varepsilon}{3 - \varepsilon} \right) \tag{3.4}$$

where: γ is the apparent electrolyte conductivity inside the DSA® coating [1/Ωcm], γ_0 is the bulk electrolyte conductivity [1/Ωcm], and ε is the void fraction of the DSA® coating [-].

III) <u>Kinetics of the electrochemical reaction</u>

We consider that we are dealing with a simple one electron transfer reaction without any mass transfer limitation.

$$M^n \rightleftharpoons M^{n+1} + e^-$$ (3.5)

Under these conditions, the Butler-Volmer equation can be used:

$$j = j_0 \left[\exp^{\alpha \frac{F}{RT} \eta} - \exp^{-(1-\alpha) \frac{F}{RT} \eta} \right]$$ (3.6)

where: j is the current density, [A/cm^2], j_0 is the exchange current density, [A/cm^2], α is the transfer coefficient, [-], F is the Faraday constant 96485, [C/mol], R is the molar gas constant 8.31, [J/molK], T is the temperature, [K], and η is the overpotential, [V].

Equation (3.6) for low overpotentials ($\eta < 10$mV) can be approximated to equation (3.7) (low-field approximation equation):

$$j = j_0 \left[\left(1 + \alpha \frac{F}{RT} \eta \right) - \left(1 - (1-\alpha) \frac{F}{RT} \eta \right) \right]$$

$$j = j_0 \frac{F}{RT} \cdot \eta$$ (3.7)

3.2.1 Modelling of the overpotential distribution using the spherical particle configuration (SPC)

In order to determine the overpotential distribution within the DSA$^®$ coating, we have used a similar approach as the one used by F. Coeuret [1] for the design of a porous

medium for the recovery of heavy metals. We consider a differential element of thickness, Δx, and cross-section, A_g, (see Figure 3.3):
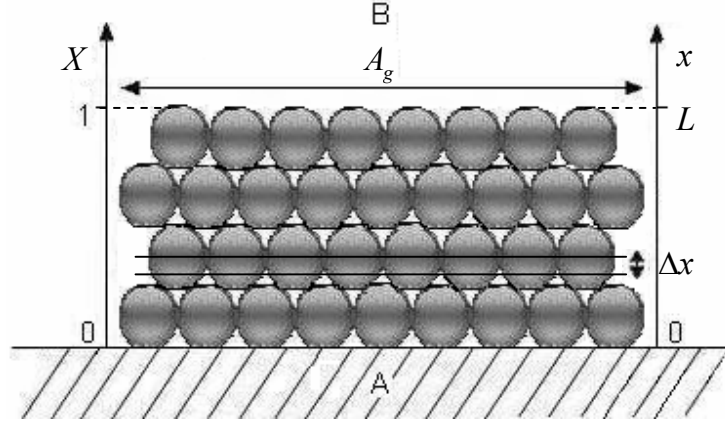
Figure 3.3: Schematic representation of the DSA® electrode according to the SPC configuration consisting of spherical particles with diameter, d_p, showing a differential element of thickness, Δx, and cross-section, A_g. (A) Ti substrate and (B) electrolyte. L is the thickness of the coating and X is the dimensionless distance.

The change of the local current, $I_s(x)$, within this differential ($\Delta x \to 0$) element, and due to the charge transfer reaction occurring at the total surface area of the element is given by equation (3.8):

$$dI_s(x) = j_0 \frac{F}{RT}\eta(x)a_p(1-\varepsilon)A_g dx \qquad (3.8)$$

where:

$I_s(x)$: Local current within the differential element, [A],

j_0 : Exchange current density, [A/cm²],

ε : Void fraction of the porous coating, [-],

a_p : Specific particle area, [1/cm],

$\eta(x)$: Local overpotential at x, [V],

A_g : Cross-section of the differential element, [cm²].

Dividing Equation (3.8) by the electrode thickness, L:

$$\frac{dI_s(x)}{L} = j_0 \frac{F}{RT} \eta(x) a_p (1-\varepsilon) A_g \frac{dx}{L} \tag{3.9}$$

From the relation $X = x/L$, one can write $dX = dx/L$ to give:

$$\frac{dI_s(X)}{dX} = j_0 \frac{F}{RT} \eta(X) a_p (1-\varepsilon) A_g L \tag{3.10}$$

Now, we consider that the electronically conductive phase of the porous medium (particles) is equipotential. In this case, Ohm's law can be applied to the electrical conduction through the pores of the differential element to give the variation of the local overpotential as:

$$d\eta(x) = RI_s(x) \tag{3.11}$$

where:

R: Apparent electrolyte resistance within the porous medium, [Ω].

The apparent electrolyte resistance, R, within the differential element can be given by the relation:

$$R = \frac{1}{\gamma} \frac{dx}{A_g} \tag{3.12}$$

From Equations (3.11) and (3.12):

$$d\eta(x) = \frac{1}{\gamma A_g} I_s(x) dx \tag{3.13}$$

Dividing Equation (3.13) by L and rearranging:

20

$$\frac{d\eta(X)}{dX} = \frac{1}{\gamma A_g} LI_s(X)$$

(3.14)

After derivation:

$$\frac{d^2\eta(X)}{dX^2} = \frac{1}{\gamma A_g} L \frac{dI_s(X)}{dX}$$

(3.15)

Replacing Equation (3.10) into Equation (3.15) gives:

$$\frac{d^2\eta(X)}{dX^2} = \frac{1}{\gamma} L^2 j_0 \frac{F}{RT} (1-\varepsilon) a_p \eta(X)$$

(3.16)

This relation can be written as:

$$\frac{d^2\eta(X)}{dX^2} - K_1^2 \eta(X) = 0$$

(3.17)

with:

$$K_1^2 = \frac{1}{\gamma} L^2 j_0 \frac{F}{RT} (1-\varepsilon) a_p$$

(3.18)

The dimensionless number, K_1^2, (Equation (3.18)), includes parameters like:

- The morphology (a_p, ε, L),
- The apparent electrolyte conductivity (γ),
- The kinetics of the investigated electrochemical reaction (j_0).

In Equation (3.18), we replace Equation (3.4):

21

$$K_1^2 = j_0 \frac{F}{RT}(1-\varepsilon)a_p L^2 \frac{1}{\gamma_0}\left(\frac{3-\varepsilon}{2\varepsilon}\right)$$ (3.19)

Furthermore, Equation (3.19) can be related to two resistances:

(a) Charge-transfer resistance, R_{ct} [Ωcm^2] related to the kinetics of the investigated electrochemical reaction given by equation (3.20):

$$R_{ct} = \frac{RT}{j_0 F}$$ (3.20)

(b) Ohmic resistance, R_Ω [Ωcm^2] related to the morphology of the DSA$^\circledR$ electrodes and the conductivity of the electrolyte given by equation (3.21):

$$R_\Omega = (1-\varepsilon)a_p L^2 \frac{1}{\gamma_0}\left(\frac{3-\varepsilon}{2\varepsilon}\right)$$ (3.21)

Using Equations (3.19), (3.20) and (3.21), we obtain equation (3.22):

$$K_1^2 = \frac{(1-\varepsilon)a_p L^2 \frac{1}{\gamma_0}\left(\frac{3-\varepsilon}{2\varepsilon}\right)}{\frac{RT}{j_0 F}} = \frac{R_\Omega}{R_{ct}}$$ (3.22)

Equation (3.17) is a second order linear ordinary differential equation. Its solution is given by:

$$\eta(X) = M_1 \exp(K_1 X) + M_2 \exp(-K_1 X)$$ (3.23)

where: M_1 and M_2 are constants defined by the limiting conditions (see Figure 3.3):

1) At $X = 0 : \dfrac{d\eta}{dX} = 0$

$$\frac{d\eta}{dX} = K_1 M_1 \exp(K_1 X) - K_1 M_2 \exp(-K_1 X)$$

$$\left(\frac{d\eta}{dX}\right)_{X=0} = K_1 M_1 \exp(K_1 \cdot 0) - K_1 M_2 \exp(-K_1 \cdot 0) = K_1(M_1 - M_2) = 0$$

resulting in $M_1 = M_2 = M$.

Replacing M in Equation (3.23) gives:

$$\eta(X) = M[\exp(K_1 X) + \exp(-K_1 X)] \tag{3.24}$$

2) At $X = 1$: $\eta = \eta(1)$

$$\eta(1) = M\left[\exp(K_1) + \exp(-K_1)\right]$$

Rearranging Equation (3.24), where the constant M is written as:

$$M = \frac{\eta(1)}{\exp(K_1) + \exp(-K_1)} \tag{3.25}$$

Replacing Equation (3.25) in Equation (3.24) gives:

$$\eta(X) = \eta(1) \frac{\exp(K_1 X) + \exp(-K_1 X)}{\exp(K_1) + \exp(-K_1)}$$

which may be written in terms of hyperbolic functions as:

$$\eta(X) = \eta(1) \frac{\cosh(K_1 X)}{\cosh(K_1)} \tag{3.26}$$

and also the following two expressions hold:

$$\eta(1) = \eta(0)\cosh(K_1) \tag{3.27}$$

and

$$\eta(X) = \eta(0)\cosh(K_1 X) \tag{3.28}$$

Finally one can write:

$$\frac{\eta(X) - \eta(0)}{\eta(1) - \eta(0)} = \frac{\cosh(K_1 X) - 1}{\cosh(K_1) - 1} \tag{3.29}$$

From Equation (3.29), one can get the average overpotential, $\overline{\eta}$, defined by equation (3.30), which is related to the average current passing through the DSA® coating:

$$\overline{\eta} = \frac{\int_0^1 \eta(X)dX}{\int_0^1 dX} \tag{3.30}$$

Replacing $\eta(X)$ from Equation (3.28) gives the expression of the average overpotential as a function of K_1 as follows:

$$\overline{\eta} = \frac{\eta(0)\int_0^1 \cosh(K_1 X)dX}{\int_0^1 dX} = \eta(0)\frac{\sinh(K_1 X)}{K_1}\bigg|_0^1 = \eta(0)\frac{\sinh(K_1)}{K_1} \tag{3.31}$$

From Equations (3.31) and (3.27), we can obtain the effectiveness factor, E_f, of the DSA® coating, defined by equation (3.32):

$$E_f = \frac{\bar{\eta}}{\eta(1)} = \frac{(1/K_1) \cdot \eta(0)\sinh(K_1)}{\eta(0)\cosh(K_1)} = \frac{\tanh(K_1)}{K_1} \qquad (3.32)$$

This effectiveness factor will allow us to estimate the fraction of the surface coating which participates effectively in the investigated reaction.

Two limiting cases can be considered:

- $K_1 \approx 0 \Rightarrow E_f = 1 \Rightarrow$ The entire wetted 3D surface participates in the electrochemical reaction (ohmic resistance is much smaller than the charge-transfer resistance $(R_\Omega << R_{ct})$).

- $K_1 >> 1 \Rightarrow E_f = 0 \Rightarrow$ Only the wetted 2D surface participates in the electrochemical reaction (ohmic resistance is much larger than the charge-transfer resistance $(R_\Omega >> R_{ct})$).

3.2.2 Modelling of the overpotential distribution using the cylindrical pore configuration (CPC)

In order to determine the overpotential distribution within the DSA® electrode, we consider a differential element of thickness, Δx, and cross-section, A_g, (see Figure 3.4):
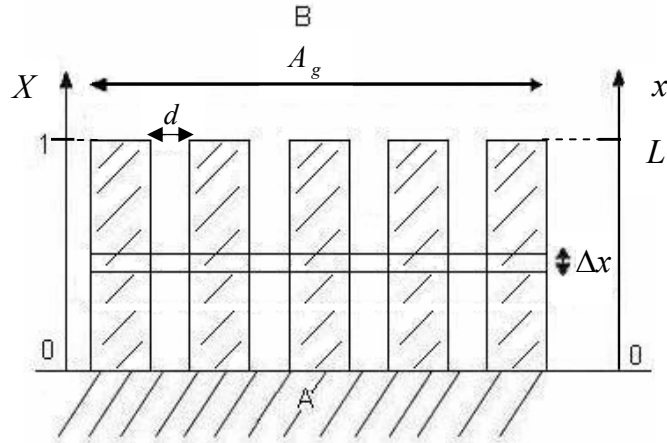
Figure 3.4: Schematic representation of the DSA® electrode according to the CPC configuration consisting of cylindrical pores with a density of N_p/cm² and diameter d, showing a differential element of thickness, Δx, and cross-section, A_g. (A) Ti substrate and (B) electrolyte. L is the thickness of the coating and X is the dimensionless distance.

The change of the local current, $I_s(x)$, within this differential ($\Delta x \rightarrow 0$) element, and due to the charge transfer reaction occurring at the total surface area of the element, is given by equation (3.33):

$$dI_s(x) = j_0 \frac{F}{RT} \eta(x) A_g N_p d \cdot \pi dx \tag{3.33}$$

where:

$I_s(x)$: Local current within the differential element, [A],

j_0: Exchange current density reported towards the cross-section, A_g, [A/cm²],

d: Pore diameter, [cm],

N_p: Number of pores per cm², [1/cm²],

$\eta(x)$: Local overpotential at x, [V],

A_g: Cross-section of the differential element, [cm²].

Dividing Equation (3.33) by L and considering $X = x / L$:

$$\frac{dI_s(X)}{dX} = j_0 \frac{F}{RT}\eta(X)A_g L N_p d \cdot \pi \tag{3.34}$$

As seen in section 3.2.1, considering equipotential the electronically conductive phase of the porous medium (particles) leads to equation (3.15):

$$\frac{d^2\eta(X)}{dX^2} = \frac{1}{\gamma A_g} L \frac{dI_s(X)}{dX} \tag{3.15}$$

From Equations (3.15) and (3.34):

$$\frac{d^2\eta(X)}{dX^2} = \frac{1}{\gamma}L^2 j_0 \frac{F}{RT}d \cdot \pi N_p \eta(X) \tag{3.35}$$

This relation can be written as:

$$\frac{d^2\eta(X)}{dX^2} - K_2^2\eta(X) = 0 \tag{3.36}$$

with:

$$K_2^2 = \frac{1}{\gamma}L^2 j_0 \frac{F}{RT}d \cdot \pi N_p \tag{3.37}$$

Similar to the previous configuration (section 3.2.1), the dimensionless constant K_2^2 from Equation (3.37), can be expressed by two resistances:

(a) Charge-transfer resistance, R_{ct} [Ωcm^2]:

$$R_{ct} = \frac{RT}{j_0 F} \tag{3.20}$$

(b) Ohmic resistance, R_Ω [Ωcm^2]:

$$R_\Omega = \frac{\pi N_p L^2 d}{2\gamma_0 \varepsilon}(3-\varepsilon)$$

(3.38)

with:

$$K_2^2 = \frac{R_\Omega}{R_{ct}}$$

(3.39)

Similar to the mathematical solution of the SPC configuration, we obtain for the CPC configuration the following solution:

$$\eta(X) = \eta(0)\cosh(K_2 X)$$

(3.40)

and

$$\frac{\eta(X)-\eta(0)}{\eta(1)-\eta(0)} = \frac{\cosh(K_2 X)-1}{\cosh(K_2)-1}$$

(3.41)

Finally, the average overpotential, $\bar{\eta}$, is written as:

$$\bar{\eta} = \eta(0)\frac{\sinh(K_2)}{K_2}$$

(3.42)

and the effectiveness factor, E_f, can be given as:

$$E_f = \frac{\bar{\eta}}{\eta(1)} = \frac{(1/K_2)\cdot\eta(0)\sinh(K_2)}{\eta(0)\cosh(K_2)} = \frac{\tanh(K_2)}{K_2}$$

(3.43)

This effectiveness factor will allow us to estimate the percentage of the surface coating which participates in the investigated reaction.

Two limiting cases can be considered, just as for the SPC configuration:

- $K_2 \approx 0 \Rightarrow E_f = 1 \Rightarrow$ The whole wetted 3D surface participates in the electrochemical reaction (ohmic resistance is much smaller than the charge-transfer resistance $(R_\Omega << R_{ct})$).

- $K_2 >> 1 \Rightarrow E_f = 0 \Rightarrow$ Only the wetted 2D surface participates in the electrochemical reaction (ohmic resistance is much larger than the charge-transfer resistance $(R_\Omega >> R_{ct})$).

Figure 3.5 shows the theoretical overpotential distribution within the 3D electrode for different values of K.
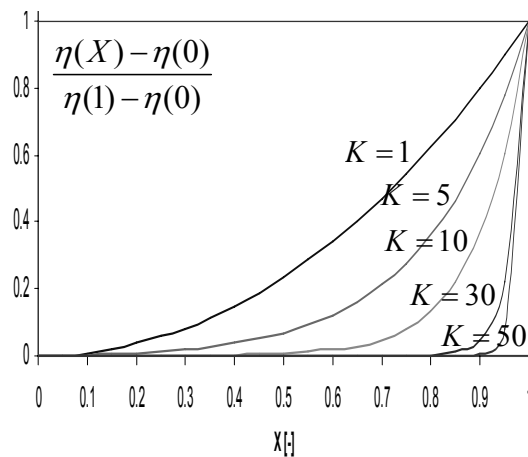
Figure 3.5: Plot of the overpotential distribution as a function of the dimensionless distance $X = x / L$ and of different K values.

3.3 Concentration distribution within the DSA® electrodes (constant overpotential)

The aim of this section is to study the concentration distribution of electroactive species within the DSA® electrodes. As seen in section 3.2, for obtaining an analytical expression of the distribution of the overpotential within the porous structure of the electrode, we have

supposed that the concentration of the electroactive species within the DSA$^{®}$ electrode remains constant.

However, in working systems, the situation is much more complex. Indeed, if the electrochemical reaction (charge-transfer reaction) is fast with respect to the internal diffusion (through the porous structure of the electrode), the concentration of the electroactive species will decrease with the penetration depth resulting in a stationary concentration profile.

In this section, and in order to obtain an analytical expression for the distribution of the concentration of the electroactive species with the penetration depth, we suppose that the overpotential remains constant within the DSA$^{®}$ electrodes.

Taking into consideration the cylindrical pore configuration (section 3.2.2) and considering the same approach as that used in heterogeneous catalysis [2], we can identify three main steps involved in the system: External film diffusion, internal pore diffusion and electrochemical reaction (charge-transfer reaction) at the external and internal surface.

A schematic representation of a single cylindrical pore showing these three steps is shown in Figure 3.6:
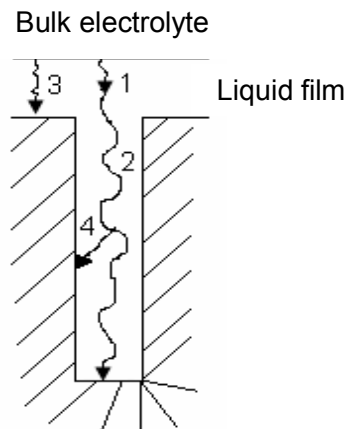
Figure 3.6: Schematic representation of a single cylindrical pore showing the involved steps:

1. External film diffusion,
2. Internal pore diffusion,
3. Electrochemical reaction (charge-transfer reaction) at the external surface, and
4. Electrochemical reaction (charge-transfer reaction) at the internal surface.

Figure 3.7 shows the equivalent circuit analogue to Figure 3.6 showing the corresponding resistances involved in these steps:
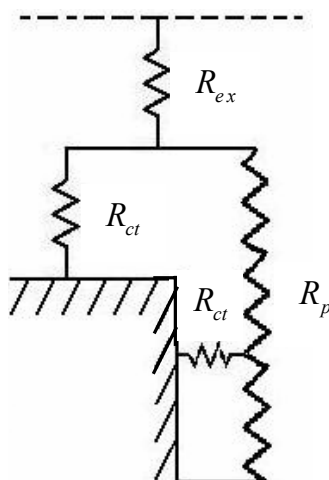
Figure 3.7: Electrical analogue of the different steps involved in the system. R_{ex}: External film resistance, R_p: internal pore resistance, and R_{ct}: charge-transfer resistance.

The external liquid film resistance, R_{ex}, is linked with the transport of the electroactive species from the bulk of the electrolyte towards the external surface of the electrode (step 1 in Figure 3.6). This resistance depends strongly on the hydrodynamic conditions. The internal pore resistance, R_p, is linked with the diffusion of the electroactive species through the pores (step 2 in Figure 3.6). The charge-transfer resistance, R_{ct}, at both the external surface (step 3 in Figure 3.6) and internal surface (step 4 in Figure 3.6) depends on the rate of the electrochemical reaction.

From Figure 3.7, we can see that the external resistance, R_{ex}, and the charge-transfer resistance, R_{ct}, do act in series with each other, and that it is the internal resistance which adds the complications since it is not related in a simple way to the other two resistances.

In this work, in order to further simplify the system, we neglect the external resistance and consider only the internal and the charge-transfer resistance.

a) <u>Internal resistance</u>

The internal resistance is related to the molecular diffusion of the electroactive species (A) inside the pores.

This diffusion within the pores is given by Fick's law (equation (3.44)):

$$J_A = -D_A \frac{dC_A}{dx}$$
(3.44)

where:

J_A: Flow of the active species within the pore [mol/cm²s],

D_A: Diffusion coefficient of the electroactive species within the DSA® coating [cm²/s],

C_A: Bulk concentration of the electroactive species [mol/cm³],

x: Distance [cm].

b) <u>Charge-transfer resistance</u>

The charge-transfer resistance for a simple one electron transfer reaction is related to the kinetics of the electrochemical reaction.

The rate of an electrochemical reaction can be given by the equation (3.45), (approximating $|\eta| > 100$mV):

$$r = \frac{j}{F} = k_e C_A \qquad \text{with: } k_e = k^0 \exp\frac{-\alpha F}{RT}\eta$$
(3.45)

where:

r : Electrochemical rate, [mol/cm²s],

j : Current density, [A/cm²],

k_e : Electrochemical rate constant, [cm/s],

C_A : Concentration of electroactive species in the bulk of the electrolyte (as we have neglected the external film resistance), [mol/cm³],

k^0 : Standard electrochemical rate constant, [cm/s],

T : Temperature, [K],

α : Transfer coefficient, [-],

η : Overpotential ($|\eta| > 100$mV), [V],

F : Faraday's constant, [C/mol],

R : Gas constant, [J/molK].

The material balance for the electroactive species A for a differential element within the pore (see Figure 3.8) is:
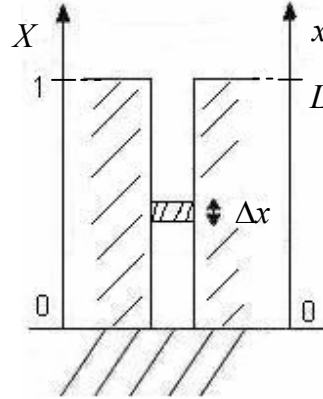
Figure 3.8: Schematic representation of a single cylindrical pore showing a differential element, Δx. L is the thickness of the coating and X is the dimensionless distance.

Output- input + disappearance by reaction = 0

$$\frac{\pi d^2}{4} J_{out} - \frac{\pi d^2}{4} J_{in} + r(\pi d \Delta x) = 0 \tag{3.46}$$

Using Fick's law (Equation (3.44)):

$$-\frac{\pi d^2}{4} D_A \left(\frac{dC_A}{dx}\right)_{out} + \frac{\pi d^2}{4} D_A \left(\frac{dC_A}{dx}\right)_{in} + r(\pi d \Delta x) = 0 \tag{3.47}$$

Rearranging Equation (3.47):

$$\frac{\left(\dfrac{dC_A}{dx}\right)_{out} - \left(\dfrac{dC_A}{dx}\right)_{in}}{\Delta x} - \frac{4}{D_A d} r = 0 \tag{3.48}$$

Taking the limit as $\Delta x \to 0$:

$$\frac{d^2 C_A}{dx^2} - \frac{4}{D_A d} r = 0 \tag{3.49}$$

The rate of the electrochemical reaction depends on the operation mode (galvanostatic or potentiostatic).

Considering the potentiostatic operation and using Equations (3.49) and (3.45), we obtain:

$$\frac{d^2 C_A}{dx^2} - \frac{4k_e}{D_A d} C_A = 0 \tag{3.50}$$

Or written with the dimensionless distance $X = x / L$ as variable:

$$\frac{d^2 C_A}{dX^2} - \frac{4k_e L^2}{D_A d} C_A = 0 \tag{3.51}$$

The solution of this differential equation is:

$$C_A(X) = M_1 \exp(mX) + M_2 \exp(-mX) \qquad \text{with} \quad m = \sqrt{\frac{4k_e L^2}{D_A d}} \tag{3.52}$$

where: M_1 and M_2 are constants.

Giving two limiting conditions from Figure 3.8, one has:

1. $X = 0$, $\dfrac{dC_A}{dX} = 0$, and deriving Equation (3.52) for $X = 0$:

$$\frac{dC_A}{dx} = mM_1 \exp(m \cdot 0) - mM_2 \exp(-m \cdot 0) = 0 \tag{3.53}$$

to give $M_1 = M_2 = M$. Replacing M in Equation (3.52):

$$C_A(X) = M[\exp(mX) + \exp(-mX)] \tag{3.54}$$

2. $X = 1$, $C_A(X) = C_A(1)$, where: $C_A(1)$ is the bulk concentration of A at $X = 1$, gives for the constant M:

$$M = \frac{C_A(1)}{\exp(m) + \exp(-m)} \tag{3.55}$$

Replacing Equation (3.55) in Equation (3.54):

$$C_A(X) = C_A(1)\frac{\exp(mX) + \exp(-mX)}{\exp(m) + \exp(-m)} = C_A(1)\frac{\cosh(mX)}{\cosh(m)} \tag{3.56}$$

and also the following two expressions hold:

$$C_A(1) = C_A(0)\cosh(m) \tag{3.57}$$

and

$$C_A(X) = C_A(0)\cosh(mX) \tag{3.58}$$

Thus one can write:

$$\frac{C_A(X) - C_A(0)}{C_A(1) - C_A(0)} = \frac{\cosh(mX) - 1}{\cosh(m) - 1} \tag{3.59}$$

The last relation is similar to Equation (3.41). The important parameter here is m, which is the Thiele modulus.

$$m = \sqrt{\frac{4k_e L^2}{D_A d}}$$

(3.60)

which is analogous to K_2^2 defined in Equation (3.39).

Finally, the average concentration, $\overline{C_A}$, within the pore is:

$$\overline{C_A} = \frac{\int_0^1 C_A(X)dX}{\int_0^1 dX} = C_A(0)\frac{\sinh(m)}{m}$$

(3.61)

and the effectiveness factor, E_f, can then be given by:

$$E_f = \frac{\overline{C_A}}{C_A(1)} = \frac{\tanh(m)}{m}$$

(3.62)

Figure 3.9 shows the plot of C_A in function of the dimensionless distance $X = x/L$ for various Thiele modulus m, according to Equation (3.60).
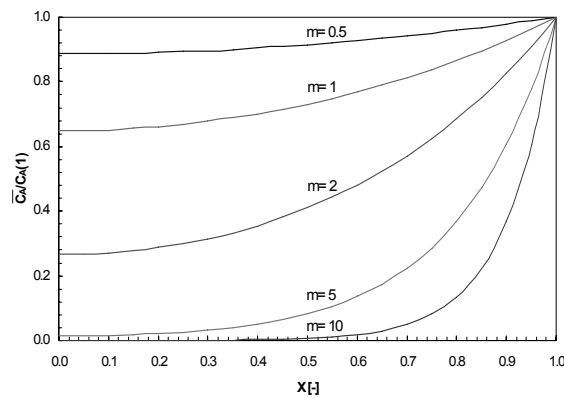
Figure 3.9: Plot representing the drop of the concentration along the pores as a function of the dimensionless distance $X = x/L$ and of Thiele modulus m, where: $m = \sqrt{\frac{4k_e L^2}{D_A d}}$.

36

An extension of this section for time dependent overpotential and taking into account the external diffusion is presented in chapter 10.

3.4 Qualitative approach allowing the estimation of the effectiveness factor under transient operation: Linear sweep voltammetry (LSV) or cyclic voltammetry (CV)

3.4.1 Effectiveness factor from the voltammetric measurements (LSV or CV)

In order to evaluate the effectiveness factor from linear sweep voltammetry (LSV) or cyclic voltammetry (CV) measurements using the Ti/IrO_2 electrodes, we consider the cylindrical pore configuration (see Figure 3.6). During the CV measurements at a given scan rate, the following steps are involved: External film diffusion of the electroctive species (step 1), internal pore diffusion of the electroactive species within the IrO_2 coating (step 2), electrochemical reaction (charge-transfer reaction) at the external (step 3) and internal (step 4) surface of the coating.
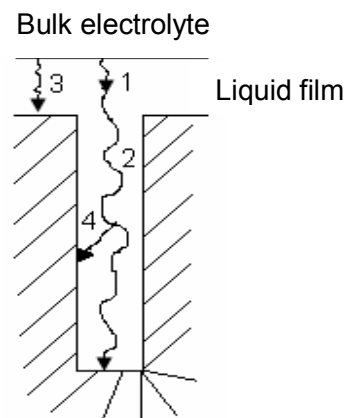
Figure 3.6: Schematic representation of a single cylindrical pore showing the involved steps: 1. External film diffusion, 2. Internal pore diffusion, 3. Electrochemical reaction at the external surface, and 4. Electrochemical reaction at the internal surface.

The external film diffusion step is associated with the transport of the electroactive species from the bulk of the electrolyte towards the external surface of the coating. The internal diffusion is linked with the diffusion of the electroactive species within the pores of the coating and depends strongly on its morphology. The charge-transfer step at both the external surface and internal surface depends on the kinetics of the investigated electrochemical reaction.

For a qualitative approach of this problem, we consider the characteristic time constants related to:

- The voltammetric measurement,
- The internal diffusion,
- The charge-transfer reaction.

a) <u>Time constant related to the voltammetric measurement</u>

The characteristic time involved in the transient voltammetric measurements (CV) can be given by the relation (equation (3.63)):

$$\tau_{volt.} = \frac{\Delta E}{\upsilon} \qquad\qquad (3.63)$$

where:

$\tau_{volt.}$: Time constant related to the voltammetric measurements [s],

ΔE : Characteristic potential difference used in the CV measurements [V],

υ : Scan rate [V/s].

The characteristic time related to the electrochemical reaction expresses the period in which the electroactive species enter in communication with the electrode. In case, where well defined anodic and cathodic peaks are obtained, ΔE in Equation (3.63) can be replaced by RT/F (for one electron reversible redox couple), or by the potential difference between the onset potential of the redox couple and the potential of peak current appearance, or by the potential window used in the voltammetric charge measurement.

b) Time constant related to the internal diffusion step

The time constant involved in this internal diffusion can be given by the relation (equation (3.64)):

$$\tau_{int.diff.} = \frac{L^2}{D_{eff}}$$

(3.64)

where:

$\tau_{int.diff.}$: Time constant related to the internal pore diffusion [s],

D_{eff} : Effective pore diffusion coefficient of the electroactive species [cm^2/s],

L : Thickness of the IrO$_2$ coating [cm].

c) Time constant related to the charge transfer step

The rate of an electrochemical reaction can be given by the Equation (3.45), (approximation for $|\eta| > 100$ mV):

$$r = \frac{j}{F} = k_e C_A \qquad \text{with: } k_e = k^0 \exp\frac{-\alpha F}{RT}\eta$$

(3.45)

where:

r : Electrochemical rate [mol/cm^{2}s],

j : Current density [A/cm^2],

k_e : Electrochemical rate constant [cm/s],

C_A : Concentration of electroactive species in the bulk of the electrolyte (as we have neglected the external film resistance) [mol/cm^3],

k^0 : Standard electrochemical rate constant [cm/s],

T : Temperature [K],

α : Transfer coefficient [-],

η : Overpotential ($|\eta|$ >100 mV) [V],

F : Faraday's constant [C/mol],

R : Gas constant [J/mol K].

The time constant involved in this charge transfer reaction [s] can be given by the equation (3.65):

$$\tau_{react.} = \frac{1}{a \cdot k_e} = \frac{1}{a \cdot k^0 \exp\dfrac{-\alpha F}{RT}\eta} \tag{3.65}$$

where:

a : Specific electrode surface area [1/cm].

This time constant is complex. In fact, not only the overpotential, η, is varied with time during the transient measurement, but it also varies through the coating. Furthermore, the concentration of the electroactive species varies within the coating, thus, this induces a modification of the standard rate constant, k^0, within the coating.

In order to simplify the problem, we have defined the following dimensionless parameters which relate the different time constants of the system.

- Dimensionless parameter, λ, related to the charge transfer reaction and the internal diffusion:

$$\lambda = \frac{\tau_{react.}}{\tau_{int.diff.}} = \frac{D_{eff}}{L^2 \cdot a \cdot k^0 \exp\dfrac{-\alpha F}{RT}\eta} \tag{3.66}$$

- Dimensionless parameter, γ, related to the voltammetric measurement and the internal diffusion:

$$\gamma = \frac{\tau_{volt.}}{\tau_{int.diff.}} = \frac{\Delta E \cdot D_{eff}}{\upsilon \cdot L^2} \tag{3.67}$$

Two extreme (arbitrary) situations can be considered:

I) $\lambda < 0.1, \; \gamma < 0.1$

In this case the electrochemical reaction rate is much faster than the pore diffusion rate and the voltammetric perturbation time (related to the scan rate) is much smaller than the time constant related to the internal diffusion. Under these conditions only the wetted 2D surface is involved in the voltammetric measurements.

In this case the peak current, I_p [A], during the CV measurements will be given by the relation:

$$I_p = (2.69 \cdot 10^5) A \cdot D_A^{1/2} \cdot C_A \cdot \upsilon^{1/2} \tag{3.68}$$

where:

A: Geometric surface area [cm^2],

C_A: Bulk concentration of the electroactive species A [mol/cm^3],

D_A: Diffusion coefficient of the electroactive species A [cm^2/s],

υ : Potential scan rate [V/s].

II) $\lambda > 10, \; \gamma > 10$

In this case the rate of the electrochemical reaction is much slower than the pore diffusion rate and the voltammetric perturbation time (related to the scan rate) is much higher than the time constant related to the pore diffusion. Under these conditions, the quasi-totality of the wetted 3D surface of the coating is expected to be involved in the voltammetric measurements.

In fact, under these conditions the peak current during the CV measurements should be much higher than that obtained in the previous case according to Equation (3.68), where only the geometric surface area participates in the electrochemical reaction.

A possible approach for the estimation of the effectiveness factor from the CV measurements will be to relate the measured current of the Ti/IrO$_2$ electrode with that calculated from Equation (3.68). In fact, if this ratio is much higher than unity, this will indicate that also a part (or the total) of the internal surface area participates in the electrochemical reaction. A quantitative estimation of the effectiveness factor using this approach is given in chapter 10.

3.4.2 Real surface area from voltammetric charge measurements

Using a similar approach as in section 3.4.1, the charging of the IrO$_2$ coating during the CV measurements can be treated. In this charging process, protons diffuse and react with the oxide within the coating, according to reaction (3.69):

$$IrO_x(OH)_y + \delta H^+ + \delta e^- \rightleftharpoons IrO_{x-\delta}(OH)_{y+\delta} \qquad (3.69)$$
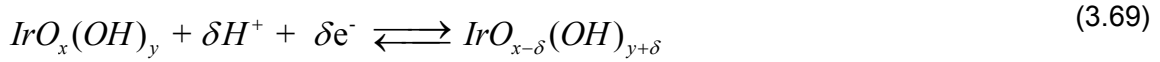
Considering that the investigated electrochemical reaction (3.69) is much faster than proton diffusion within the coating, the only parameter which controls the charging process will be the dimensionless parameter γ. This parameter relies the characteristic time involved in the voltammetric measurements with the characteristic time involved in the internal diffusion as shown in equation (3.70):

$$\gamma = \frac{\Delta E \cdot D_{eff}}{\upsilon \cdot L^2} \qquad (3.70)$$

where:

υ : Scan rate [V/s],

D_{eff} : Effective pore diffusion coefficient of H$^+$ [cm^2/s],

L : Thickness of the IrO$_2$ coating [cm],

ΔE : Potential window used in the CV measurements [V].

Two extreme (arbitrary) situations can be considered:

I) $\gamma < 0.1$

Under these conditions the time constant involved in the voltammetric measurements is much lower than the characteristic time involved in the internal diffusion. In this case, the obtained voltammetric charge (after correction of the double layer charging) corresponds to the wetted 2D surface.

II) $\gamma > 10$

Under these conditions, the time constant involved in the voltammetric measurements is much higher than the characteristic time involved in the internal diffusion. In this case, the obtained voltammetric charge (after correction of the double layer charging) corresponds to all the wetted 3D surface of the coating. This point will be treated in more detail in chapter 4.

3.5   Discussion

In order to estimate the real (working) electrode area, which indeed participates in the electrochemical reaction under investigation, the effectiveness factor, E_f, is defined. For the estimation of the effectiveness factor, E_f, two main approaches have been used: An analytical and a qualitative approach. The analytical approach can allow the estimation of the effectiveness factor, E_f, considering two simplifying conditions: One is the constant concentration of the electroactive species within the DSA$^®$ coating and another one is the constant overpotential within the coating.

In the qualitative approach two dimensionless parameters have been defined allowing the estimation of the effectiveness factor under transient conditions.

In this discussion, we will show that the same differential equation governs all the studied cases.

- **Constant concentration**

Due to the micro and macroporosity of the investigated DSA$^®$ coating, two configurations have been used: One is the spherical particle configuration (SPC) related to the microporosity and another one is the cylindrical pore configuration (CPC) related to macroporosity.

Considering that the electronically conductive phase of the coating is equipotential, one can obtain for both, the SPC and CPC configurations, the following differential Equation:

$$\frac{d^2\eta(X)}{dX^2} - K^2\eta(X) = 0 \qquad (3.17)$$

Equation (3.17) is a second order linear ordinary differential equation which after solving it gives:

$$\frac{\eta(X)-\eta(0)}{\eta(1)-\eta(0)} = \frac{\cosh(KX)-1}{\cosh(K)-1} \qquad (3.29)$$

The dimensionless number, K^2, includes parameters like the morphology (a_p, ε, L, for the SPC configuration and N_p, d for the CPC configuration), the apparent electrolyte conductivity (γ), and the kinetics of the investigated electrochemical reaction (j_0).

Furthermore, K^2 is also related to two resistances: Charge-transfer resistance, R_{ct}, and ohmic resistance, R_Ω, with Equation (3.22):

$$K^2 = \frac{R_\Omega}{R_{ct}} \qquad (3.22)$$

Finally, the effectiveness factor, E_f, of the DSA$^{\circledR}$ coating can be calculated from K.

$$E_f = \frac{\tanh(K)}{K} \tag{3.32}$$

This effectiveness factor will allow us to estimate the fraction of the surface coating which participates effectively in the investigated reaction.

The K values of the two used configurations are:

SPC configuration:

$$K_1^2 = \frac{1}{\gamma} L^2 j_0 \frac{F}{RT} (1-\varepsilon) a_p \tag{3.18}$$

and CPC configuration:

$$K_2^2 = \frac{1}{\gamma} L^2 j_0 \frac{F}{RT} \pi N_p d \tag{3.37}$$

From the comparison of Equations (3.18) and (3.37), the equivalence of the two configurations is formulated as:

$$(1-\varepsilon) \cdot a_p = \pi \cdot N_p \cdot d \tag{3.71}$$

In fact, using Equation (3.71), both the microporosity and macroporosity can be treated as one global porosity.

- **Constant overpotential**

As the two configurations (where K_1 and K_2 participate) are equivalent, we consider only the CPC configuration:

$$\frac{d^2 C_A}{dX^2} - \frac{4k_e L^2}{D_A d} C_A = 0 \tag{3.51}$$

This equation is analogous to Equation (3.17) when replacing η by C_A, and K^2 by m, where:

$$K^2 = m = \sqrt{\frac{4k_e L^2}{D_A d}} \tag{3.72}$$

where: in this case m is the Thiele modulus ($K^2 = m$).

Similarly to Equation (3.32), the effectiveness factor, E_f, of the DSA® coating is given by:

$$E_f = \frac{\tanh(m)}{m} \tag{3.62}$$

3.6 Conclusions

This chapter concludes in:

- Two configurations have been used in order to describe the micro and macroporosity of a DSA® coating,
- An analytical approach has been developed for both configurations under two different simplifying conditions: Constant concentration and constant overpotential,
- In the analytical approach, the effectiveness factor, E_f, has been described using the dimensionless parameters K^2 (for constant concentration) and m (for constant overpotential),

- Even if similar approaches have been used in other fields, it is the first time that the effectiveness factor, E_f, has been adapted in electrocatalysis, particularly for DSA® electrode applications,

- Two dimensionless numbers (Equations (3.66) and (3.67)), relating the time constant involved in the voltammetric measurements, internal diffusion and charge-transfer reaction, have been defined for the qualitative estimation of the effectiveness factor, E_f, from voltammetric measurements (LSV or CV). Extreme cases are discussed,

- For the qualitative estimation of the real surface area of the coating from voltammetric charge measurements, the charging of the IrO_2 coating during the CV measurements can be treated. In this charging process, protons diffuse and react with the oxide through the coating according to reaction (3.69),

- Considering that the electrochemical reaction is much faster than proton diffusion within the coating, the only parameter which controls the charging process is the dimensionless parameter, γ, (Equation (3.67)), with two extreme (arbitrary) situations:

I) $\gamma < 0.1$

In this case, the obtained voltammetric charge (after correction of the double layer charging) corresponds to the wetted 2D surface.

II) $\gamma > 10$

In this case, the obtained voltammetric charge (after correction of the double layer charging) corresponds to all the wetted 3D surface of the coating.

3.7   References

1.   F. Coeuret, D. Hutin, A. Gaunand, *J. Appl. Electrochem.*, 1976, **6**, 417-423.
2.   O. Levenspiel, *Chemical Reaction Engineering*, Wiley Eastern Limited, 2nd. Edition, New Delhi, 1972, 473.
3.   S. Trasatti, *Electrochim. Acta*, 2000, **45**, 2377-2385.

Chapter 4

Morphological and electrochemical characterization of the Ti/IrO$_2$ electrode

In this chapter the voltammetric charge obtained from cyclic voltammetry (CV) measurements will be presented using different potential scan rates, potential windows, and temperatures for various Ti/IrO$_2$ loadings. A model will be proposed in order to explain the influence of temperature and scan rates on the voltammetric charge, q^*. Both the outer-inner surface model (Trasatti model) and the three capacitance model (Takasu model) have been considered in this model.

4.1   Introduction

The electrochemical surface properties of the DSA$^®$ electrodes play an important role in their electrocatalytic behaviour. Transient techniques, like cyclic voltammetry, are usually used for the investigation of the involved surface reactions.

For reversible surface process (fast process), the obtained cyclovoltammogram shows horizontal symmetry (see Figure 4.1a). On the contrary, for an irreversible surface process (slow process), the obtained cyclovoltamograms are asymmetric (see Figure 4.1b).
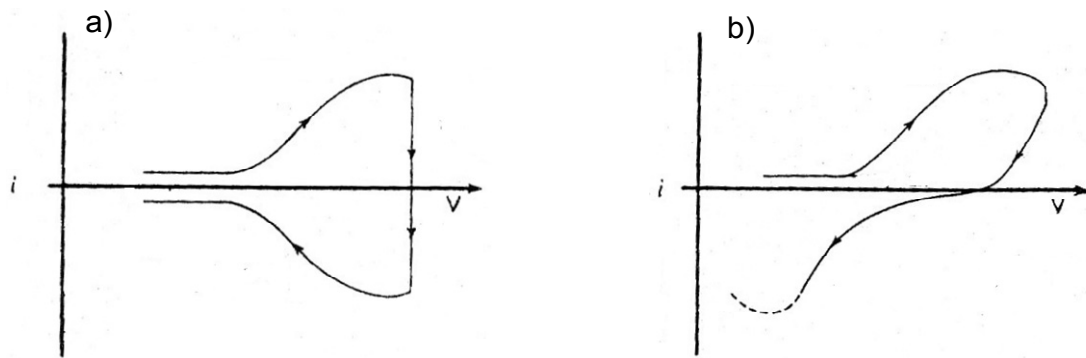
Figure 4.1: Schematic representation of cyclovoltammograms: (a) Reversible process (fast) and (b) irreversible process (slow) [1].

The majority of the papers dealing with measurement of the voltammetric charge q^* report on investigations of Ti/RuO₂ electrodes. Two main approaches have been elaborated in order to explain the origin of the voltammetric charge and to elucidate the dependence of q^* on scan rate:

a) According to Trasatti [2], the anodic and cathodic surface activities involved in the cyclovoltammograms of a Ti/RuO₂ electrode (see Figure 4.2) correspond to a transition in the oxidation state of surface Ru ions accompanied by proton exchange with the solution according to reaction (4.1).

$$RuO_x(OH)_y + \delta H^+ + \delta e^- \underset{anodic}{\overset{cathodic}{\rightleftharpoons}} RuO_{x-\delta}(OH)_{y+\delta} \qquad (4.1)$$
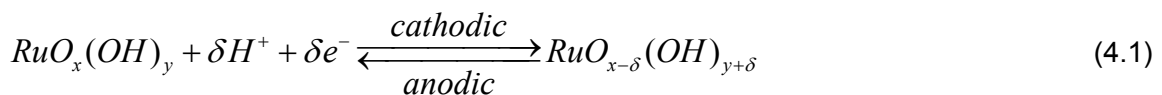
As a whole, reaction (4.1) resembles the protonation-deprotonation of the oxide surface, i.e. the oxide behaves as a "protonic condenser".
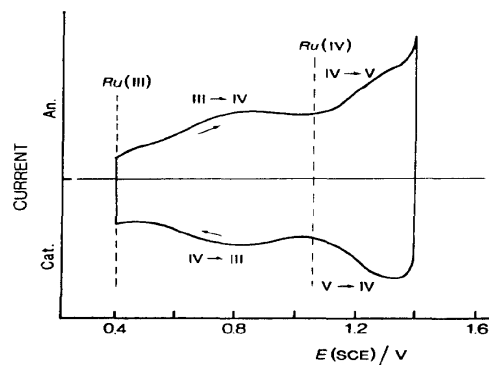
Figure 4.2: Cyclovoltammogram of a supported RuO₂ electrode [2]. Scan rate: 50 mV/s.

The integration of the cyclovoltammogram provides the voltammetric charge, q^*, measuring the amount of protons exchanged. According to [2], since proton exchange takes place at surface active sites, q^* can be regarded as a measure of the electrochemically active surface area.

It is necessary to notice here that q^* cannot be directly compared for two different oxides since the nature of the surface redox sites is different.

Trasatti et al. [3] have shown that the overall voltammetric charge can be divided into a fast charge, due to the charging of the outer surface area of the electrode, and a slow charge, due to less accessible surface regions (loose grain boundaries, pores, cracks…), which become progressively excluded as the scan rate is enhanced. This implies that a fraction of available surface sites exchanges protons with more difficulty during the determination of q^*. It has also been suggested that the involved surface reactions in Equation (4.1) are limited by slow diffusion of proton-donating species to the reacting sites of the oxide.

b) In order to explain the dependence of q^* on scan rate observed for the Ti/RuO$_2$ electrode, Takasu et al. [4] have proposed a model according to which the voltammetric charge is the contribution of three components resulting in three capacitances: The double-layer capacitance, C_{dl}, which is independent of the scan rate, the adsorption capacitance, C_{ads}, and the capacitance due to surface redox activity considered as a slow and irreversible process, C_{irr}. Both C_{ads} and C_{irr} decrease with increasing scan rate. In fact, at low scan rates (i.e. 5mV/s) all three capacitances have a significant contribution to the total capacitance contrary to high scan rates (i.e. 500mV/s) where C_{dl} dominates (see Figure 4.3).
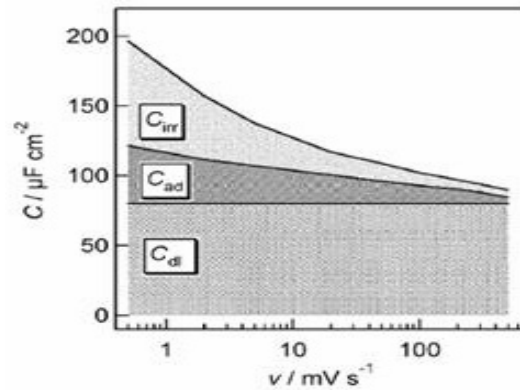
Figure 4.3: Contribution of the three specific capacitances at various scan rates. C_{dl}: double-layer capacitance, C_{ads}: adsorption capacitance and C_{irr}: irreversible redox surface capacitance [4].

In this work, the electrochemical surface properties of the Ti/IrO₂ electrode have been investigated by cyclic voltammetry using different potential windows, scan rates, IrO₂ loadings and temperatures. This is the first time that the influence of temperature on q^* has been investigated.

4.2   Experimental

a) Preparation of the Ti/IrO₂ electrodes

The Ti/IrO₂ electrodes have been prepared by the thermal decomposition technique using H_2IrCl_6 as precursor. The IrO₂ deposit was located inside a circular slot (ø= 15mm, h= 0.5mm) on a Ti plate (25 x 25mm). The geometric (projected) area of the electrode was 1.77cm².

The following steps are involved in this preparation technique:

- Sandblasting of the Ti substrate using abrasive particles type BR 3080,
- Rinsing with ultrapure water,
- Treatment in 1M oxalic acid during 1 hour at 95-100°C,
- Rinsing with ultrapure water,

- Deposition of $30\mu l$ of the precursor solution 46mM $H_2IrCl_6 \cdot xH_2O$ (ABCR 99.9%) in isopropanol (Fluka 99.5%), using a micropipette (Eppendorf).

- Treatment in a drying oven (Heraeus) during 10 min at 70°C (evaporation of the solvent),

- Treatment in a furnace (Solo 111.10/9/20) during 10 min at 500°C,

- Weighing the sample using a Mettler AE163 analytical balance,

- The last four steps are repeated until reaching the desired loading, and finally

- Treatment in the furnace during 1 hour at 500°C.

The amount of water in the chemical used ($H_2IrCl_6 \cdot xH_2O$) as precursor being unknown, the exact concentration of H_2IrCl_6 in the precursor solution was determined from the weight increase, taking as reference the 20 step deposition (see Table 4.1).

Four electrodes with different loading have been prepared and denoted as E_ℓ where subscript ℓ refers to the loading in mg IrO_2/cm^2. For instance, $E_{0.28}$ means that 0.28mg/cm^2 of IrO_2 has been deposited on the Ti substrate. These electrodes are presented in Table 4.1.

Table 4.1: Characteristics of the electrodes prepared by the controlled volume deposition technique

Deposition steps		2	5	10	20
Loading [mg IrO_2/cm^2]	calculated	0.35 ± 0.01	0.87 ± 0.03	1.75 ± 0.06	3.50 ± 0.12
	measured	0.28 ± 0.12	0.90 ± 0.12	1.70 ± 0.12	3.50 ± 0.12
Electrode label		$E_{0.35}$	$E_{0.87}$	$E_{1.75}$	$E_{3.50}$

This table shows that there is a reasonably good agreement between the values calculated from the deposited volume and those measured by increase in weight.

b) Microscopy and diffraction techniques

In this section the different techniques used for the morphological characterization of the Ti/IrO_2 electrodes are presented.

a) High Resolution Scanning Electron Microscopy (HRSEM)

A Philips XL30 SFEG microscope has been used in HRSEM analysis, operating at a field emission of 1-30kV. Analyses were carried out at the Interdisciplinary Centre of Electron Microscopy (CIME) at the EPFL.

b) X-Ray Diffraction (XRD)

A Siemens D500 Powder Diffractometer has been used. Measurements were performed using the K_α Cu ray (1.54 Å) using slits of 1°/1°/1°/0.05° over the 5-90° range, a step of 0.04°, and a resolution of 4 sec/step. XRD measurements were carried out at the Laboratory of Ceramics (IMX-LC), EPFL.

c) Cyclic voltammetric (CV) measurements

In a single-compartment, three-electrode cell (50 ml) made of Teflon, the following electrodes have been used: Ti/IrO₂ electrodes ($E_{0.35}, E_{0.87}, E_{1.75}, E_{3.50}$) with exposed geometric area of 0.785cm^2 as working electrode (WE), Pt wire (Goodfellow 99.99%) as counter electrode (CE), and a mercurous sulfate electrode (MSE: $Hg/Hg_2SO_4/K_2SO_4$sat., Radiometer REF621; 0.64V vs. SHE) as reference electrode (RE). A constant distance of 1mm was kept between the reference and working electrode.

In the CV measurements, the potential is varied linearly with time between potential limits of [-0.4; +0.4], [-0.4; +0.7] and [-0.7; +0.7] V/MSE and the resulting current is measured for both the forward and the reverse scan. The used scan rates lie between 5-500mV/s. This technique has been mainly used for the determination of the voltammetric charge. The electrochemical measurements were carried out in a three-electrode cell using a computer controlled EcoChemie potentiostat (model Autolab$^®$ PGSTAT 30). The setup is illustrated in Figure 4.4.

The measurements were performed at room temperature using 1M HClO₄ (Riedel-de-Haën 70%). The solutions were prepared in ultrapure (Millipore$^®$) water and with analytical grade reagents without further purification. All potentials are expressed here with respect to the mercurous sulfate electrode (MSE). The current density and the voltammetric charge have been reported relative to the geometric (projected) area.
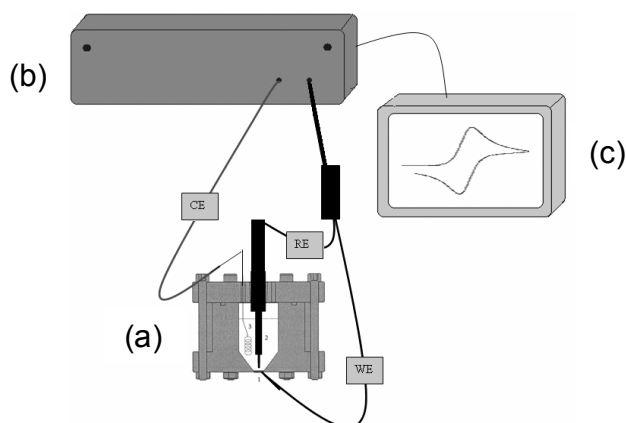
Figure 4.4: Illustration of the used equipment composed of: (a) electrochemical cell, (b) potentiostat Autolab® PGSTAT 30, and (c) computer. Electrochemical cell: Working electrode (WE), reference electrode (RE) and counter electrode (CE).

4.3 Results and discussion

4.3.1 Morphological characterization of Ti/IrO$_2$ electrodes

a) High Resolution Scanning Electron Microscopy (HRSEM)

Figures 4.5a and b shows SEM and HRSEM images of a Ti/IrO$_2$ electrode directly after preparation.
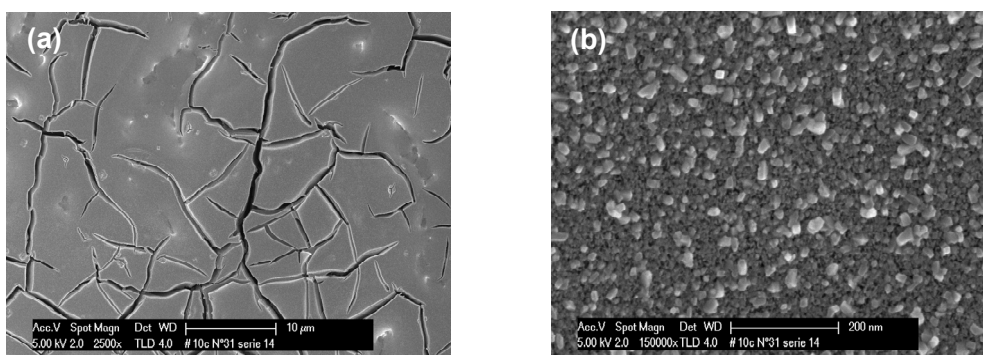
Figure 4.5: HRSEM images of a Ti/IrO$_2$ (E$_{1.75}$) electrode at: (a) Low magnification and (b) high magnification.

Figure 4.5a shows that the Ti/IrO$_2$ electrode exhibits a cracked dried-mud look which is the typical structure of DSA® electrodes. Figure 4.5b shows, however, that the surface is composed of fine IrO$_2$ particles down to few nanometers in diameter. Hence, the electrode exhibits at the same time microporosity and macroporosity.

The microporosity part of the coating is characterized using the SPC configuration by the porosity of the coating (estimated with ε = 0.26 for a monodisperse spherical compact coating) and the diameter of the particle (estimated with d_p = 2nm) to give $(1-\varepsilon)a_p$ = 2x10^7 cm^{-1}.

The equivalence between the observed cracked structure and the SPC configuration is given by equation (4.2):

$$(1-\varepsilon)a_p = 2L_{sp} \tag{4.2}$$

where: L_{sp} is the specific length of the cracks per unit surface [cm^{-1}]. Based on Figure 4.5b, the estimated value of $2L_{sp}$ is 5x10^3 cm^{-1}.

It is seen that the contribution of the macroporosity due to cracks ($2L_{sp}$ = 5x10^3 cm^{-1}) is negligible compared to the microporosity due to fine particles ($(1-\varepsilon)a_p$ = 2x10^7 cm^{-1}).

b) X-Ray Diffraction (XRD)

Figure 4.6 shows a typical X-Ray diffractogram of a Ti/IrO$_2$ electrode.

56
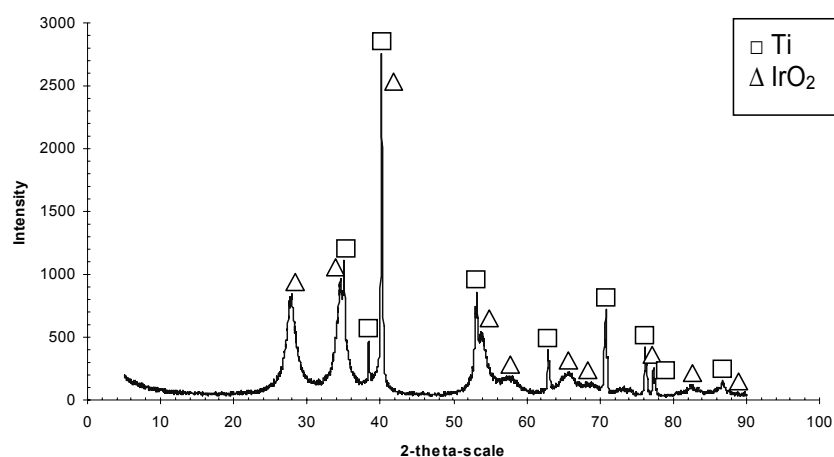
Figure 4.6: X-Ray diffraction pattern of a Ti/IrO$_2$ (E$_{1.75}$) electrode.

The peak positions (2θ), atomic distances (d, Å), and intensities were compared to the ASTM (American Standards for Testing and Materials) reference for IrO$_2$ (no. 88-0288) and Ti (44-1294), (see Appendix).

Figure 4.6 shows that the peaks associated with IrO$_2$ and metallic Ti are present; there are no peaks indicating the presence of TiO$_2$. The narrowness of the IrO$_2$ peaks is an indication of the high crystallinity of the coating.

4.3.2 Cyclic voltammetric characterization of Ti/IrO$_2$ electrodes

In this section, Ti/IrO$_2$ electrodes of different loading are characterized on the basis of cyclic voltammetric experiments performed in the potential region of water stability with potential window, potential scan rate and temperature as variables.

a) Influence of the potential window at different scan rates

Figure 4.7 shows cyclic voltammograms obtained with the Ti/IrO$_2$ (E$_{0.35}$) electrode using different potential windows and scan rates. The current in these voltammograms has been normalised by the IrO$_2$ loading.
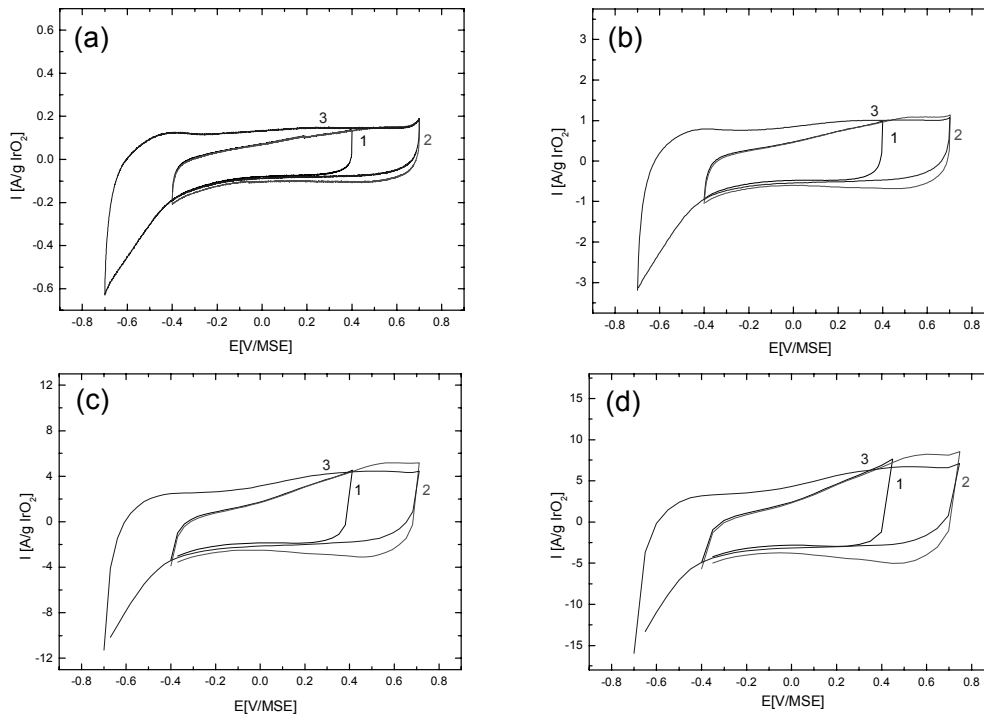
Figure 4.7: Cyclic voltammograms of the electrode of Ti/IrO$_2$ (E$_{0.35}$), at different scan rates: (a) 5, (b) 50, (c) 300 and (d) 500mV/s, and for different potential windows between: (1) -0.4 and +0.4V, (2) -0.4 and +0.7V, (3) -0.7 and +0.7V. Electrolyte: 1M HClO$_4$. T= 25°C.

For all the investigated potential windows and scan rates the obtained cyclic voltammograms do not show any horizontal symmetry. This is an indication that the involved surface redox reactions are slow.

Figure 4.7 also shows that the anodic current between -0.4 and 0.7 V is not dependent on the fixed upper limit (0.4 or 0.7 V) when the lower cut-off was fixed at -0.4 V, while it is clearly higher when the lower cut-off potential was set to -0.7 V. Furthermore, the cathodic current increases strongly in the potential region between -0.4 and -0.7 V. This shows that the involved surface process in the potential region between -0.4 and -0.7 V is irreversible (slow process).

Furthermore, the fact that the ratio between the anodic q^+ and cathodic q^- charges,

$\dfrac{q^+}{q^-}$, determined from Figure 4.7 and reported in Table 4.2, is close to unity (for all the

investigated potential windows and scan rates) shows that the large cathodic current

58

observed between -0.4 and -0.7 V is completely regained over the whole anodic range during the anodic sweep.

Table 4.2: Anodic and cathodic charges obtained by integration of the cyclic voltammograms of Figure 4.7, and their ratio in absolute value, for different potential windows and potential scan rates. Electrode type: Ti/IrO$_2$ ($E_{0.35}$).

Potential window [V]	Charge [mC]	Potential scan rate [mV/s]		
		50	300	500
-0.4 to 0.4	q^+	2.18	1.53	1.54
	q^-	-2.31	-1.51	-1.46
	$\dfrac{q^+}{q^-}$	**0.94**	**1.01**	**1.06**
-0.4 to 0.7	q^+	3.89	2.86	2.80
	q^-	-3.96	-2.81	-2.70
	$\dfrac{q^+}{q^-}$	**0.98**	**1.02**	**1.04**
-0.7 to 0.7	q^+	6.24	4.07	3.63
	q^-	-6.58	-4.09	-3.65
	$\dfrac{q^+}{q^-}$	**0.95**	**0.99**	**0.99**

b) Effect of temperature

Figure 4.8 shows the variation of voltammetric charge q^* with scan rate at different operating temperatures. This figure shows that the effect of temperature on the voltammetric charge is more pronounced at low scan rates.
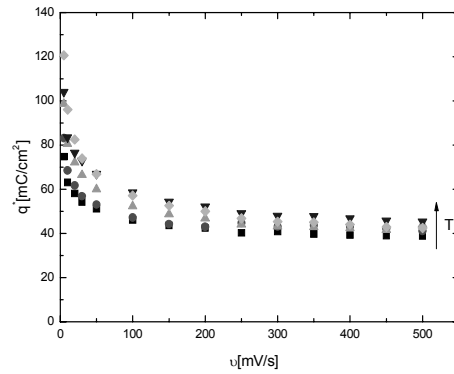
Figure 4.8: Variation of voltammetric charge q^* with scan rate at different operating temperatures: 12, 30, 50, 60, and 70°C. Potential window: -0.7 to +0.7V. Electrolyte: 1M $HClO_4$. Electrode: Ti/IrO₂ ($E_{0.87}$).

The apparent activation energy, E_a^{app}, as a function of the scan rate, is shown in Figure 4.9.
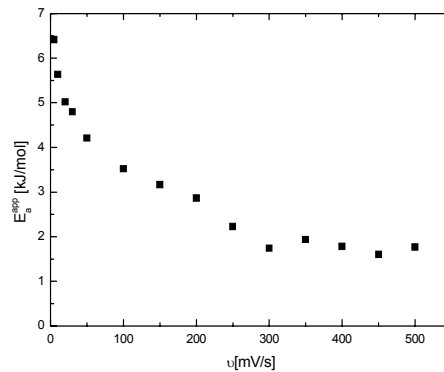
Figure 4.9: Apparent activation energy E_a^{app} as a function of the scan rate. Electrode and experimental conditions as in Figure 4.8.

Figure 4.9 shows the variation of the apparent activation energy, E_a^{app}, (determined from Arrhenius equation) with the potential scan rate. E_a^{app} decreases from 6.4kJ/mol at low scan rates to 1.8kJ/mol at high scan rates.

From these measurements, we can consider that two main contributions are involved in the voltammetric charge:

a) A contribution related with a fast (instantaneous) process with zero activation energy. This process dominates at high scan rates.

b) A contribution related with a slow process with activation energy of about 10 kJ/mol. This process dominates at low scan rates.

It is proposed that the fast (instantaneous) contribution with zero activation energy is due to an electrostatic phenomenon related to the charging of the electrical double layer at the electrode-electrolyte interface, and corresponds to the double-layer capacitance C_{dl}. The slow process with activation energy of about 10 kJ/mol (see Figure 4.13) is due to a physical phenomenon related to the diffusion of protons to the reacting sites of the oxide according to equation (4.3).

c) Effect of scan rate

Figure 4.10 shows the variation of the voltammetric charge q^* (referred to 1cm^2 geometric area) with the scan rate for different loadings and potential windows obtained in 1M HClO$_4$ at 25°C.
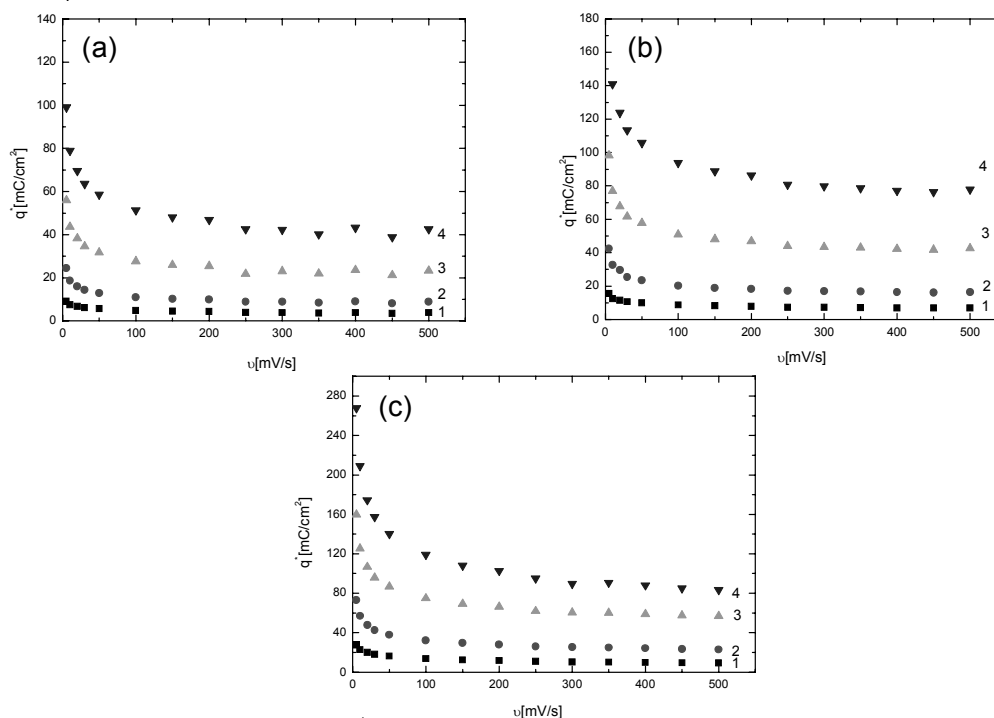
Figure 4.10: Dependence of q^* on the potential scan rate for the potential windows between: (a) -0.4 and +0.4, (b) -0.4 and +0.7, (c) -0.7 and +0.7V, and for different loadings: (1) $E_{0.35}$, (2) $E_{0.87}$, (3) $E_{1.75}$, (4) $E_{3.50}$. Electrolyte: 1M HClO$_4$. T= 25°C.

As expected, the voltammetric charge for all investigated loadings and potential windows decreases with the scan rate, a rapid initial decrease being followed by stabilization at high scan rates. Furthermore, q^* increases with increasing electrode loading.

Two main approaches can be used in order to explain this behaviour: The first approach proposed by Trasatti et al. [3] is based on the accessibility to the active sites of the electrode. The decrease of the voltammetric charge with the scan rate is explained by the exclusion of the inner part of the electrode (as the scan rate is enhanced) due to the slow diffusion of protons through the porous structure of the electrode. The voltammetric charge has been attributed to the redox surface couples according to the Faradaic reaction (4.3).

$$IrO_x(OH)_y + \delta H^+ + \delta e^- \xleftrightarrow[anodic]{cathodic} IrO_{x-\delta}(OH)_{y+\delta} \tag{4.3}$$
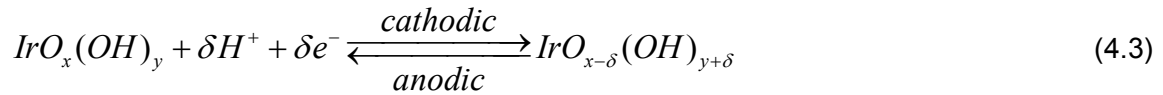
The second approach is proposed by Takasu et al. [4]. This approach is based on the presence of mainly two types of capacitances: The double-layer capacitance, C_{dl} (non-Faradaic fast process) which dominates at high scan rates and a redox surface capacitance (Faradaic slow surface process) which contributes only at low scan rates. The decrease of the voltammetric charge with the scan rate is explained by the slow and irreversible behaviour of the redox surface capacitance resulting in its exclusion at high scan rates.

The apparent activation energy measurements as a function of scan rate (Figure 4.9) have allowed us to consider a slightly different model. In fact, we consider that the total charge is due to two contributions:

a) One contribution is due to the double-layer charging (q_{dl}^*). This charging process dominates at high scan rates and is scan rate independent.

b) Another contribution is due to surface redox activities in the coating (q_{redox}^*), according to the Faradaic reaction (4.3). This charging process dominates at low scan rates and depends on the square root of scan rate ($\upsilon^{0.5}$).

In order to estimate q_{dl}^*, the voltammetric charge should be measured under conditions where the time constant involved in the voltammetric measurements is much lower than the time constant involved in the internal diffusion (see section 3.4.2) given by:

$$\gamma = \frac{\Delta E \cdot D_{eff}}{\upsilon \cdot L^2} < 0.1 \tag{3.70}$$

In order to satisfy this condition and considering an effective volume diffusion coefficient within the coating, $D_{eff} = 10^{-7}$ cm^2/s (estimated value), $\Delta E = 1.4$ V, and $L = 10^{-4}$ cm, voltammetric measurements should be made with a scan rate higher than 140V/s. For lack of such experiments, q_{dl}^* is estimated by extrapolation as follows.

For the determination of q_{dl}^* from Figure 4.10, a relation given by Trasatti et al. [3], (equation (4.4)) has been adapted and presented in Figure 4.11:

$$q^*(\upsilon) = q_{dl}^* + const\left(\frac{1}{\upsilon^{1/2}}\right) \tag{4.4}$$

From Figure 4.11, q_{dl}^* has been determined by extrapolation to $\dfrac{1}{\upsilon^{1/2}} \to 0$.
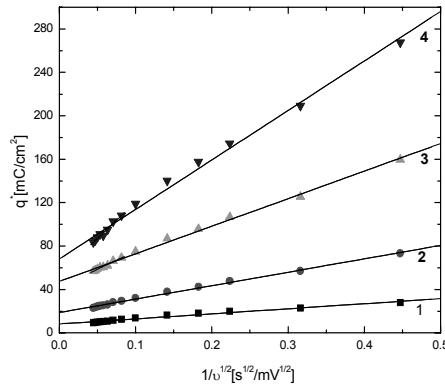
Figure 4.11: Graphical representation of Equation (4.4) for the determination of q_{dl}^* by extrapolation. Potential window: -0.7 to +0.7V. Electrodes: (1) $E_{0.35}$, (2) $E_{0.87}$, (3) $E_{1.75}$, (4) $E_{3.50}$. Electrolyte: 1M HClO$_4$. T= 25°C.

Figure 4.12 shows q_{dl}^* as a function of IrO$_2$ loading and temperature.
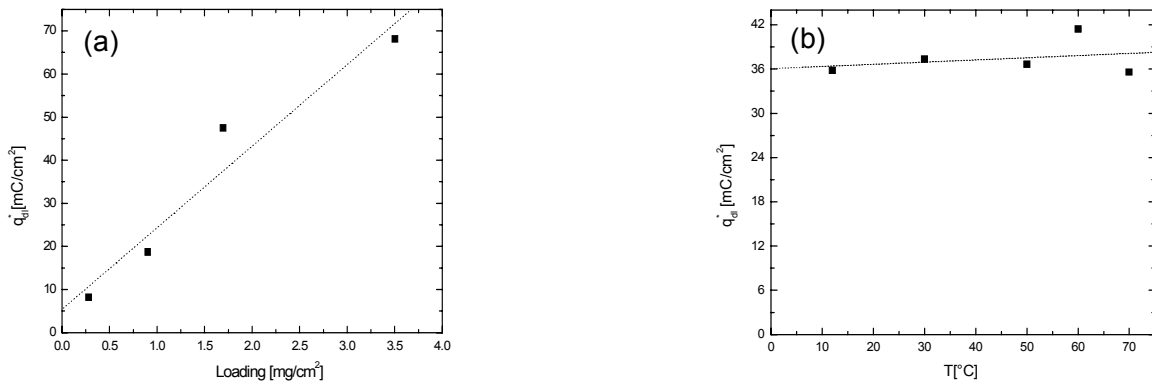
Figure 4.12: (a) Variation of q_{dl}^* with the IrO$_2$ loading, (b) variation of q_{dl}^* with temperature for the electrode Ti/IrO$_2$ ($E_{0.87}$). Experimental conditions as in Figure 4.11.

Figures 4.12 shows that q_{dl}^* increases with the IrO$_2$ loading, and as expected, it is almost independent of the temperature.

The effective activation energy, E_a^{eff}, for q_{redox}^* has been calculated by plotting $q^*(\upsilon) - q_{dl}^*$ at all scan rates as a function of $\dfrac{1}{T}$ (Arrhenius plot). The obtained values have been reported as a function of scan rate (see Figure 4.13).
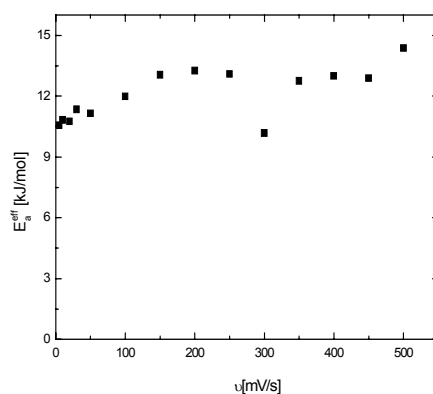
Figure 4.13: Effective activation energy E_a^{eff} for q_{redox}^* as a function of the scan rate υ. Potential window: -0.7 to +0.7V. Electrolyte: 1M HClO$_4$. Electrode Ti/IrO$_2$ ($E_{0.87}$).

Figure 4.13 shows the variation of this effective activation energy E_a^{eff} for q_{redox}^* with scan rate for one of the investigated electrodes, $E_{0.87}$. This figure shows that the $E_a^{eff} \approx$ 10kJ/mol and this confirms that q_{redox}^* is related to a physical process, certainly diffusion of protons through the coating.

4.3.3 Determination of the real surface area of the electrode

The calculated q_{dl}^* and q_{redox}^* in the previous section can be regarded as a measure of the electrochemically active surface area of the coating. However, one must be cautious when determining the real surface area from these voltammetric charges q_{dl}^* and q_{redox}^* because they depend on several experimental parameters like:

- The scan rate for q_{redox}^*,
- The potential domain used in the cyclic voltammetric measurements,
- The pH of the used electrolyte.

Furthermore, this technique has no universal significance since q_{dl}^* and q_{redox}^* have only empiric validity. Nevertheless, this method is useful for an internal comparison within

the Ti/IrO$_2$ electrodes, provided that the technique is normalized to appropriate experimental conditions. In addition, the technique should be calibrated using other methods for the determination of the surface area.

Savinell et al. [5] have taken into consideration all these facts and have related the voltammetric charge of Ti/IrO$_2$, obtained at 20mV/s in 1M H$_2$SO$_4$, potential range within 0.05-1V vs. SCE (saturated calomel electrode), with the surface area of the electrode measured by Zn^{2+} ion adsorption. The obtained values under the used experimental conditions are:

- Specific charge (q_{sp}^{*}) (anodic or cathodic): q_{sp}^{*} = 31.1 $\pm$ 2.9 mC/mg IrO$_2$

- Specific surface area (a_{sp}): a_{sp} = 101.5 $\pm$ 6.4 cm^2/mg IrO$_2$

Even if these voltammetric charge values are not related directly to q_{dl}^{*} and q_{redox}^{*}, we can use them for the estimation of the real surface area of the Ti/IrO$_2$ electrodes prepared in this work. To do this, we have chosen similar operating conditions to those used in Ref. [5] (same pH and scan rate). Figure 4.14a shows cyclovoltammograms obtained in 1M HClO$_4$ at 20mV/s for different loadings and Figure 4.14b shows the variation of both q^{+} and q^{-} with the loading. From the slope, we can calculate a specific charge of 24$\pm$ 3 mC/mg IrO$_2$.
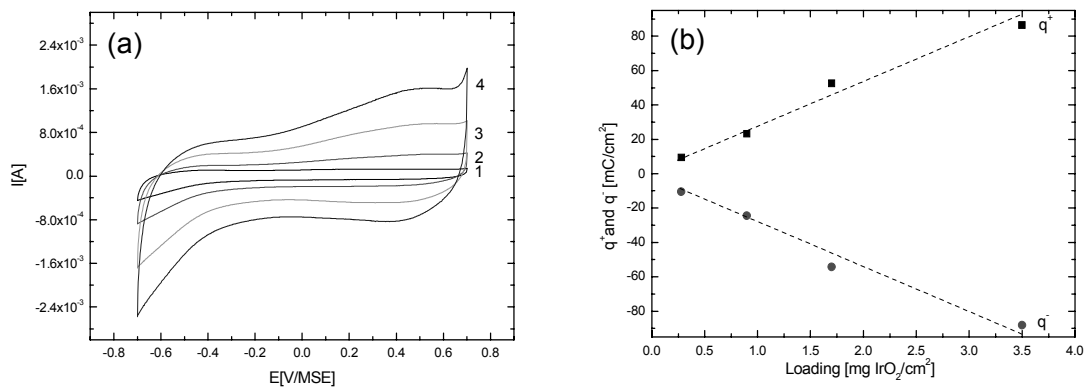
Figure 4.14: (a) Cyclic voltammogram of the Ti/IrO$_2$ electrodes (1: E$_{0.35}$, 2: E$_{0.87}$, 3: E$_{1.75}$, 4: E$_{3.50}$) and (b) anodic q^{+} and cathodic q^{-} charge vs. the IrO$_2$ loading. Scan rate: 20mV/s. Electrolyte: 1M HClO$_4$. T=25°C.

As this value is close to that obtained by Savinell et al. [5], we can use the specific surface area determined by these authors (101.5 ± 6.4 cm^2/mg IrO$_2$) for the estimation of the three dimensional roughness factor, γ_{3D}, of the Ti/IrO$_2$ electrodes prepared in this work, using the relation (4.5):

$$\gamma_{3D} = m_{sp} \cdot a_{sp}$$

(4.5)

where: a_{sp} is the specific surface area (=101.5 cm^2/mg IrO$_2$) of the coating and m_{sp} is the specific loading [mg IrO$_2$/cm^2].

4.3.4 Estimation of the three dimensional roughness factor (γ_{3D}) of the IrO$_2$ coatings from the morphology of the coating

The three dimensional roughness factor, γ_{3D}, is directly related to the morphological parameters of the coating. In fact, considering the IrO$_2$ coating as a packing of uniform size spherical particles of diameter, d_p, wetted surface area, A_w, geometric (projected) area, A_g, the three dimensional roughness factor, γ_{3D}, can be expressed as:

$$\gamma_{3D} = \frac{A_w}{A_g} = \frac{S_p}{V_p}(1-\varepsilon)\cdot L = \frac{6}{d_p}(1-\varepsilon)\cdot L$$

(4.6)

where: S_p and V_p are, respectively, surface and volume of one particle, ε is the volume fraction of pores in the film and L the film thickness.

The 3D roughness factor of the IrO$_2$ coating can be estimated from experimental data using the relation:

$$\gamma_{3D} = 1000 \cdot a_{sp} \cdot \rho \cdot (1-\varepsilon)\cdot L$$

(4.7)

where: a_{sp} [cm²/mg IrO₂] is the specific area of the IrO₂ coating and ρ [g/cm³] is the bulk density of IrO₂.

From Equations (4.6) and (4.7), the particle diameter is calculated with equation (4.8):

$$d_p = \frac{6}{1000 \cdot a_{sp} \cdot \rho}$$
(4.8)

while the thickness of the film L can be estimated from the specific IrO₂ loading, m_{sp} [mg/cm²], with equation (4.9):

$$L = \frac{m_{sp}}{1000 \cdot \rho \cdot (1 - \varepsilon)}$$
(4.9)

4.4   Conclusions

This chapter concludes in:

- Using Ti/IrO₂ electrodes, we have found that two main contributions are involved in the voltammetric charge: The first contribution is related to a fast process with zero activation energy and the second is related to a slow process with an effective activation energy, E_a^{eff}, of about 10 kJ/mol. The fast process has been related to the charging of the electrical double layer which corresponds to the double-layer capacitance (C_{dl}), while the slow process has been related to the diffusion of protons to the reacting sites of the oxide,

- The experimental values of the specific charge, q_{sp}^{*}, obtained in this work (24 ± 3 mC/mg IrO₂) are similar to those from Savinell et al. [5] (31.1 ± 2.9 mC/mg IrO₂). These authors have used the Zn²⁺ ion adsorption technique for the determination of the real surface area. Therefore, we can use the specific surface area determined by these authors (a_{sp} = 101.5 ± 6.4 cm²/mg IrO₂) for the estimation of the three-dimensional

roughness factor, γ_{3D}, of the Ti/IrO$_2$ electrodes prepared in this work using the relation: $\gamma_{3D} = m_{sp} \cdot a_{sp}$.

4.5   References

1.   H. Angerstein-Kozlowska, B. E. Conway, and W. B. A. Sharp, *Electroanal. Chem. Interfac. Electrochem.*, 1973, **43**, 9-36.

2.   S. Trasatti, *Mat. Chem. Phys.*, 1987, **16**, 157-174.

3.   S. Ardizzone, G. Fregonara, and S. Trasatti, *Electrochim. Acta*, 1990, **35**, 263-267.

4.   W. Sugimoto, T. Kizaki, K. Yokoshima, Y. Murakami and Y. Takasu, *Electrochim. Acta*, 2004, **49**, 313-320.

5.   R. F. Savinell, R. L. Zeller, and J. A. Adams, *J. Electrochem. Soc.*, 1990, **137**, 489-494.

Appendix

Crystallographic data of the Ti/IrO$_2$ electrode ($E_{1.75}$) compared to the ASTM reference.

Results hkl d, Å 2-theta	Intensity	Literature ASTM IrO$_2$ (88-0288) hkl d, Å 2-theta	Intensity	Literature ASTM Ti (44-1294) hkl d, Å 2-theta	Intensity
27.96	30.69	27.986	100		
110		110			
3.1049		3.185			
34.92	31.41	34.656	90		
101		101			
2.5		2.586			
35.04	40.43			35.094	25
100				100	
2.491				2.555	
38.4	16.81			38.422	30
002				002	
2.28				2.341	
40.16	100	39.994	25		
200		200			
2.184		2.252			
40.16	100			40.171	100
101				101	
2.184				2.243	
53.2	31.01			53.005	13
102				102	
1.675				1.726	
54	18.4	53.935	53		
211		211			
1.652		1.698			
58.12	6.086	58.385	7		
002		002			
1.544		1.579			
62.92	14.49			62.951	11
110				110	
1.437				1.475	
65.56	7.39	65.589	6		
65.64	7.43	65.967	13		
69.16	3.7	69.218	12		
70.84	26.3			70.662	11
103				103	
1.294				1.332	
76.2	15.25			76.221	9

Results		Literature ASTM		Literature ASTM	
hkl		IrO$_2$ (88-0288)		Ti (44-1294)	
d, Å		hkl		hkl	
2-theta	Intensity	d, Å		d, Å	
		2-theta	Intensity	2-theta	Intensity
112				112	
1.215				1.248	
76.56	3.37	76.594	1		
77.36	9.24			77.37	6
201				201	
1.2				1.232	
83.16	2.65	83.055	9		
86.36	4.75			86.762	1
86.64	4.35	86.765	5		

Chapter 5

Voltammetric characterization of Ti/IrO$_2$ electrodes with a fast reaction (Fe^{3+}/Fe^{2+})

In the previous chapter, a simple relation has been proposed (Equation (4.5)) for the estimation of the three dimensional roughness factor, γ_{3D}, of the IrO$_2$ coating.

In this chapter, the voltammetric behavior of Ti/IrO$_2$ electrodes of different IrO$_2$ loading has been investigated using the Fe^{3+}/Fe^{2+} redox couple as a fast probe reaction in order to get a first insight into the effectiveness factor of these electrodes.

Problems involved due to background current (voltammetric charge) and uncompensated electrolyte resistance between the working and reference electrode are presented. Furthermore, the sensibility on the uncompensated electrolyte resistance, R_u, of the standard rate constant, k^0, of the investigated redox couple has been evaluated.

5.1   Introduction

The activity of electrocatalysts such as DSA$^®$ electrodes is attributed to both intrinsic effects (electronic contribution) and surface area effects (geometric contribution). In fact, DSA$^®$ electrodes are 3D devices and in principle have a high surface area. In order to have

a better understanding on their catalytic activity, the contribution of each effect should be evaluated.

The geometric contribution can be evaluated from the three dimensional (3D) roughness factor, γ_{3D}, which is defined as the wetted surface area, A_w, per geometric (projected) area, A_g, of the coating (Equation (3.1)):

$$\gamma_{3D} = \frac{A_w}{A_g} \tag{3.1}$$

As it has been shown in the previous chapter, the voltammetric charge can be used in order to estimate the 3D roughness factor, γ_{3D}, of the Ti/IrO₂ electrodes, using the specific surface area of about 100 cm²/mg IrO₂ (see Equation (4.5)).

In this chapter, the Fe^{3+}/Fe^{2+} redox couple has been used as a probe in order to evaluate the influence of the IrO₂ loading on the fraction of electrode surface which effectively participates in the electrochemical reaction (effectiveness factor, E_f). This redox couple is generally considered as an outer-sphere redox couple, ideal for testing new electrode formulations. The kinetics of charge transfer of this reaction has been measured using numerous metallic electrodes (Pt, Au and Pd) and electrolytes, in which the results have been summarized in several reviews [1-3]. Most measurements were carried out with platinum electrodes in HClO₄ and the apparent standard rate constant was found to be between 10^{-2} and 10^{-3} cm/s [4]. However, it has been found that the presence of traces (few ppm) of chloride ions in the electrolyte can increase by several orders of magnitude the apparent rate constant. This increase has been attributed to the "ligand-bridging" mechanism [4]. All these investigations with the Fe^{3+}/Fe^{2+} redox couple have been conducted on polished flat metallic electrodes, however, there is only limited information for the electrochemical behavior of this couple in rough and/or porous electrodes like Ti/IrO₂.

The Fe^{3+}/Fe^{2+} redox couple in 1M HCl has been investigated by linear sweep voltammetry (LSV) and cyclic voltammetry (CV) on Ti/IrO₂ electrodes with different IrO₂ loading. Hydrochloric acid (HCl) has been chosen as supporting electrolyte in order to avoid experimental difficulties related to ill-defined traces of chloride in the supporting electrolyte. In the first step of measurements, the influence of electrode capacitance on the voltammetric response of the investigated system has been evaluated.

Then, the standard rate constant of the Fe^{3+}/Fe^{2+} redox couple, the exchange current density, and the diffusion coefficient of both Fe^{3+} and Fe^{2+} have been estimated from the CV measurements and related to IrO_2 loading.

5.2 Experimental

Four electrodes with different loading ($E_{0.11}$, $E_{0.28}$, $E_{1.81}$ and $E_{4.07}$) have been prepared as described in section 4.2a. The electrochemical measurements were carried out in a three-electrode cell using a computer controlled potentiostat (model Autolab® PGSTAT 30) as described in section 4.2c. Polarization measurements at different scan rates have been performed in 1M HCl solution and 50 mM Fe^{3+}/Fe^{2+} + 1M HCl using ultrapure (Millipore®) water. All potentials are expressed with respect to the mercurous sulfate electrode (MSE) used as a reference electrode. This electrode has been positioned at a distance of about 1 mm from the working electrode. The current densities have been reported relative to the geometric (projected) area.

5.3 Results and discussion

5.3.1 Effect of electrode capacitance on the voltammetric response of the Fe^{3+}/Fe^{2+} redox couple

Preliminary CV measurements have shown that the background current due to electrode capacitance of the IrO_2 coating can strongly influence the voltammetric response of the Fe^{3+}/Fe^{2+} redox system. Furthermore, it has been found that this interference due to the background current increases with the IrO_2 loading and potential scan rate.

Figures 5.1a and b show cyclic voltammograms of the Ti/IrO_2 electrode ($E_{4.07}$) obtained in 1M HCl supporting electrolyte and in 50 mM Fe^{3+}/Fe^{2+} + 1M HCl, respectively.
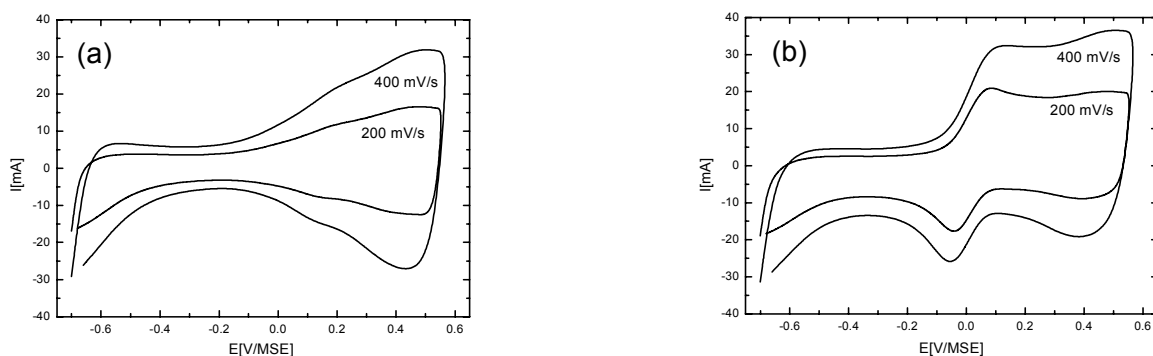
Figure 5.1: Cyclic voltammograms of the Ti/IrO$_2$ electrode ($E_{4.07}$) obtained in: (a) 1M HCl supporting electrolyte and (b) 50 mM Fe^{3+}/Fe^{2+} + 1M HCl. T=25°C.

Figure 5.1a shows that the background current under the investigated conditions corresponds to about 80% of the total current (Figure 5.1b) obtained in the presence of the Fe^{3+}/Fe^2 redox couple.

The correction of the obtained CVs of the redox couple, made by subtraction of the background current, depends strongly on the IrO$_2$ loading. In fact, if the correction can be achieved without any apparent difficulty at low loading (see Figures 5.2a and b), some anomalies (distortion) are observed at high IrO$_2$ loading (see Figures 5.2c and d).
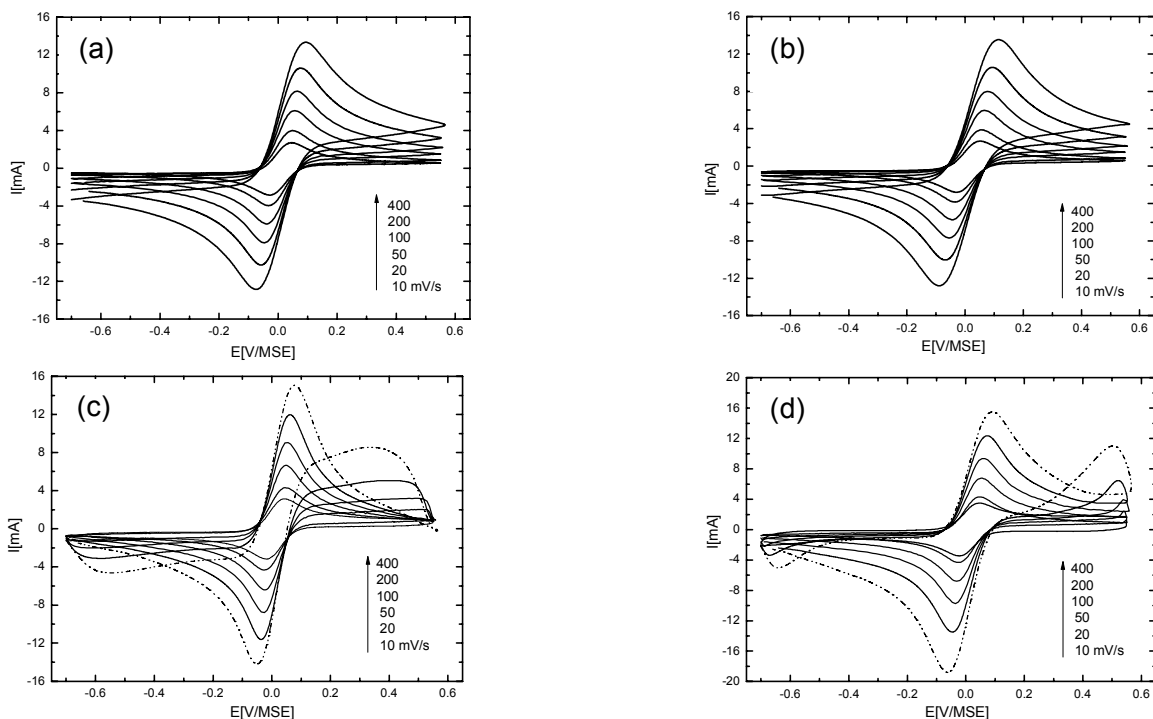
Figure 5.2: Background current corrected CVs in 50 mM Fe^{3+}/Fe^{2+} + 1M HCl at low loading: (a) $E_{0.11}$ and (b) $E_{0.28}$, and high loading: (c) $E_{1.81}$ and (d) $E_{4.07}$. T= 25°C.

76

Indeed, Figures 5.2c and d give an indication that the presence of Fe^{3+}/Fe^{2+} redox couple in the electrolyte can influence the charging/discharging process of the IrO_2 electrode. In fact, the Fe^{3+}/Fe^{2+} redox couple can participate in the charging/discharging of IrO_2 according to the reaction (5.1), and/or can influence the double layer capacitance.

$$IrO_x(OH)_y + \delta H^+ + \delta Fe^{2+} \rightleftharpoons IrO_{x-\delta}(OH)_{y+\delta} + \delta Fe^{3+} \qquad (5.1)$$

5.3.2 Electrochemical rate constant of the Fe^{3+}/Fe^{2+} redox couple obtained by CV

The determination of the electrochemical rate constant, k^0, for the redox couple Fe^{3+}/Fe^{2+} using the CVs of Figure 5.2, presents an intrinsic problem. In fact, the correction of the voltammetric measurements for the IR_u drop in the electrolyte (between the working and the reference electrode) is uncertain due to the difficulty of the estimation of the uncompensated resistance, R_u. As a matter of fact, the estimated resistance of 3Ω, obtained for the O_2 evolution reaction (see chapter 7, section 7.3.1a), involves bubble formation which contributes to the total resistance. In the case of Fe^{3+}/Fe^{2+}, a lower resistance is expected.

In order to evaluate the effect of R_u on k^0, the CV curves have been corrected using different values in the domain $0 \le R_u \le 3\Omega$.

The k^0 values have been estimated from the ΔE_p of the corrected CVs using different values of R_u and considering $D_{Fe^{2+}} = D_{Fe^{3+}}$, via the relation (5.2). The corresponding ψ values have been obtained from Table 5.1 and plotted as a function of $(1/\upsilon)^{1/2}$. From the slope, the standard rate constant, k^0, of the redox couple Fe^{3+}/Fe^{2+} has been calculated.

$$\psi = \frac{k^o}{\sqrt{\pi \cdot D \cdot f \cdot \upsilon}} \qquad (5.2)$$

where:

ψ : Related to ΔE_p and is given in Table 5.1,

ΔE_p : Potential difference between the anodic and cathodic peak potentials (E_{pa} and

E_{pc}), respectively,

k^0 : Standard rate constant [cm/s],

D : Diffusion coefficient of $D_{Fe^{2+}} = D_{Fe^{3+}}$ [cm²/s],

$$f = \frac{F}{RT} = 38.92 \text{ [1/V] at 25°C,}$$

υ : Scan rate [V/s].

Table 5.1: Variation of ΔE_p with ψ at 25°C [5].

ψ	20	7	6	5	4	3	2	1	0.75	0.50	0.35	0.25	0.10
ΔE_p [mV]	61	63	64	65	66	68	72	84	92	105	121	141	212

Furthermore, the exchange current density, j_0, of the redox couple Fe³⁺/Fe²⁺ has been

calculated using the relation (5.3) (see Table 5.2):

$$j_0 = Fk^0 C \tag{5.3}$$

where: F, k^0, C, have their usual meaning.

Table 5.2: Standard rate constant, k^0, and the exchange current density, j_0, for the redox couple Fe^{3+}/Fe^{2+}, where k^0 is obtained using Equation (5.2). Electrode: $E_{0.11}$. T=25°C.

R_u [Ω]	k^0 [cm/s]	j_0 [mA/cm^2]
0	3.7×10^{-3}	18
0.5	4.7×10^{-3}	23
1	6.6×10^{-3}	32
2	2.2×10^{-2}	105
3	7.2×10^{-2}	350

As seen from Table 5.2, both k^0 and j_0 depend strongly on the value of the uncompensated resistance, they increase with increasing R_u. The obtained values for both k^0 (3.7×10^{-3}-7.2×10^{-2} cm/s) and j_0 (18-350 mA/cm^2) indicate that the investigated redox couple is a fast reaction. In addition, these values are close to those reported by others [4].

5.3.3 Linear sweep voltammetry (LSV) for different IrO$_2$ loading

Figures 5.3a-d show uncorrected IR_u drop LSV measurements using four different loadings and different scan rates.
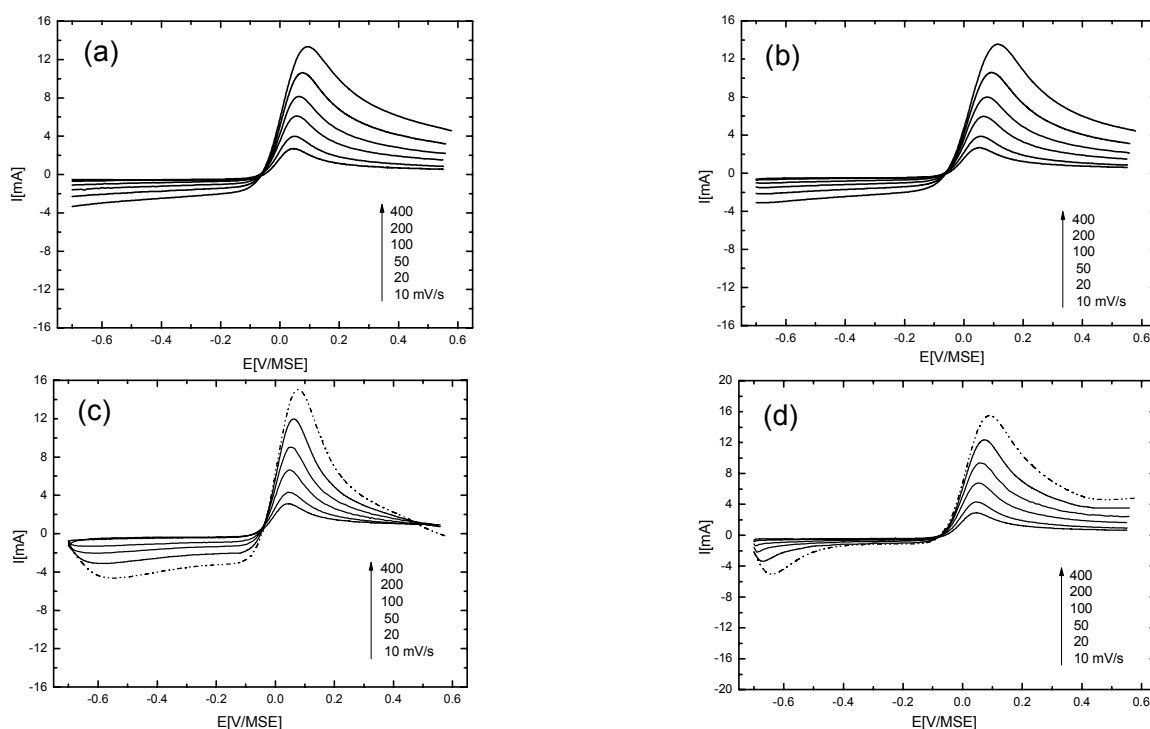
Figure 5.3: Uncorrected IR_u drop LSV measurements in 50 mM Fe^{3+}/Fe^{2+} + 1M HCl using four different loadings: (a) $E_{0.11}$, (b) $E_{0.28}$, (c) $E_{1.81}$ and (d) $E_{4.07}$, and different scan rates: 10, 20, 50, 100, 200 and 400mV/s. T= 25°C.

Figure 5.4 shows the plot of anodic peak current, I_{pa}, as a function of the square root of scan rate, $\upsilon^{1/2}$, obtained for different electrodes loadings.
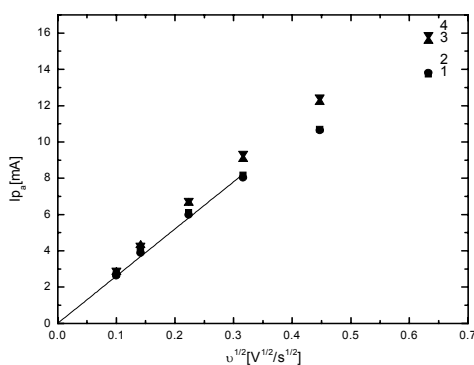
Figure 5.4: Anodic peak current, I_{pa}, from measurements of Figure 5.3, as a function of the square root of scan rate, $\upsilon^{1/2}$, obtained for the different electrodes loadings: 1: $E_{0.11}$, 2: $E_{0.28}$, 3: $E_{1.81}$ and 4: $E_{4.07}$.

The fact that the I_{pa}-$\upsilon^{1/2}$ curves are quasi-independent of loading (especially at low san rates) indicates that under the investigated conditions only the geometric surface area is involved in the LSV measurements. Note that this conclusion has already been suggested by the similarity of the cyclic voltammograms obtained with different loadings (see Figure 5.2). Furthermore, the diffusion coefficient of Fe^{2+} ($D_{Fe^{2+}}$) obtained from the slope of the I_{pa}-$\upsilon^{1/2}$ curve using equation (5.4) is $D_{Fe^{2+}}$ = 6x10^{-6} cm^2/s. It is very close to the value reported for Pt polished electrodes in aqueous medium [6], ($D_{Fe^{2+}}$ = 5.4x10^{-6} cm^2/s).

$$I_{pa} = (2.69x10^5)n^{3/2}A \cdot D_{Fe^{2+}}^{1/2} \cdot C_{Fe^{2+}} \cdot \upsilon^{1/2} \tag{5.4}$$

where:

I_{pa} : Anodic peak current, [mA],

n : Number of exchanged electrons [-],

A : Geometric surface area [cm^2],

$C_{Fe^{2+}}$: Concentration of Fe^{2+} [mol/cm^3],

$D_{Fe^{2+}}$ Diffusion coefficient of Fe^{2+} [cm^2/s],

υ : Scan rate [V/s].

5.4   Conclusions

This chapter can conclude in:

• The cyclic voltammetric (CV) measurements of the Fe^{3+}/Fe^{2+} redox couple have shown that the background current due to electrode capacitance of the IrO_2 coating can strongly influence the voltammetric response of this redox couple at high IrO_2 loading and high potential scan rate. This indicates that the presence of Fe^{3+}/Fe^{2+} redox couple in the electrolyte can influence the charging/discharging process of the IrO_2 electrode, and/or can influence the double layer capacitance,

81

- One inherent problem in the determination of the electrochemical rate constant of the redox couple Fe^{3+}/Fe^{2+} is the correction of the voltammetric measurements from the IR_u drop of the electrolyte. Considering different values of uncompensated electrolyte resistance (0-3 Ω), the standard rate constant, k^0, for the Fe^{3+}/Fe^{2+} redox couple, varies between 3.7×10^{-3} and 7.2×10^{-2} cm/s. These values are close to the ones given in the literature [4] and indicate a fast reaction,

- Linear sweep voltammetry (LSV) measurements have shown that I_{pa} vs. $\upsilon^{1/2}$ plots are quasi-independent of loading (especially at low scan rates). Furthermore, the obtained $D_{Fe^{2+}}$ is close to the value reported for polished Pt. This means that under the investigated conditions, only the geometric surface area of the Ti/IrO₂ electrode is involved in the LSV measurements.

5.5   References

1.   N.Tanaka and R. Tamamushi, *Electrochim. Acta*, 1964, **9**, 963-989.

2.   R.Tamamushi, *Kinetic Parameters of Electrode Reactions of Metallic Compounds*, Butterworths, London, 1975.

3.   K.E. Heusler, *Encyclopedia of Electrochemistry of the Elements*, Edited by A.J. Bard, Vol. IX A, Marcel Dekker, New York, 1982, 229.

4.   Z. Nagy, *Modern Aspects of Electrochemistry*, Edited by R.E. White et al., Vol. 37, Kluwer Academic/Plenum Publishers, New York, 2004, 256.

5.   Allen J. Bard and Larry R. Faulkner, *Electrochemical Methods-Fundamentals and Applications*, John Wiley & Sons, 2nd. Edition, 2001, 243.

6.   A.M. Baticle, F. Perdu, and P. Vennereau, *Electrochim. Acta*, 1971, **16**, 901-912.

Chapter 6

Estimation of the effectiveness factor of Ti/IrO$_2$ electrodes for a fast reaction (Fe^{3+}/Fe^{2+}) using RDE

As seen in the previous chapter, voltammetric techniques are not well suited for the estimation of the effectiveness factor, E_f, due mainly to difficult estimation of the uncompensated electrolyte resistance, R_u.

In this chapter, the rotating disk electrode (RDE) technique with the Fe^{3+}/Fe^{2+} redox couple as a probe reaction has been used in order to evaluate the effectiveness factor, E_f, and to compare these values with the theoretical ones using different IrO$_2$ loadings.

For this purpose, steady-state polarization measurements using Ti/IrO$_2$ rotating disk electrodes in 0.5M Fe^{3+}/Fe^{2+} in 1M HCl have been carried out under well defined hydrodynamic conditions. The low-field approximation relation has been used for the estimation of the exchange current densities, j_0 (reported to 1cm^2 geometric area), of the Fe^{3+}/Fe^{2+} redox couple.

6.1   Introduction

The effectiveness factor, E_f, is well known in heterogeneous catalysis and it is presented by O. Levenspiel [1] as the measure of how much the reaction rate is lowered because of the resistance to catalyst pore diffusion. In other words, this author defines the effectiveness factor as the ratio of the actual reaction rate within the pore and the rate if not slowed by pore diffusion.

In 1976, F. Coeuret et al. [2] present the effectiveness factor, E_f, for the first time in electrochemistry for a 3D electrochemical reaction. These authors defined the effectiveness factor as the ratio of the measured electrolytic current and the current obtained with an electrode whose overpotential maintained constant. The application of this is in the electrolytic treatment of given diluted solutions for the recovery of metal ions using a 3D porous electrode. Later, Savinell et al. used the effectiveness factor, E_f, for the investigation of the DSA® electrodes [3].

In this chapter, the effectiveness factor, E_f, has been used for the characterization of DSA® electrodes. The Fe^{3+}/Fe^{2+} redox couple has been used as a probe. Conditions have been chosen in order to minimise the effect due to bulk diffusion (low overpotential, high concentration). Finally, the obtained effectiveness factor, E_f, has been compared with the predicted one from the developed analytical approach (see chapter 3, section 3.2) .

6.2   Estimation of the effectiveness factor of Ti/IrO₂ electrodes

The effectiveness factor will be calculated from the measurements of the exchange current density, j_0, of the Fe^{3+}/Fe^{2+} redox couple using the relation in Equation (6.1):

$$E_f = \frac{(j_0)_{3D}}{(j_0)_{2D}\gamma_{3D}}$$

(6.1)

where: $(j_0)_{3D}$ is the exchange current density (measured current reported to 1cm² projected area) for a three dimensional (3D) IrO₂ electrode with a given loading, $(j_0)_{2D}$ is the exchange current density measured with a polished (two dimensional, 2D electrode) and γ_{3D} is the 3D roughness factor (see section 4.3.4) of the IrO₂ electrode with the given loading. Note that, in principle, $(j_0)_{2D}$ can be measured with any polished electrode when using the Fe^{3+}/Fe^{2+} redox couple as a probe. This is because the charge transfer with this couple is an outer-sphere reaction. Therefore, the standard rate constant, k^0, is independent of the electrode material. In practice, it is proposed to measure $(j_0)_{2D}$ with a polished Pt electrode.

6.3   Experimental

In order to determine the exchange current density of the Ti/IrO$_2$ electrodes, the rotating disk electrode (RDE) technique was proposed.

6.3.1   Preparation of Ti/IrO$_2$ rotating disk electrodes

Titanium wire (ø= 4 mm) has been used as substrate for the deposition of the IrO$_2$ coatings. The procedure was the same as described in the previous chapter (section 4.2a) except that the coating solution was applied by brushing instead of depositing a given volume with a micropipette. The lateral insulation of the Ti/IrO$_2$ rotating disk electrodes was done by Teflon as in the case of commercial RDEs. The resulted IrO$_2$ loading has been estimated from the voltammetric charge (see section 4.3.3). Four Ti/IrO$_2$ rotating disk electrodes of different loadings ($E_{0.62}$, $E_{1.97}$, $E_{2.46}$, and $E_{4.92}$) were prepared this way.

6.3.2   Steady-state polarization measurements using RDEs

Steady-state polarization measurements (scan rate 0.1 mV/s) with the Fe^{3+}/Fe^{2+} redox couple (0.5 M Fe^{3+} + 0.5 M Fe^{2+} in 1M HCl) have been carried out at room temperature in a three electrode cell using either a Ti/IrO$_2$ or a commercial Pt rotating disk electrode ($\varnothing$=4 mm; exposed geometric surface area: 0.125 cm^2) as working electrode (WE), Pt wire (Goodfellow 99.99%) as a counter electrode (CE) and MSE (Hg/Hg$_2$SO$_4$/K$_2$SO$_4$sat. Radiometer REF621) as a reference electrode (RE). A computer controlled EcoChemie potentiostat (model Autolab$^\circledR$ PGSTAT 30) and a RDE equipment EG&G Parc model 616 were used at five rotation rates: 100, 500, 1000, 1500 and 2000 rpm. All potentials are expressed with respect to the mercurous sulfate electrode (MSE).

The steady-state polarization curves were corrected for the uncompensated potential drop estimated from the equation (6.2):

$$\Delta E = I \cdot R_u \tag{6.2}$$

where: ΔE is the potential drop [V] between WE and RE, I is the measured current [A] and R_u is the overall cell resistance [Ω]. R_u has been estimated with the relation in equation (6.3), according to [4]:

$$R_u = \frac{1}{4 \cdot \gamma_o \cdot r}$$
(6.3)

where: γ_o is the conductivity of the electrolyte [$\Omega^{-1}cm^{-1}$] and r is the disk radius [cm].

6.4   Results and discussion

6.4.1   Polarization curves

Figure 6.1 shows ohmic drop corrected, steady-state (0.1 mV/s) $I-E$ curves and $I/I_{lim}-E$ curves (the limiting currents, I_{lim}, being taken at ±0.3 V) obtained at different rotation rates (100, 500, 1000, 1500, and 2000 rpm) using four electrodes of different loading ($E_{0.62}$, $E_{1.97}$, $E_{2.46}$, and $E_{4.92}$). The anodic and cathodic limiting currents plotted as a function of the square root of rotation rate for the four investigated electrodes are shown in Figure 6.2.
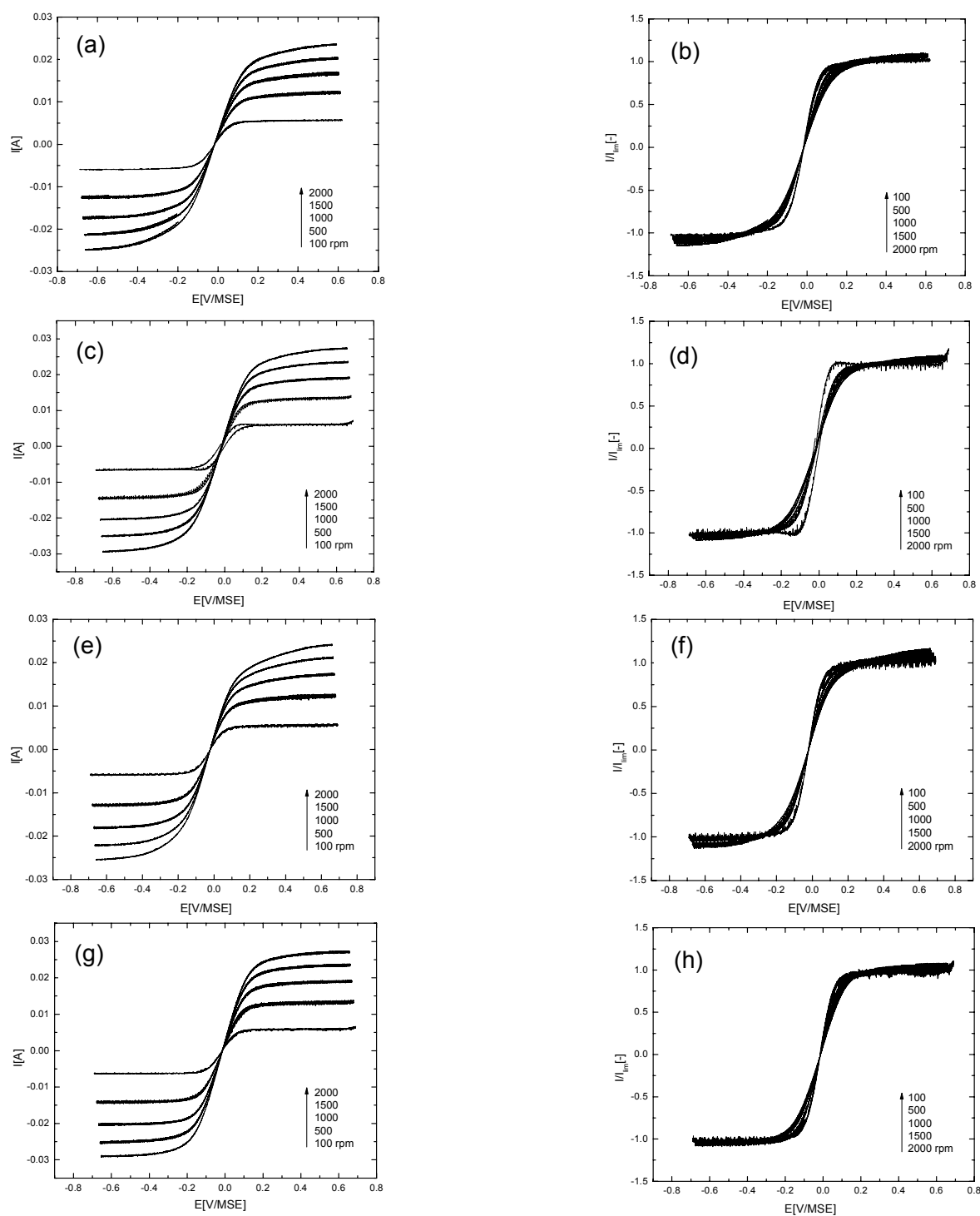
Figure 6.1: Ohmic drop corrected steady-state (0.1 mV/s) polarization curves of Ti/IrO$_2$ rotating disk electrodes of different loading: (a, b) E$_{0.62}$, (c, d) E$_{1.97}$, (e, f) E$_{2.46}$ and (g, h) E$_{4.92}$, recorded at different rotation rates: 100, 500, 1000, 1500, and 2000 rpm. Left (a, c, e, g): $I - E$ curves. Right (b, d, f, h): $I / I_{lim} - E$ curves (with $I_{lim} = I$ taken at ±0.3 V). Electrolyte: 0.5 M Fe^{3+} + 0.5 M Fe^{2+} in 1M HCl. T=25°C.
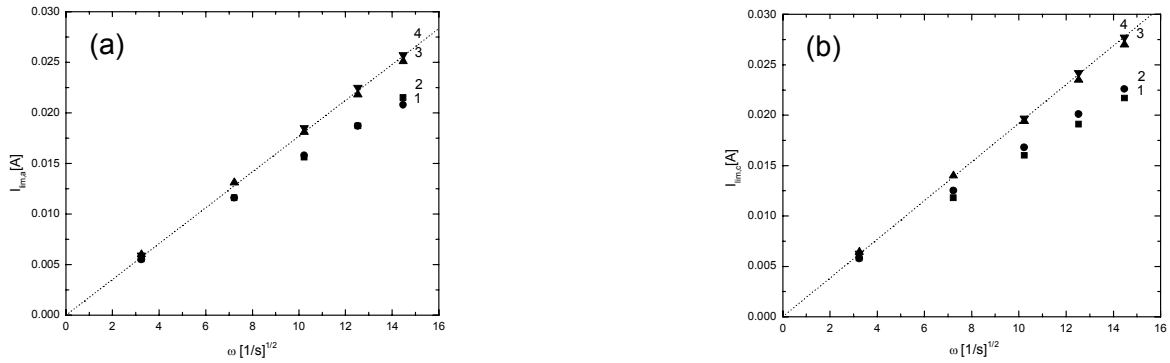
Figure 6.2: Plot of the (a) anodic and (b) cathodic limiting current, $I_{lim, a}$ and $I_{lim, c}$ (taken at E = +0.3 and -0.3 V, respectively), as a function of the square root of the rotation rate, $\omega^{1/2}$ for Ti/IrO₂ rotating disk electrodes of different loading: 1: $E_{0.62}$, 2: $E_{1.97}$, 3: $E_{2.46}$, and 4: $E_{4.92}$. Experimental conditions as in Figure 6.1.

From Figures 6.1 and 6.2, several interesting features can be underlined:

- The normalized ($I / I_{lim} - E$) polarization curves do depend on rotation rate (see Figure 6.1).
- At low loading and high rotation rates, even in the range of high overpotentials, the current continues to increase slightly with the applied potential without reaching a limiting value (see Figure 6.1).
- At low loading and high rotation rates, the $I_{lim} - \omega^{1/2}$ curves deviate from linearity (see Figure 6.2, points 1 and 2).

These anomalies observed at high rotation rates and low loading are certainly related to the surface roughness of the investigated electrodes. Electrodes of low loading have higher surface roughness factor, γ_{2D}, inherent to the preparation procedure of the used Ti substrate. In fact, Ti has a very high roughness factor after sandblasting. Increasing loading seems to decrease the surface roughness of the electrode. At high rotation rates, where the thickness of the diffusion layer goes down to a few micrometers (see below in Table 6.1), the behaviour of rough electrodes do not follow the theory of RDE, developed considering perfectly polished surfaces, because the diffusion layer thickness approaches the scale of surface roughness.

From the slope of the obtained straight lines in Figure 6.2 (considering the two high loadings), the diffusion coefficient of both Fe^{3+} and Fe^{2+} were calculated using the Levich equation (6.4):

$$I_{lim} = 0.62 \cdot nFAD^{2/3}\omega^{1/2}v^{-1/6}C \tag{6.4}$$

where: I_{lim} is the limiting current [A], n is the number of exchanged electrons, F is the Faraday constant [C/mol], A is the geometrical surface of the RDE [cm^2], D is the diffusion coefficient [cm^2/s] and C is the concentration [mol/cm^3] of the electroactive species (Fe^{3+} or Fe^{2+}), ω is the angular velocity [s^{-1}] and v is the kinematic viscosity [cm^2/s]. For the species Fe^{3+} and Fe^{2+}, respectively, diffusion coefficients of 3.6 ($\pm$0.1)$\times 10^{-6}$ and 3.3 ($\pm$0.1)$\times 10^{-6}$ cm^2/s were calculated, in a reasonable good agreement with the respective literature values (5.4$\times 10^{-6}$ and 4.4$\times 10^{-6}$ [5]) and with those (3.2$\times 10^{-6}$ and 2.8$\times 10^{-6}$ cm^2/s) obtained under the same experimental conditions using a polished platinum RDE.

The diffusion layer thickness, δ [μm], was estimated with equation (6.5) taking the average diffusion coefficient of Fe^{3+} and Fe^{2+} equal to 3.4 ($\pm$0.2)$\times 10^{-6}$ cm^2/s:

$$\delta = 1.61 \cdot D^{1/3}\omega^{-1/2}v^{1/6} \tag{6.5}$$

The estimated diffusion layer thickness at different rotation rates is given in Table 6.1.

Table 6.1: Thickness of the diffusion layer, δ, at different rotation rates calculated with Equation (6.5) taking the average diffusion coefficient of Fe^{3+} and Fe^{2+} equal to 3.4 ($\pm$0.2)$\times 10^{-6}$ cm^2/s.

Rotation rate [rpm]	100	500	1000	1500	2000
δ [μm]	35$\pm$3	16$\pm$2	11$\pm$1	9$\pm$1	8$\pm$1

Furthermore, from the anodic and cathodic limiting currents, $I_{lim,\,a}$ and $I_{lim,\,c}$ [A] (Figure 6.1), the exchange current density, j_0 [A/cm^2], of the Fe^{3+}/Fe^{2+} redox couple can be determined using equation (6.6):

$$\eta = I\frac{RT}{AF}\left(\frac{1}{j_0} - \frac{1}{j_{lim,\,c}} + \frac{1}{j_{lim,\,a}}\right)$$

(6.6)

where: η is the overpotential [V], I is the measured current [A], R is the molar gas constant [J/molK], T is the temperature [K], A is the geometrical surface of the RDE [cm²] and F is the Faraday constant [C/mol].

Table 6.2 shows j_0 values obtained for the four investigated Ti/IrO₂ electrodes using five different rotation rates. It is seen that j_0 slightly increases with the electrode loading and it is rather independent of the rotation speed, excepting the slowest rotation rate (100 rpm) where the experimental uncertainties are the highest. In the same table, the exchange current density, j_0, of the Fe^{3+}/Fe^{2+} redox couple measured on polished Pt electrode is also given.

Table 6.2: Exchange current density, j_0 (for 1cm² geometric area), of the Fe^{3+}/Fe^{2+} redox couple at different rotation rates for Ti/IrO₂ electrodes of different specific loading, m_{sp}, and for a polished Pt electrode, as calculated with Equation (6.6) from steady-state polarization data.

Rotation rate [rpm]	j_0 [mA/cm²]				
	m_{sp} [mg IrO₂/cm²]				Polished Pt
	0.62	1.97	2.46	4.92	
100	42	36	61	48	47
500	42	46	57	59	53
1000	44	46	56	57	52
1500	46	47	57	59	51
2000	47	47	55	62	51
Average*	45±2	47±1	56±1	59±2	52±1

*Average is taken with neglecting data obtained at the slowest (100 rpm) rotation rate.

6.4.2   Effectiveness factor for the 3D IrO₂ electrodes

As discussed in section 6.2, the effectiveness factor, E_f, of Ti/IrO$_2$ can be predicted from the analytical approach (see section 3.2) and calculated from experimental data (Equation (6.1)).

Prediction (according to section 3.2) of the effectiveness factor, E_f, using Equation (3.32) needs an estimation of all parameters involved in K_1 according to Equation (3.22):

$$E_f = \frac{\tanh(K_1)}{K_1} \tag{3.32}$$

and

$$K_1^2 = \frac{(1-\varepsilon)a_p L^2 \dfrac{1}{\gamma_0}\left(\dfrac{3-\varepsilon}{2\varepsilon}\right)}{\dfrac{RT}{j_0 F}} = \frac{R_\Omega}{R_{ct}} \tag{3.22}$$

For this purpose, the following simplifications have been considered when using the Fe^{3+}/Fe^{2+} redox couple as a probe reaction:

a) As the redox process with the Fe^{3+}/Fe^{2+} couple is an outer-sphere reaction (in principle, for these type of reactions the standard rate constant is independent of the electrode material), for the exchange current density the value measured with polished platinum RDE (j_0 = 52 mA/cm^2 ; see Table 6.2) has been taken. It gives with Equation (3.20), a charge-transfer resistance of R_{ct} = 0.49 Ωcm^2.

$$R_{ct} = \frac{RT}{j_0 F} \tag{3.20}$$

b) The ohmic resistance, R_Ω, relates the morphology of the Ti/IrO$_2$ electrodes and the conductivity of the electrolyte which relation is given by Equation (3.21), and from which the results are given in Table 6.3:

$$R_\Omega = (1-\varepsilon) a_p L^2 \frac{1}{\gamma_0} \left(\frac{3-\varepsilon}{2\varepsilon} \right) \qquad (3.21)$$

c) The electrolyte conductivity, γ_0, has been estimated from individual molar conductivity and concentration of each ion in solution (see Appendix). The obtained value is $\gamma_0 = 0.8$ $\Omega^{-1} \text{cm}^{-1}$.

d) Considering the coating as a dense cubic packing of uniform size spherical particles, the void volume fraction, ε, is estimated as 0.26.

e) The specific area of the IrO$_2$ particles, a_p, has been calculated using the relation given in Equation (3.3):

$$a_p = \frac{6}{d_p} \qquad (3.3)$$

with a particle diameter, d_p, estimated to 2 nm from the SEM analysis (see section 4.3.1a). The obtained specific area is 3×10^7 cm^{-1}.

f) The coating thickness, L [cm], has been estimated using the relation given in Equation (4.9):

$$L = \frac{m_{sp}}{1000 \cdot \rho \cdot (1-\varepsilon)} \qquad (4.9)$$

where: m_{sp} is the specific IrO$_2$ loading [mg/cm^2], ρ the bulk density of IrO$_2$ (11.7 g/cm^3) and ε the void volume fraction of the coating.

Table 6.3 shows the coating thickness, L, the ohmic resistance, R_Ω, the dimensionless number, K_1, and the model predicted effectiveness factor, E_f, for the Ti/IrO$_2$ electrodes used in the rotating disk electrode experiments.

Table 6.3: Prediction of the effectiveness factor. Characteristics of the IrO$_2$ electrodes of different specific loading, m_{sp}, used in the rotating disk electrode experiments: Coating thickness, L (Equation (4.9)), ohmic resistance, R_Ω (Equation (3.21)), dimensionless number, K_1 (Equation (3.22)), and predicted effectiveness factor, E_f (Equation (3.32)). For the calculation of K_1 and E_f, a charge transfer resistance of R_{ct}=0.49 Ωcm^2 was taken, obtained from analogous RDE experiments with a polished Pt electrode.

	m_{sp} [mg IrO$_2$/cm^2]			
	0.62	1.97	2.46	4.92
L [µm]	0.72	2.3	2.8	5.7
R_Ω [Ωcm^2]	0.75	7.6	12	47
K_1 [-]	1.2	3.9	4.9	20
E_f [-]	0.68	0.26	0.20	0.10

As seen, the analytical approach predicts rather high effectiveness factor which obviously increases with decreasing loading.

For comparison with the predicted data, the effectiveness factor, E_f, was also calculated from experimental data using Equation (6.1).

As experimental $(j_0)_{3D}$ data, the measured exchange current densities (average values calculated for rotation rates ≥500 rpm) were taken, as reported in Table 6.2, for the IrO$_2$ (3D) electrodes of different loading. Similarly, the exchange current density (average value calculated for rotation rates ≥500 rpm) measured with the polished Pt (2D) electrode (see Table 6.2) was identified as $(j_0)_{2D}$. The 3D roughness factor, γ_{3D}, of the IrO$_2$ electrodes, was calculated with Equation (4.5):

93

$$\gamma_{3D} = a_{sp} \cdot m_{sp} \tag{4.5}$$

where: a_{sp} is the specific surface area (=101.5 cm^2/mg IrO$_2$) of the coating (see section 4.3.3) and m_{sp} is the specific loading [mg IrO$_2$/cm^2]. The results are summarized in Table 6.4.

Table 6.4: Experimental determination of the effectiveness factor. Characteristics of the IrO$_2$ electrodes of different specific loading, m_{sp}, used in the rotating disk electrode experiments: Average exchange current density, $(j_0)_{3D}$ (see Table 6.2), 3D roughness factor, γ_{3D} (Equation (4.5)), and experimental effectiveness factor, E_f (Equation (6.1)). For the calculation of E_f, a 2D exchange current density of $(j_0)_{2D}$ = 52 mA/cm^2 was taken, measured with a polished Pt electrode.

	m_{sp} [mg IrO$_2$/cm^2]			
	0.62	1.97	2.46	4.92
$(j_0)_{3D}$ [mA/cm^2]*	45	47	56	59
γ_{3D} [-]	63	200	250	499
E_f [-]	0.014	0.005	0.004	0.002

* Reported for 1cm^2 geometric (projected) area.

As expected, also the experimentally obtained effectiveness factor increases with decreasing loading, but its value remains very low even at the lowest used loading. It means that in all cases only the 2D surface is effectively working.

For comparison, the predicted (according to section 3.2) and the experimental effectiveness factors are summarized in Table 6.5.

Table 6.5: Comparison of the predicted and experimental effectiveness factors for IrO_2 electrodes of different loading.

		m_{sp} [mg IrO_2/cm^2]			
		0.62	1.97	2.46	4.92
E_f [-]	Predicted	0.68	0.26	0.20	0.10
	Experimental	0.014	0.005	0.004	0.002

The comparison reveals a huge difference between the predicted and the experimental effectiveness factor. This difference is certainly related to the main assumption of our analytical approach that the concentration of the electroactive species (Fe^{3+} and Fe^{2+}) is invariant inside the coating. This is surely not the case. In fact, as the charge transfer with this redox couple is very fast, a sharp decrease of Fe^{3+} and Fe^{2+} concentration within the pores is awaited during polarization.

6.5 Conclusions

This chapter concludes in:

- The Fe^{3+}/Fe^{2+} redox couple has been used as a probe reaction in order to evaluate the E_f of this redox couple and to compare these values with the theoretical ones using different IrO_2 loadings,
- Steady-state polarization measurements using RDE electrodes in 0.5M Fe^{3+}/Fe^{2+} in 1M HCl were done and corrected for the uncompensated potential drop,
- The exchange current densities, j_0 (reported to 1cm^2 geometric area), show to increase slightly with the electrode loading and it is rather independent of the rotation speed, except at the slowest one (100 rpm), where the experimental uncertainties are the highest,
- The analytical approach predicts rather high effectiveness factor, which obviously increases with decreasing loading. The huge difference between the predicted and experimental values of the effectiveness factor is certainly related to the kinetics of the redox couple (Fe^{3+}/Fe^{2+}), which is a very fast reaction,

- In summary, the reaction with the Fe^{3+}/Fe^{2+} redox couple takes place almost exclusively at the 2D surface shown by the very low experimental E_f values, and the exclusion of the 3D surface is due to a sharp concentration gradient.

6.6 References

1. O. Levenspiel, *Chemical Reaction Engineering*, Wiley Eastern Limited, 2nd. Edition, New Delhi, 1972, 473.

2. F. Coeuret, D. Hutin, A. Gaunand, *J. Appl. Electrochem.*, 1976, **6**, 417-423.

3. R. F. Savinell, R. L. Zeller, and J. A. Adams, *J. Electrochem. Soc.*, 1990, **137**, 489-494.

4. Allen J. Bard and Larry R. Faulkner, *Electrochemical Methods-Fundamentals and Applications*, John Wiley & Sons, 2nd. Edition, 2001, 345.

5. A. M. Baticle, F. Perdu, and P. Vennereau, *Electrochim. Acta*, 1971, **16**, 901-912.

Appendix

Summary of ionic conductivities of the solution 0.5M $FeCl_3$ + 0.5M $FeCl_2$ in 1M HCl.

	Fraction	Ions	Molar conductivity [$cm^2 \cdot S \cdot mol^{-1}$]	Ionic concentration λ [mol cm^{-3}]	Electrolyte conductivity γ [S cm^{-1}]
HCl 1M	1	H^+	349.65	0.001	0.35
	1	Cl^-	76.31	0.001	0.08
$FeCl_2$ 0.5M	0.5	Fe^{2+}	54	0.0005	0.05
	1	Cl^-	76.31	0.001	0.08
$FeCl_3$ 0.5M	0.33	Fe^{3+}	68	0.0005	0.10
	1	Cl^-	76.31	0.0015	0.11
Total					**0.77**

Chapter 7

Estimation of the effectiveness factor of Ti/IrO$_2$ electrodes for slow reactions (oxygen and chlorine evolution)

In the previous chapter, where the Fe^{3+}/Fe^{2+} redox couple was used as a probe reaction, it has been shown that there is a huge difference between the theoretical and the experimental effectiveness factor, E_f, determined for different IrO$_2$ loadings. This difference between the experimental and the theoretical values has been attributed to the main assumption that the analytical approach considers the concentration of both Fe^{3+} and Fe^{2+} constant within the coating. This assumption seems not to be the case as this redox couple involves fast reactions.

In this chapter, the O$_2$ evolution reaction has been considered for the estimation of the effectiveness factor, E_f, using different IrO$_2$ loadings. The assumption made by the analytical approach is valid in this system, as water present in excess within the coating is involved in the reaction.

Furthermore, the redox couple, Cl$_2$/Cl$^-$ has been investigated using different IrO$_2$ loadings and the effectiveness factor, E_f, has been determined in order to compare it with the theoretical one.

7.1   Introduction

In chapter 6, we have shown that in the Fe^{3+}/Fe^{2+} system, which is a relatively fast outer-sphere reaction, only the geometric (projected) surface participates effectively in the electrochemical reaction. In this chapter, both the oxygen evolution and chlorine reactions,

which are known to be much more slower reactions than the Fe^{3+}/Fe^{2+} system, have been used in order to evaluate the influence of the electrode kinetics on the effectiveness factor, E_f, (i.e. the effective electrode area which indeed participates in the electrochemical reaction). The experimentally obtained E_f values will be compared with those predicted by the analytical approach (Equation (3.32)) developed in chapter 3, section 3.2.

$$E_f = \frac{\tanh(K_1)}{K_1} \tag{3.32}$$

where: K_1 is a dimensionless number (see chapter 3, section 3.2).

7.2   Experimental

a) Electrode preparation and electrochemical measurements

Four electrodes with different loading ($E_{0.11}$, $E_{0.28}$, $E_{1.81}$, and $E_{4.07}$) have been prepared as described in section 4.2a. The electrochemical measurements were carried out in a single-compartment cell made of teflon using a three-electrode cell as described in section 4.2c. Polarization measurements (5mV/s) have been performed in 1M $HClO_4$ solution (oxygen evolution) and 1M HCl (chlorine evolution) using ultrapure (Millipore®) water. All potentials are expressed with respect to the mercurous sulfate electrode (MSE) used as a reference electrode. The current density has been reported relative to the geometric area.

The specific IrO_2 loading, m_{sp}, the roughness factor, γ_{3D}, calculated with Equation (4.5) and the estimated coating thickness, L, calculated with Equation (4.9) for the four IrO_2 electrodes are shown in Table 7.1:

$$L = \frac{m_{sp}}{1000 \cdot \rho \cdot (1-\varepsilon)} \tag{4.9}$$

where: m_{sp} is the specific IrO$_2$ loading [mg IrO$_2$/cm^2], ρ is the bulk density of IrO$_2$ (11.7g/cm^3) and ε is the volume fraction of the pores in the coating [-].

and

$$\gamma_{3D} = a_{sp} \cdot m_{sp} \tag{4.5}$$

where: a_{sp} is the specific surface area (=101.5 cm^2/mg IrO$_2$) of the coating (see section 4.3.3) and m_{sp} is defined before.

Table 7.1: Characteristics of the Ti/IrO$_2$ electrodes used for the gas evolution reactions: Specific IrO$_2$ loading, m_{sp}, roughness factor, γ_{3D}, and the estimated coating thickness, L.

m_{sp} [mg IrO$_2$/cm^2]	0.11	0.28	1.81	4.07
γ_{3D} [-]	11.2	28.4	184	413
L [µm]	0.13	0.32	2.1	4.7

b) Ohmic (IR_u) drop correction

It was proposed to investigate the reactions of oxygen and chlorine evolution in terms of semi-logarithmically plotted current-potential curve at high overpotential known as Tafel plot. However, the use of the Tafel approach for gas-evolving reactions is difficult due to the formation of gas bubbles at the electrode surface. The nucleation of bubbles depends on the saturation degree of the gas in the liquid, which is controlled by the mass-transfer and the current density. In general, during gas evolution, the electrode surface is covered with a steady layer of gas bubbles, depending on the current density and the nature of the anode surface. The state of the electrode surface is important because the bubbles are formed at active nucleation sites, i.e. on surface irregularities. Thus, taking this into account, the nucleation of bubbles on a thermally prepared IrO$_2$ electrode might be important due to its high, both 2D and 3D roughness. Bubble formation not only reduces the active surface area of the electrode but also influences the ohmic resistance of the electrolyte. Both of these factors may cause distortion of the polarization curves. Thus, in

order to obtain meaningful data, it is necessary to perform an appropriate correction of the polarization curves before proceeding to Tafel plot analysis.

The ohmic drop correction was made using the method of D. M. Shub [1] which allows the estimation of the total uncompensated resistance of the studied system. In this method, it is assumed that the experimentally observed overpotential, η [V], at any current is given by equation (7.1):

$$\eta = a + b \ln I + IR_u \qquad (7.1)$$

where: a is the Tafel constant [V] , b is the Tafel slope [V/dec], I is the current [A], and R_u is the total uncompensated resistance [Ω] between the working and the reference electrode of the system assumed to be constant and independent of current. Differentiating Equation (7.1) with respect to the current density gives equation (7.2) from which b and R_u can be obtained by plotting $\dfrac{d\eta}{dI}$ vs. $1/I$:

$$\frac{d\eta}{dI} = \frac{b}{I} + R_u \qquad (7.2)$$

Knowledge of R_u allows correction of the experimental overpotential by subtraction of the ohmic drop, IR_u , according to equation (7.3):

$$\eta_{corr} = \eta - IR_u \qquad (7.3)$$

In the numerical calculation, the derivative $\dfrac{d\eta}{dI}$ was replaced by $\Delta\eta / \Delta I$ calculated from each pair of two consecutive experimental points.

7.3   Results and discussion

Both oxygen and chlorine evolution being an inner-sphere reaction (thus dependent on the electrode material), on one hand, and no polished IrO_2 electrode being available, on the other hand, the exchange current density for a true 2D electrode, $(j_0)_{2D}$, is not known. Hence, the relation given in section 6.2 for the calculation of the experimental effectiveness factor, E_f, given by Equation (6.1):

$$E_f = \frac{(j_0)_{3D}}{(j_0)_{2D}\,\gamma_{3D}} \qquad\qquad (6.1)$$

is not applicable in the given systems. Instead, it is proposed to calculate the experimental effectiveness factor with respect to the Ti/IrO_2 electrode of lowest loading as a reference (relative effectiveness factor, $E_f^{rel.}$), by using the relation given in equation (7.4):

$$E_f^{rel.} = \frac{(j_0)_{3D}\,/\,m_{sp}}{(j_0)_{3D}^{ref}\,/\,m_{sp}^{ref}} \qquad\qquad (7.4)$$

where: $(j_0)_{3D}^{ref}$ and m_{sp}^{ref} are, respectively, the exchange current density and the specific loading of the reference 3D electrode (in the present case, the electrode ($E_{0.11}$) with 0.11 mg IrO_2/cm^2 specific loading).

7.3.1   Oxygen evolution reaction

a) Polarization curves: Ohmic (IR_u) drop correction

Figure 7.1 shows a typical polarization curve obtained in 1M $HClO_4$ on the Ti/IrO_2 electrode ($E_{0.11}$) before (curve 1) and after (curve 2) IR_u drop correction using the

uncompensated resistance, R_u (=3.2 Ω), of the cell determined from the intersection of the plot of $\Delta \eta / \Delta I$ vs. $1 / I$ using Equation (7.2) (see Figure 7.2).
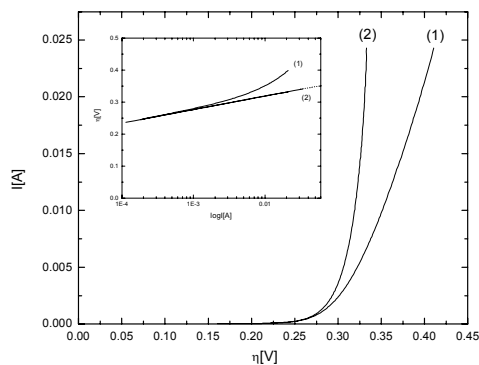
Figure 7.1: Steady-state (5 mV/s) polarization curves obtained in 1M HClO₄ on the Ti/IrO₂ electrode ($E_{0.11}$) before (curve 1) and after (curve 2) ohmic drop correction. Inset: Tafel lines before (curve 1) and after (curve 2) ohmic drop correction. T= 25°C.
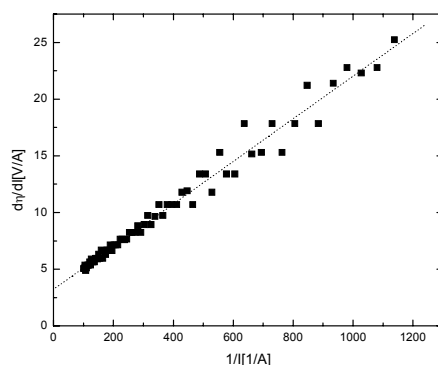
Figure 7.2: Determination of the uncompensated resistance from the intersection of the plot of $\Delta \eta / \Delta I$ vs. $1 / I$ using the data of Figure 7.1.

From both the experimental and the corrected polarization curves, the Tafel lines were plotted (inset of Figure 7.1). It can be seen that in the high overpotential region the uncorrected curve (curve 1) deviates strongly from linearity. However, the corrected polarization curve (curve 2) is linear to give a Tafel slope of 43 mV/decade.

In acidic medium, the following mechanism for the O₂ evolution on oxide electrodes has been proposed by De Faria et al. [2, 3]:

$$S + H_2O \rightarrow S - OH_{ads} + H^+ + e^- \tag{7.5}$$

$$S - OH_{ads} \rightarrow S - O_{ads} + H^+ + e^- \tag{7.6}$$

$$2S - O_{ads} \rightarrow 2S + O_2 \tag{7.7}$$

In the first step (reaction (7.5)) water is discharged forming adsorbed hydroxyl radicals. These hydroxyl radicals are further discharged forming a higher oxide (reaction (7.6)) which is finally decomposed to oxygen liberating the active site S (reaction (7.7)).

Depending on the rate-determining step (rds) of this process, different Tafel slopes can be obtained: 120 mV/dec if step 1 is the rds, 40 mV/dec if step 2 is the rds, and 15 mV/dec if step 3 is the rds.

The obtained experimental Tafel slope (43 mV/decade) indicates that the formation of the higher oxide is certainly the rate-determining step of the process. In fact, using differential mass spectroscopy (DEMS) measurements with $^{18}O_2$, it has been demonstrated that the oxide participated effectively in the oxygen evolution reaction [4].

Furthermore, the exchange current density, j_0 [mA/cm^2] and the Tafel slope, b, of the oxidation of the redox couple O_2/H_2O can be determined using Equation (7.1). Table 7.2 shows the j_0 and b values obtained for the four investigated Ti/IrO$_2$ electrodes.

Table 7.2: Exchange current density, j_0, Tafel slope, b, (defined in Equation (7.1)), and the roughness factor, γ_{3D}, (defined in Equation (4.5)) of the O_2/H_2O redox couple for four Ti/IrO$_2$ electrodes of different specific loading, m_{sp}.

m_{sp} [mg/cm^2]	γ_{3D} [-]	j_0 [mA/cm^2]*	b (Tafel slope)[V/dec]
0.11	11.2	1.34x10^{-6}	0.043
0.28	28.4	2.75 x10^{-6}	0.043
1.81	184	2.35 x10^{-5}	0.043
4.07	413	6.02 x10^{-5}	0.043

* Reported for 1cm^2 geometric (projected) area.

b) Relative effectiveness factor for the Ti/IrO₂ electrodes

The effectiveness factor, E_f, of the Ti/IrO$_2$ electrodes (as discussed in section 6.2), can be predicted from the analytical approach (see Equation (3.32)). For comparison with the experimental relative effectiveness factor, calculated with Equation (7.4), the predicted values were also referred to that of the lowest loading to give $E_f^{rel.}$.

Table 7.3: Comparison of the relative predicted and experimental effectiveness factors, $E_f^{rel.}$, for various IrO$_2$ loadings.

Prediction					Experimental	
m_{sp} [mg/cm^2]	L [cm]	R_Ω [Ωcm^2]	K_1 [-]	$E_f^{rel.}$ [-]	$j_{0(3D)}$ [mA/cm^2]*	$E_f^{rel.}$ [-]
0.11	1.3 x10^{-5}	0.044	0.00005	1.00**	1.34 x10^{-6}	1.00**
0.28	3.2 x10^{-5}	0.30	0.0001	1.00	2.75 x10^{-6}	0.81
1.81	2.1 x10^{-4}	12	0.0008	1.00	2.35 x10^{-5}	1.07
4.07	4.7 x10^{-4}	60	0.0018	1.00	6.02 x10^{-5}	1.21

* Reported for 1cm^2 geometric (projected) area

** Taken as a reference.

Table 7.3 shows that the relative effectiveness factor, $E_f^{rel.}$, for both the experimental and the theoretical values is close to the unity (fluctuating between 0.8 and 1.2) indicating that almost all the active surface of the coating participates in this reaction. This is mainly due to two reasons:

- The O$_2$/H$_2$O reaction is slow (low j_0 value),

- There is no concentration gradient within the coating as water is the reactive species present in excess inside the coating.

7.3.2 Chlorine evolution reaction

a) Polarization curves: Determination of the exchange current density

Figure 7.3 shows a polarization curve typical for all Ti/IrO$_2$ electrode loadings obtained in 1M HCl before and after IR_u drop correction using the uncompensated resistance determined from the intersection of the plot of $\Delta\eta / \Delta I$ vs. $1/I$ using Equation (7.2).
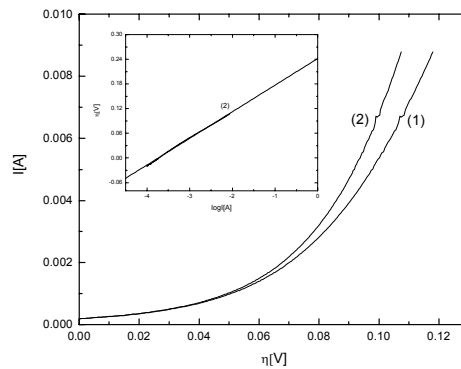
Figure 7.3. Steady-state (5 mV/s) polarization curves obtained in 1M HCl on the Ti/IrO$_2$ electrode ($E_{0.11}$) before (curve 1) and after (curve 2) ohmic drop correction. Inset : Tafel line after ohmic drop correction (curve 2).

From the corrected polarization curves, the Tafel lines were plotted (inset of Figure 7.3) and the exchange current density, j_0 (for 1cm^2 geometric area), of the redox couple Cl$_2$/Cl$^-$ has been determined using Equation (7.1) for the four investigated IrO$_2$ loadings.

Table 7.4: Exchange current density, j_0, and the roughness factor, γ_{3D}, of the Cl$_2$/Cl$^-$ redox couple for four Ti/IrO$_2$ electrodes of different specific loading, m_{sp}.

m_{sp} [mg/cm^2]	γ_{3D} [-]	j_0 [mA/cm^2]*
0.11	11.2	0.22
0.28	28.4	0.56
1.81	184	2.32
4.07	413	4.83

* Reported for 1cm^2 geometric (projected) area.

b) Relative effectiveness factor for the Ti/IrO₂ electrodes

The same approach as that given for the O_2 evolution, has been used for the estimation of the relative effectiveness factor, $E_f^{rel.}$, using Equation (7.4). In this relation, the lowest IrO_2 loading, $E_{0.11}$, has been used as a reference.

Table 7.5: Comparison of the relative predicted and experimental effectiveness factors, $E_f^{rel.}$, for various IrO_2 loadings.

Prediction					Experimental	
m_{sp} [mg/cm^2]	L [cm]	R_Ω [Ωcm^2]	K_1 [-]	$E_f^{rel.}$ [-]	$j_{0(3D)}$ [mA/cm^2]*	$E_f^{rel.}$ [-]
0.11	1.3E-05	0.044	0.019	1.00**	0.22	1.00**
0.28	3.2E-05	0.30	0.050	1.00	0.56	0.98
1.81	2.1E-04	12	0.32	0.97	2.32	0.64
4.07	4.7E-04	60	0.72	0.86	4.83	0.59

* Reported for 1cm^2 geometric (projected) area.

** Taken as a reference.

This table shows that both relative experimental and predicted effectiveness factors decrease with the IrO_2 loading. Furthermore, the experimental values are close to the predicted ones.

This is a predicted behaviour as the Cl_2/Cl^- redox couple has an intermediate kinetics between the O_2/H_2O and the Fe^{3+}/Fe^{2+} redox couples.

7.4   Conclusions

This chapter concludes in:

- The investigation of the kinetics of O_2 and Cl_2 evolution shows that the chlorine evolution is much faster than the O_2 evolution. In fact, the exchange current density of

- chlorine, $(j_0)_{Cl_2}$, equals 0.22 mA/cm^2 and for the O$_2$, $(j_0)_{O_2}$ equals 1.3x10^{-6} mA/cm^2, considering the E$_{0.11}$ electrode,

- The relative effectiveness factors, $E_f^{rel.}$, for the O$_2$ evolution are close to the unity (between 0.8 and 1.2) for all the IrO$_2$ loadings, however, for the Cl$_2$/Cl$^-$ redox couple, it decreases with the IrO$_2$ loading. This behavior is predicted according to the proposed analytical approach.

7.5   References

1.   D. M Shub, M. F. Reznik, V.V. Shalaginov, *Elektrokhimiya*, 1985, **21**, 937-941.

2.   L. A. De Faria, J. F. C. Boodts, and S. Trasatti, *J. Appl. Electrochem.*, 1996, **26**, 1195-1199.

3.   L. M. Da Silva, J. F. C. Boodts, and L.A. De Faria, *Electrochim. Acta*, 2001, **46**, 1369-1375.

4.   S. Fierro, T. Nagel, H. Baltruschat, Ch. Comninellis, *Electrochem. Comm.*, 2007, **9**, 1969-1974.

Chapter 8

Investigation of isopropanol oxidation on Ti/IrO$_2$ electrodes

In this chapter, the electrochemical oxidation of isopropanol was investigated on Ti/IrO$_2$ electrodes with different IrO$_2$ loading. The obtained results indicate that the oxidation of isopropanol leads to a decrease of the overpotential of water discharge with the increase of isopropanol concentration. A model has been proposed based on three main reactions: Electrochemical IrO$_2$ oxidation to IrO$_3$, chemical oxidation of isopropanol via IrO$_3$ and chemical decomposition of IrO$_3$ to IrO$_2$ (reactions (8.7)-(8.9)). Finally, the effectiveness factor, E_f, for both the electrochemical and chemical reactions (8.7) and (8.8) has been evaluated for different IrO$_2$ loadings.

8.1   Introduction

Thin film conductive coating deposited on an inert substrate has been widely investigated as anode material for chlorine and oxygen evolution [1] and oxidation of organic compounds [2-4].

Concerning organics oxidation, we have found in our laboratory that frequently electrochemical oxidation of some organics in aqueous medium occurs, without any loss in electrode activity, when it takes place at high potentials with concomitant evolution of O$_2$ [5, 6]. Furthermore, it has been found that the nature of the electrode material influences strongly both the selectivity and the efficiency of the process [7-9].

In order to interpret these observations a comprehensive model for anodic oxidation of organics in acidic medium, including competition with oxygen evolution has been proposed [7-9]. This model permits to distinguish between two limiting cases:

'active' and 'non-active' anode. Figure 8.1 illustrates the reaction scheme in acidic medium (i.e. $HClO_4$), where M designates an active site at the anode surface.
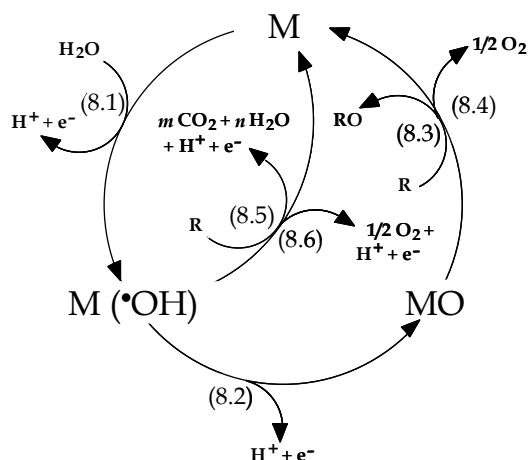
Figure 8.1. Scheme of the electrochemical oxidation of organic compounds on 'active' anodes (reactions (8.1), (8.2), (8.3), (8.4)) and on 'non-active' anodes (reactions (8.1), (8.5), (8.6)). (8.1) water discharge to hydroxyl radicals; (8.2) formation of the higher metal oxide; (8.3) partial (selective) oxidation of the organic compound, R, *via* the higher metal oxide; (8.4) oxygen evolution by chemical decomposition of the higher metal oxide; (8.5) combustion of the organic compound *via* hydroxyl radicals; (8.6) oxygen evolution by electrochemical oxidation of hydroxyl radicals.

In all cases, the initial step is the discharge of water molecules to form adsorbed hydroxyl radicals (reaction (8.1)):

$$M + H_2O \rightarrow M(^\bullet OH) + H^+ + e^- \tag{8.1}$$

The electrochemical and chemical reactivity of the adsorbed hydroxyl radicals depends strongly on the nature of electrode material used. Two extreme classes of electrodes can be defined: 'active' and 'non-active' electrodes:

a) At 'active' electrodes, there is a strong electrode (M) - hydroxyl radical ($^\bullet OH$) interaction. In this case, the adsorbed hydroxyl radicals may interact with the anode with possible transition of the oxygen from the hydroxyl radical to the anode surface, forming a higher oxide (reaction (8.2)). This may be the case when higher oxidation states on the surface electrode are available above the thermodynamic potential for oxygen evolution (1.23 V/RHE: 0.59V/MSE).

$$M(^\bullet OH) \rightarrow MO + H^+ + e^- \tag{8.2}$$

The surface redox couple MO/M can act as mediator in the oxidation of organics at 'active' electrodes (reaction (8.3)). This reaction is in competition with the side reaction of oxygen evolution due to the chemical decomposition of the higher oxide (reaction (8.4)).

$$MO + R \rightarrow M + RO \tag{8.3}$$

$$MO \rightarrow M + 1/2O_2 \tag{8.4}$$

The oxidation reaction *via* the surface redox couple MO/M (reaction (8.3)) may result in the partial (selective) oxidation of organics. This anodic oxidation process has been reported as redox catalysis.

b) At 'non-active' electrodes, there is a weak electrode (M) - hydroxyl radical ($^\bullet OH$) interaction. In this case, the oxidation of organics is mediated by hydroxyl radicals (reaction (8.5)), which may result in fully oxidized reaction products such as CO_2:

$$M(^\bullet OH) + R \rightarrow M + mCO_2 + nH_2O + H^+ + e^- \tag{8.5}$$
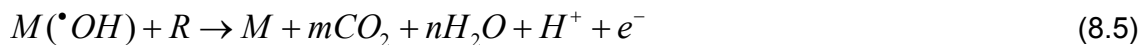
This reaction is in competition with the O_2 evolution (reaction (8.6)) side reaction (through formation of H_2O_2 as intermediate) to O_2 without any participation of the anode surface:

$$M(^\bullet OH) \rightarrow M + 1/2O_2 + H^+ + e^- \tag{8.6}$$

The distinction between 'active' and 'non-active' behavior and the underlying mechanistic explanation are supported by several experimental observations, including detection of reactive intermediates in the oxygen evolution reaction, such as hydroxyl radicals produced by discharge of water [10].

In this chapter, the kinetics of isopropanol (a model of organic compounds) oxidation on Ti/IrO$_2$ electrodes (a typical active electrode) with different loading have been investigated. Due to the complexity of the system only the experimental effectiveness factor, E_f, is presented.

8.2 Experimental

Four Ti/IrO$_2$ electrodes with different loading ($E_{0.11}$, $E_{0.28}$, $E_{1.81}$ and $E_{4.07}$) have been prepared as described in section 4.2a. The electrochemical measurements were carried out in a single-compartment cell made of Teflon using a three-electrode cell as described in section 4.2c. All tests were performed at four isopropanol concentrations: 0.1, 0.2, 0.4 and 0.5M in 1M HClO$_4$ supporting electrolyte, at 25°C.

8.3 Results and discussion

Figure 8.2 shows the influence of isopropanol (ISP) concentration in 1M HClO$_4$ on the voltammetric curves at 5mV/s, obtained using Ti/IrO$_2$ electrodes with different loading.
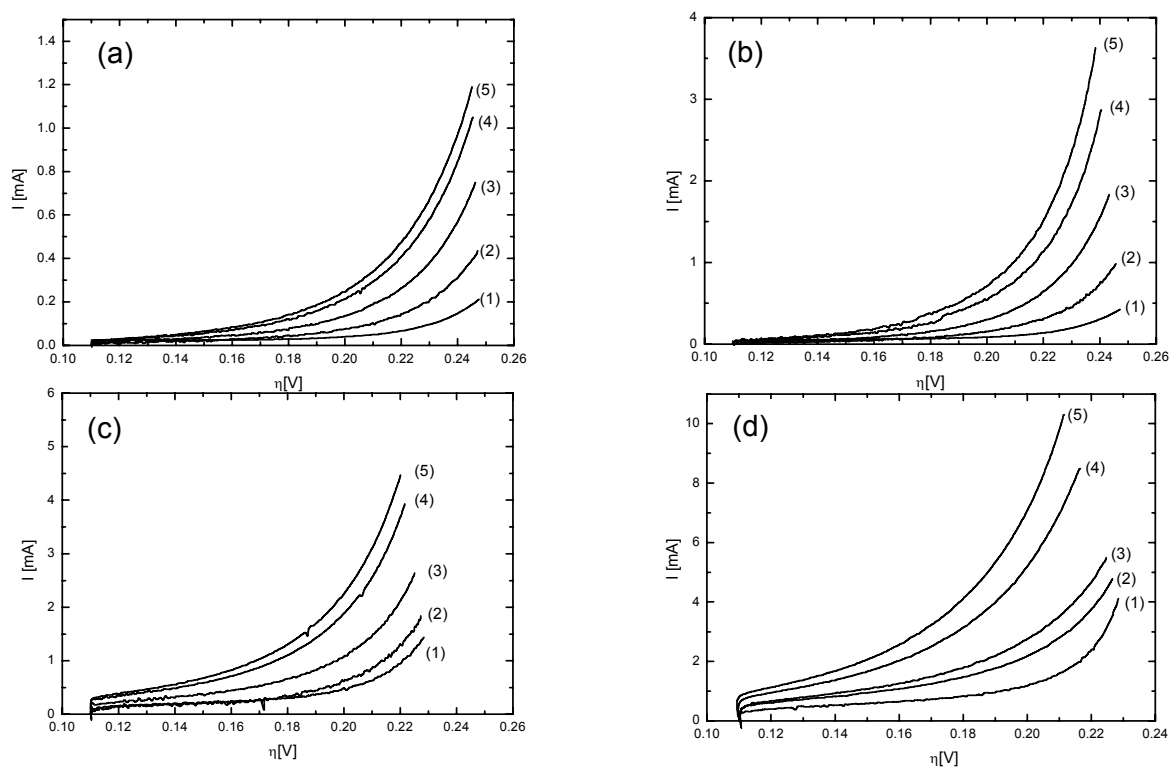
Figure 8.2: Steady-state polarization curves performed at 5mV/s using Ti/IrO$_2$ electrodes with different loading: (a) $E_{0.11}$, (b) $E_{0.28}$, (c) $E_{1.81}$, and (d) $E_{4.07}$ and for different concentration of (ISP) in 1M HClO$_4$ supporting electrolyte: (1) 0M, (2) 0.1M, (3) 0.2M, (4) 0.4M and (5) 0.5M. T= 25°C.

Figure 8.2 shows that the overpotential of the oxygen evolution decreases as the concentration of the organic (isopropanol) increases.

In order to determine from these voltammetric measurements the kinetic parameters of ISP oxidation on Ti/IrO$_2$ anodes, a comprehensive model is presented based on the assumption that the surface redox couple IrO$_3$/IrO$_2$ is involved in both oxygen evolution and ISP oxidation.

Three reactions have been considered in this model:

(a) Electrochemical oxidation of surface IrO$_2$ to IrO$_3$ via hydroxyl radicals according to the global reaction (8.7):

$$(IrO_2)_s + H_2O \underset{k_{-1}^e}{\overset{k_1^e}{\rightleftarrows}} (IrO_3)_s + 2H^+ + 2e^- \tag{8.7}$$
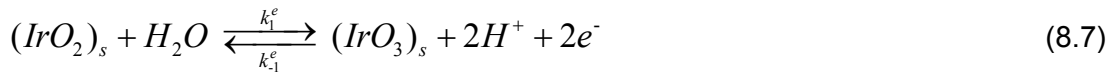
b) Chemical oxidation of the adsorbed isopropanol (ISP) to acetone by the electrogenerated IrO$_3$ according to the global reaction (8.8):

$$(IrO_3)_s + (CH_3CHOHCH_3)_{ad} \xrightarrow{k_c} (IrO_2)_s + (CH_3COCH_3)_{ad} + H_2O \tag{8.8}$$
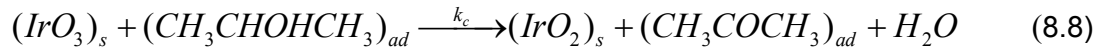
c) Oxygen evolution via decomposition of surface IrO$_3$ according to the global reaction (8.9):

$$(IrO_3)_s \xrightarrow{k_d} (IrO_2)_s + 1/2 O_2 \tag{8.9}$$

Both reactions (8.8) and (8.9) have been considered to be heterogeneous chemical reactions regenerating the reduced state (IrO$_2$) at the surface of the electrode.

The rate of IrO$_3$ electrogeneration (reaction (8.7)) is given by (equation (8.10)):

$$r_{IrO_3} = \frac{j}{nF} = \gamma_{3D} k_1^e \Gamma_0 (1 - \Theta) - \gamma_{3D} k_{-1}^e \Gamma_0 \Theta \tag{8.10}$$

and the corresponding current density is given by (equation (8.11)):

$$j = \gamma_{3D} nF \Gamma_0 \left[k_1^e (1 - \Theta) - k_{-1}^e \Theta \right] \tag{8.11}$$

with the three dimensional roughness factor γ_{3D} [-] defined by:

$$\gamma_{3D} = \frac{A_w}{A_g} \tag{3.1}$$

where: j is the current density (relative to the geometric area) [A/cm²], Γ_0 is the density of IrO$_2$ active surface sites [mol/cm²], Θ is the fraction of surface sites covered by IrO$_3$ [-], k_1^e and k_{-1}^e are the electrochemical rate constant for the forward and the backward reactions (reaction (8.7)), respectively [1/s], n is the number of involved electrons in reaction (8.7) (n=2), A_w is the real (wetted) electrode surface area [cm²] and A_g is the geometric (projected) electrode surface area [cm²].

The rate of the chemical oxidation of ISP by IrO$_3$ (reaction (8.8)) is given by equation (8.12):

$$r_{oxid.} = \gamma_{3D} k_c \Gamma_0 \Theta \cdot C_{ISP}^{ad} \tag{8.12}$$

where: k_c is the chemical rate constant [cm³/mols] and C_{ISP}^{ad} is the concentration of the adsorbed ISP at the surface of the electrode [mol/cm³].

The rate of decomposition of surface IrO$_3$ to oxygen (given by the reaction (8.9)) is shown in equation (8.13):

$$r_{dec.} = \gamma_{3D} k_d \Gamma_0 \Theta \tag{8.13}$$

where: k_d is the decomposition rate constant of the higher oxide IrO$_3$ [1/s].

Considering steady-state conditions, the fraction of surface sites covered by IrO$_3$ is obtained (equation (8.14)):

$$r_{IrO_3} = r_{oxid.} + r_{dec.}$$

$$k_1^e (1 - \Theta) - k_{-1}^e \Theta = k_c \Theta \cdot C_{ISP}^{ad} + k_d \Theta$$

$$\Theta = \frac{k_1^e}{k_1^e + k_{-1}^e + k_c C_{ISP}^{ad} + k_d}$$ (8.14)

From Equations (8.11) and (8.14), and considering that $C_{ISP}^{ad} = C_{ISP}^{bulk}$, $n = 2$, and neglecting the side reaction of O_2 evolution ($k_d = 0$), we obtain:

$$j = 2\gamma_{3D} F k_1^e \Gamma_0 \left[\frac{k_c C_{ISP}^{bulk}}{k_1^e + k_{-1}^e + k_c C_{ISP}^{bulk}} \right]$$

Since it is difficult to determine from this relation the kinetic parameters of the model, it has been taken the reciprocal of both sides of this relation to give (equation (8.15)):

$$\frac{1}{j} = \frac{1}{2\gamma_{3D} F k_1^e \Gamma_0} + \frac{k_1^e + k_{-1}^e}{2\gamma_{3D} F k_1^e \Gamma_0 k_c C_{ISP}^{bulk}}$$ (8.15)

According to this equation, the plot of the inverse of current density ($1/j$) against the inverse of ISP bulk concentration ($1/C_{ISP}^{bulk}$) should be linear.

As a matter of fact, from the data of Figure 8.2, the plot of ($1/j$) against ($1/C_{ISP}^{bulk}$) gives straight lines for all the investigated IrO_2 loadings (Figure 8.3). From this figure, the intersection on the ($1/j$) axis will give $1/2\gamma_{3D} F k_1^e \Gamma_0$, according to Equation (8.15).
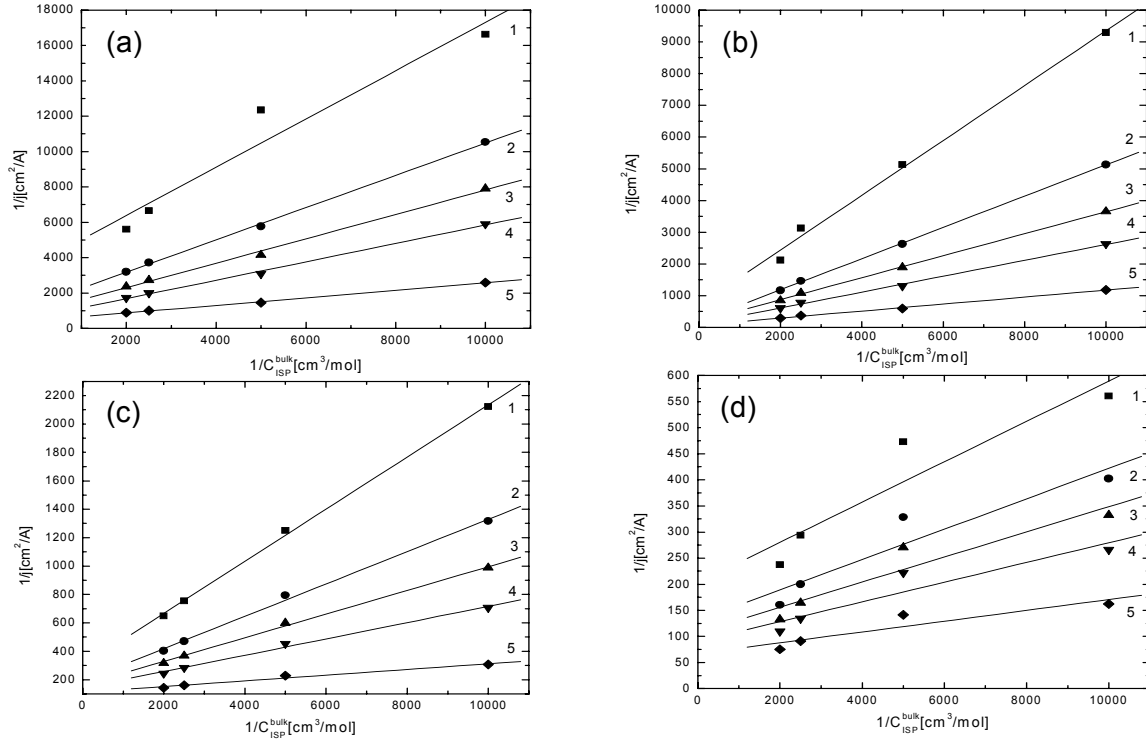
Figure 8.3: Inverse of the current density ($1/j$) plotted vs. the inverse of isopropanol concentration ($1/C_{ISP}^{bulk}$) for different IrO₂ loadings: (a) $E_{0.11}$, (b) $E_{0.28}$, (c) $E_{1.81}$, and (d) $E_{4.07}$, and for different potentials: 1: 0.77, 2: 0.79, 3: 0.8, 4: 0.81, 5: 0.83 V/MSE. Supporting electrolyte: 1M HClO₄. T=25°C.

In order to calculate the apparent standard rate constant $(k_1^{e,o})_{app}$ (defined by equation (8.16)) of the electrochemical reaction [mol/cm²s] for all investigated loadings, the logarithm of the intersections, in Figure 8.3, have been plotted against the overpotential (considering E^0 = 0.66V/MSE for reaction (8.7)) and are given in Figure 8.4.

$$(k_1^{e,o})_{app} = \gamma_{3D} k_1^{e,o} \Gamma_0 \tag{8.16}$$
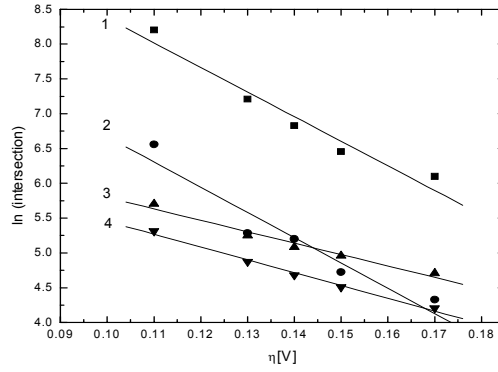
Figure 8.4: Intersections of the straight lines reported in Figure 8.3 plotted as a function of the overpotential η for different loadings: 1: $E_{0.11}$, 2: $E_{0.28}$, 3: $E_{1.81}$, and 4: $E_{4.07}$.

According to equation (8.17), from the intersection of the straight lines in Figure 8.4, the apparent standard rate constants $(k_1^{e,o})_{app}$ have been determined for different IrO$_2$ loadings and are shown in Table 8.1.

$$k_1^e = k_1^{e,0} \exp\left(\frac{\alpha n F}{RT} \eta \right) \tag{8.17}$$

where: n, F, R, T have their usual meaning.

Working at high overpotentials (>200mV), Equation (8.15) is transformed to equation (8.18).

$$\frac{1}{j} = \frac{1}{2\gamma_{3D}Fk_1^e\Gamma_0} + \frac{1}{2F(k_c)_{app}} \cdot \frac{1}{C_{ISP}} \tag{8.18}$$

where: $(k_c)_{app}$ is the apparent rate constant of reaction (8.8) defined by :

$$(k_c)_{app} = \gamma_{3D}\Gamma_0 k_c \tag{8.19}$$

From the $I - \eta$ curves of Figure 8.2 corrected for the background current due to oxygen evolution, the inverse of the current density $(1/j)$ has been plotted against the inverse of ISP concentration $(1/C_{ISP}^{bulk})$, and this for the different investigated IrO$_2$ loadings (Figure 8.5).
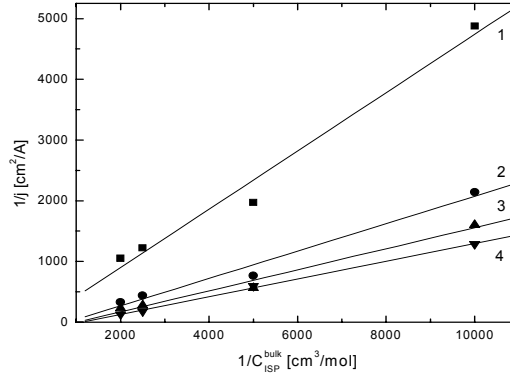
Figure 8.5: Inverse of the current density ($1/j$) corrected for O_2 evolution plotted as a function of the inverse of the isopropanol concentration ($1/C_{ISP}^{bulk}$) obtained at different IrO₂ loadings: 1: $E_{0.11}$, 2: $E_{0.28}$, 3: $E_{1.81}$, and 4: $E_{4.07}$. T= 25°C.

From the slope of the obtained straight lines, the apparent rate constants $(k_c)_{app}$ for the reaction (8.8) has been calculated. The obtained $(k_c)_{app}$ values for different IrO₂ loadings have been given on Table 8.1.

For the estimation of the effectiveness factor, E_f, the same approach used for the O_2 and Cl_2 evolution reactions (see chapter 7, sections 7.3.1 and 7.3.2, respectively) has as well been used here. The lowest IrO₂ loading, $E_{0.11}$, has been used as a reference for the determination of the relative effectiveness factor, $E_f^{rel.}$, for both the electrochemical reaction (8.7) and the chemical reaction (8.8) using equations (8.20) and (8.21), respectively:

$$(E_f^{rel.})_{elect.} = \frac{(k_1^{e,0})_{app} / m_{sp}}{(k_1^{e,0})_{app}^{ref} / m_{sp}^{ref}} \tag{8.20}$$

and

$$(E_f^{rel.})_{chem.} = \frac{(k_c)_{app} / m_{sp}}{(k_c)_{app}^{ref} / m_{sp}^{ref}} \tag{8.21}$$

where: $(k_1^{e,0})_{app}^{ref}$ and $(k_c)_{app}^{ref}$ are the apparent electrochemical and chemical rate constants for the lowest specific IrO₂ loading ($E_{0.11}$), m_{sp}^{ref}, taken as reference.

The obtained relative effectiveness factors, $E_f^{rel.}$, for both reactions (8.7) and (8.8) are given in Table 8.1.

Table 8.1: Calculated relative effectiveness factor, $E_f^{rel.}$, for reactions (8.7) and (8.8) using Equations (8.20) and (8.21).

m_{sp} [mg/cm²]	0.11	0.28	1.81	4.07
$(k_1^{e,0})_{app}$ [mol/cm²s]	3.5×10^{-11}	1.7×10^{-10}	3.1×10^{-9}	3.5×10^{-9}
$(k_c)_{app}$ [cm/s]	1.1×10^{-5}	2.3×10^{-5}	3.0×10^{-5}	3.5×10^{-5}
$(E_f^{rel.})_{elect.}$ [-]	1.00*	1.9	5.3	2.7
$(E_f^{rel.})_{chem.}$ [-]	1.00*	0.83	0.16	0.09

* Taken as a reference.

This table shows that the relative effectiveness factor for the electrochemical reaction (8.7), is in the order of unity and no correlation with the loading can be established. However, the relative effectiveness factor for the chemical reaction (8.8), decreases with increasing loading. This is expected, as we are dealing with an electrochemical reaction in which water is the electroactive species (present in large excess), while for the chemical reaction, isopropanol has to diffuse through the coating leading to a concentration gradient.

Unfortunately due to the complexity of this system, the theoretical effectiveness factor, E_f, for these reactions, has not been calculated.

8.4   Conclusions

This chapter concludes in:

- For all investigated IrO_2 electrodes, the overpotential of water discharge decreases as the concentration of isopropanol increases,
- A model was proposed based on three main reactions: Electrochemical IrO_2 oxidation to IrO_3, chemical oxidation of isopropanol via IrO_3, and chemical decomposition of IrO_3 to IrO_2 (reactions (8.7)-(8.9)),

- From the $1/j$ versus $1/C_{ISP}^{bulk}$ plots, the kinetic parameters of the system have been determined,

- The relative effectiveness factor for the electrochemical reaction (8.7) is in the order of unity and seems not to correlate with the loading, while the relative effectiveness factor for the chemical reaction (8.8), shows a decreasing correlation with the loading.

8.5 References

1. S. Trasatti, W. E. O'Grady, in *Advances in Electrochemistry and Electrochemical Engineering*, H. Gerischer and C. W. Tobias, Editors, John Wiley and Sons, New York, 1981, 177-261.

2. F. Beck, *Ber. Bunsenges, Phys. Chem.*, 1973, **77**, 353.

3. F. Beck and H. Schulz, *Electrochim. Acta*, 1984, **29**, 1569-1579.

4. E. Lodowicks and F. Beck, *Chem. Eng. & Tech.*, 1994, **17**, 338-347.

5. Ch. Comninellis and E. Plattner, *Chimia*, 1988, **42**, 250.

6. Ch. Comninellis and C. Pulgarin, *J. Appl. Electrochem.*, 1991, **21**, 703-708.

7. G. Foti, D. Gandini, Ch. Comninellis, A. Perret, and W. Haenni, *Electrochem. Solid-State Lett.*, 1999, **2**, 228-230.

8. G. Foti and Ch. Comninellis, in *Modern Aspects of Electrochemistry*, R. White, B. E. Conway and C.G. Vayenas, Editors, Vol. 37, Kluwer Academic/Plenum Publishers, New York, 2004, 87.

9. G. Foti, D. Gandini and Ch. Comninellis, in *Current Topics in Electrochemistry*, Vol. 5, Research Trends, Trivandrum, 1997, 71.

10. B. Marselli, J. Garcia-Gomez, P. A. Michaud, M. A. Rodrigo and Ch. Comninellis, *J. Electrochem. Soc.*, 2003, **150**, D79-D83.

Chapter 9

General discussion

This chapter will give the reader a general overview of the presented work and highlight the main results and achievements regarding the estimation of the effectiveness factor, E_f, of the DSA® (Ti/IrO$_2$) electrodes, i.e. the fraction of the active electrode surface which indeed participates in the electrochemical reactions under investigation of Fe^{3+}/Fe^{2+}, O$_2$ and Cl$_2$ evolution, and the oxidation of isopropanol.

The activity of dimensionally stable anodes (DSA®) depends mainly on two effects: electronic and geometric. Their differentiation is very important for fundamental research and needs to be evaluated. In order to quantify the geometric effect, it is useful to introduce the notion of the effectiveness factor, E_f.

In fields like heavy metals recovery using 3D electrodes [1] or in heterogeneous catalysis [2], the effectiveness factor has been widely used. On the other hand, with this work, it is the first time that the effectiveness factor has been adopted and adapted in electrocatalysis for studying its influence on the loading of DSA® (Ti/IrO$_2$) electrodes and on the kinetics of the investigated reactions. Consequently, this work focuses on the estimation of the effectiveness factor for varying reactions like: (a) Fe^{3+}/Fe^{2+} (fast reaction), (b) O$_2$ and Cl$_2$ evolution (slow reactions), and (c) isopropanol oxidation (complex reaction involving redox catalysis).

(a) Estimation of the effectiveness factor, E_f, for the Fe^{3+}/Fe^{2+} redox couple using voltammetry

Voltammetric determination of the effectiveness factor, E_f, of Ti/IrO_2 electrodes of different IrO_2 loading has been attempted using the Fe^{3+}/Fe^{2+} redox couple as a fast probe reaction.

Accompanied issues due to background current (voltammetric charge) and uncompensated electrolyte resistance have been elucidated. Additionally, the effect of the uncompensated resistance, R_u, on the experimentally obtained standard rate constant, k^0, and the effectiveness factor, E_f, has been evaluated. It was found that the experimental determination of the exchange current density, j_0, is so much sensitive to the correction of the uncompensated electrolyte resistance, R_u, that the estimation of the effectiveness (through exchange current densities) by this method is not reliable. Nevertheless, both CV and LSV measurements suggested qualitatively that only the geometric surface area is involved when using the Fe^{3+}/Fe^{2+} redox couple.

(b) Estimation of the effectiveness factor, E_f, for the Fe^{3+}/Fe^{2+} redox couple using Ti/IrO_2 rotating disk electrodes (RDE)

Also in rotating disk electrode (RDE) experiments, the Fe^{3+}/Fe^{2+} redox couple has been used as a probe reaction in order to evaluate the effectiveness factor, E_f, of this redox couple, and to compare the values with the prediction (according to the analytical approach given in section 3.2), using different specific IrO_2 loadings, m_{sp}, (see Table 9.1). The main advantage of this investigation, using RDE, is that low currents are involved and the uncompensated resistance can easily be calculated.

Table 9.1: Comparison of the predicted and experimental effectiveness factors for various IrO_2 loadings.

		m_{sp} [mg IrO_2/cm^2]			
		0.62	1.97	2.46	4.92
E_f [-]	**Predicted**	0.68	0.26	0.20	0.10
	Experimental	0.014	0.005	0.004	0.002

Table 9.1 shows an enormous difference between the predicted and the experimental effectiveness factor. This difference should be related to the main assumption of the analytical approach, i.e. that the concentration of the electroactive species (Fe^{3+} and Fe^{2+}) is invariant inside the coating. As a matter of fact, as the charge transfer reaction of this redox couple is very fast (j_0 = 52mA/cm^2), a sharp decrease of Fe^{3+} and Fe^{2+} concentration within the pores is expected during polarization.

(c) Estimation of the relative effectiveness factor, $E_f^{rel.}$, for the O_2 and Cl_2 evolution reactions

In this section, the O_2 and Cl_2 evolution reactions have been considered for the estimation of the relative effectiveness factor, $E_f^{rel.}$, using different IrO_2 loadings. Concerning the O_2 evolution reaction, the assumption made by the analytical approach (invariant concentration of the electroactive species within the coating) is applicable, as water present in excess within the coating is involved in the reaction.

Table 9.2: Relative predicted and experimental effectiveness factor, $E_f^{rel.}$, for the O_2 evolution reaction and various IrO_2 loadings.

Electrodes	m_{sp} [mg/cm²]	Predicted $E_f^{rel.}$ [-]	Experimental $E_f^{rel.}$ [-]
$E_{0.11}$	0.11	1.00*	1.00*
$E_{0.28}$	0.28	1.00	0.81
$E_{1.81}$	1.81	1.00	1.07
$E_{4.07}$	4.07	1.00	1.21

* The predicted effectiveness factor is obtained with Equation (3.32), and referred to the lowest loading to give $E_f^{rel.}$. The relative experimental effectiveness factor, $E_f^{rel.}$, has been calculated using equation: $E_f^{rel.} = \dfrac{(j_0)_{3D} \, / \, m_{sp}}{(j_0)_{3D}^{ref} \, / \, m_{sp}^{ref}}$, where: $(j_0)_{3D}^{ref}$ and m_{sp}^{ref} are, respectively, the exchange current density and the specific IrO_2 loading of the 3D electrode of lowest loading ($E_{0.11}$) taken as a reference.

Table 9.2 shows that the effectiveness factors, $E_f^{rel.}$, for both the relative experimental and the theoretical values are close to the unity showing that almost all the totality of the active surface of the coating participates in the reaction, and this is mostly due to two reasons: The O_2/H_2O reaction is slow and there is no concentration gradient within the coating as water is the reactive species (present in excess) inside the coating.

The same approach as that given for the O_2 evolution, has been used for the estimation of the relative effectiveness factor, $E_f^{rel.}$, for the Cl_2 evolution reaction.

Table 9.3: Relative predicted and experimental effectiveness factor, $E_f^{rel.}$, for the Cl_2 evolution reaction and various IrO_2 loadings.

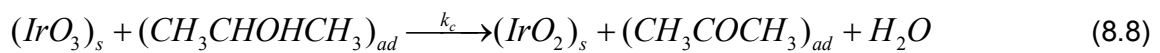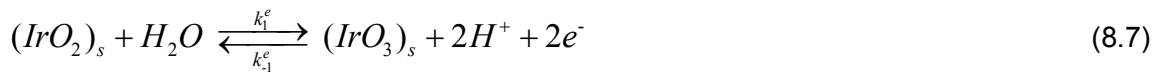| Electrodes	m_{sp} [mg/cm²]	Predicted $E_f^{rel.}$ [-]	Experimental $E_f^{rel.}$ [-]
$E_{0.11}$	0.11	1.00*	1.00*
$E_{0.28}$	0.28	1.00	0.98
$E_{1.81}$	1.81	0.97	0.64
$E_{4.07}$	4.07	0.86	0.59

* As seen in Table 9.2, the predicted effectiveness factor is also obtained with Equation (3.32), and referred to the lowest loading to give $E_f^{rel.}$. The relative experimental effectiveness factor, $E_f^{rel.}$, has been calculated using the same equation shown in Table 9.2, and the electrode $E_{0.11}$ was taken as a reference.

Table 9.3 shows that for both the relative experimental and predicted effectiveness factor diminish with the IrO_2 loading as the Cl_2/Cl^- redox couple has intermediate kinetics between that of the O_2/H_2O and the Fe^{3+}/Fe^{2+} redox couples. Moreover, the experimental values are close to the predicted behaviour.

(d) Estimation of the relative effectiveness factor, $E_f^{rel.}$, for the isopropanol oxidation

A model has been proposed based on three main reactions: Electrochemical IrO_2 oxidation to IrO_3 (see reaction (8.7)), chemical oxidation of isopropanol via IrO_3 (see reaction (8.8)) and chemical decomposition of IrO_3 to IO_2 (see reaction (8.9)).

$$(IrO_2)_s + H_2O \underset{k_{-1}^e}{\overset{k_1^e}{\rightleftarrows}} (IrO_3)_s + 2H^+ + 2e^- \tag{8.7}$$

$$(IrO_3)_s + (CH_3CHOHCH_3)_{ad} \overset{k_c}{\longrightarrow} (IrO_2)_s + (CH_3COCH_3)_{ad} + H_2O \tag{8.8}$$

$$(IrO_3)_s \overset{k_d}{\longrightarrow} (IrO_2)_s + 1/2O_2 \tag{8.9}$$

Using Equations (8.20)-(8.21), the relative effectiveness factor, $E_f^{rel.}$, (taking the lowest loading as reference, $E_{0.11}$) for both the electrochemical (8.7) and the chemical (8.8) reaction has been evaluated for different IrO_2 loading and given in Table 9.4.

$$(E_f^{rel.})_{elect.} = \frac{(k_1^{e,0})_{app} / m_{sp}}{(k_1^{e,0})_{app}^{ref} / m_{sp}^{ref}} \tag{8.20}$$

and

$$(E_f^{rel.})_{chem.} = \frac{(k_c)_{app} / m_{sp}}{(k_c)_{app}^{ref} / m_{sp}^{ref}} \qquad (8.21)$$

where: $(k_1^{e,0})_{app}^{ref}$ and $(k_c)_{app}^{ref}$ are the electrochemical and chemical apparent rate constants for the lowest IrO$_2$ loading ($E_{0.11}$), taken as reference (m_{sp}^{ref}).

Table 9.4: Calculated relative effectiveness factor, $E_f^{rel.}$, for reactions (8.7) and (8.8) using Equations (8.20) and (8.21) for various IrO$_2$ loadings.

Electrodes	$E_{0.11}$	$E_{0.28}$	$E_{1.81}$	$E_{4.07}$
m_{sp} [mg/cm^2]	0.11	0.28	1.81	4.07
$(k_1^{e,0})_{app}$ [mol/cm^{2}s]	3.5×10^{-11}	1.7×10^{-10}	3.1×10^{-9}	3.5×10^{-9}
$(k_c)_{app}$ [cm/s]	1.1×10^{-5}	2.3×10^{-5}	3.0×10^{-5}	3.5×10^{-5}
$(E_f^{rel.})_{elect.}$ [-]	1.00	1.9	5.3	2.7
$(E_f^{rel.})_{chem.}$ [-]	1.00	0.83	0.16	0.09

Table 9.4 shows that the relative effectiveness factor for the electrochemical reaction, (8.7) is in the order of unity and no correlation with the loading is found, whereas the relative effectiveness factor for the chemical reaction (8.8), decreases with increasing loading. The latter is expected as we are dealing with an electrochemical reaction in which water is the electroactive species (present in large excess). Concerning the chemical reaction, having isopropanol as reactant which has to diffuse through the coating, a concentration gradient is built up. Unluckily, due to the complexity of this system, no prediction of the effectiveness factor, E_f, for any of these two reactions, could be made.

References

1. F. Coeuret, D. Hutin, A. Gaunand, *J. Appl. Electrochem.*, 1976, **6**, 417.
2. O. Levenspiel, *Chemical Reaction Engineering*, Wiley Eastern Limited, 2nd. Edition, New Delhi, 1972, 473.

Chapter 10

Perspectives

In the previous chapters analytical approaches have been used for the evaluation of the effectiveness factor of the IrO_2 coating. The obtained results, compared to the predicted values, have demonstrated the limitations of these simplified approaches. This is mainly due to the simplifications inherent to the analytical solutions.

Numerical simulation is a very powerful technique which gives very useful information on the behavior of porous electrodes.

In the last chapters, some preliminary results are given in order to demonstrate the feasibility of the numerical approach.

10.1 Modelling of the porous IrO_2 coating using a numerical approach

A schematic representation of the IrO_2 coating is shown in Figure 10.1
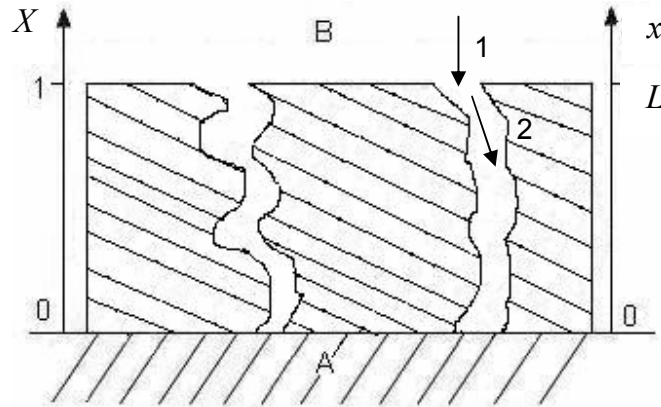
Figure 10.1: Schematic representation of the porous IrO$_2$ coating with thickness L, and dimensionless distance $X = x/L$. 1: semi-infinite diffusion (external diffusion), 2: diffusion within the coating (pore diffusion). (A) Ti substrate and (B) electrolyte.

The coating is considered as a porous medium with thickness, L [cm], tortuosity, χ [-], and volume specific pore surface area, a [1/cm]. The latter is defined as $a = A_p / L \cdot A_g$ where A_p is the internal pore surface area [cm^2] and A_g is the geometric area [cm^2].

This coating is characterized by the dimensionless parameter:

$$\mu = a \cdot L \tag{10.1}$$

A simple one-electron transfer reaction (10.2) and the Butler-Volmer equation (10.3) have been considered:

$$Ox + e^- \rightleftharpoons Red \tag{10.2}$$

$$j = j_0 (C_{red} e^{(1-\alpha)p} - C_{ox} e^{-\alpha p}) \tag{10.3}$$

where:

j : Current density, [A/cm^2],

j_0 : Exchange current density of reaction (10.2), [A/cm^2],

α : Transfer coefficient, [-],

p : Dimensionless potential, $p = \dfrac{F}{RT}\eta$, [-],

$C_{ox} = \dfrac{c_{ox}}{c_{ox}^*}$ and $C_{red} = \dfrac{c_{red}}{c_{red}^*}$: Dimensionless concentrations, [-], with: surface concentration

(c) relative to the bulk concentration (c^*), [mol/cm³].

According to this model, the current at a given overpotential has two contributions (see Figure 10.1). One contribution is coming from the semi-infinite diffusion of the electroactive species towards the planar electrode surface (external film diffusion), and the other one comes from the diffusion of electroactive species within the coating (internal pore diffusion). In order to describe this system, the dimensionless parameters λ and γ given in Equations (3.66) and (3.67) have been modified to give:

(a) The dimensionless parameter λ' is related to the charge-transfer reaction and the diffusion within the coating.

$$\lambda' = ak^0 \frac{L^2}{D_{eff}} = \frac{e^{\alpha p}}{\lambda} \tag{10.4}$$

where: k^0 is the standard electrochemical rate constant [cm/s] and $D_{eff} = \dfrac{D}{\chi^2}$ [cm²/s] is the effective diffusion coefficient inside the porous electrode of tortuosity χ .

(b) The dimensionless parameter γ is related to the voltammetric measurements and the internal diffusion.

$$\gamma = \frac{\Delta E \cdot D_{eff}}{\upsilon \cdot L^2} \tag{3.67}$$

Considering a reversible redox couple:

$$\gamma = \frac{RT \cdot D_{eff}}{F\upsilon \cdot L^2} \tag{10.5}$$

Diffusion of the electroactive species within the coating is described by the dimensionless Fick's second law together with an electrochemical reaction in one dimension (at $0 \le X \le 1$).

$$\frac{\partial C_{ox}}{\partial T} = \frac{1}{\chi^2} \frac{\partial^2 C_{ox}}{\partial X^2} - \lambda' \left(C_{ox} e^{-\alpha p} - C_{red} e^{(1-\alpha)p} \right)$$

$$\tag{10.6}$$

$$\frac{\partial C_{red}}{\partial T} = \frac{1}{\chi^2} \frac{\partial^2 C_{red}}{\partial X^2} + \lambda' \left(C_{ox} e^{-\alpha p} - C_{red} e^{(1-\alpha)p} \right)$$

where: T is the dimensionless time: $T = t/\tau$ and τ is the typical time constant: $\tau = L^2/D$.

The equations to solve in the outer part of the electrode in the dimensionless form are:

$$\frac{\partial C_{ox}}{\partial T} = \frac{\partial^2 C_{ox}}{\partial X^2}$$

$$\text{At: } X > 1 \tag{10.7}$$

$$\frac{\partial C_{red}}{\partial T} = \frac{\partial^2 C_{red}}{\partial X^2}$$

The initial and boundary dimensionless conditions are:

$$T = 0, \ 0 \le X \le 1 : C_{ox} = 1, \ C_{red} = 1,$$

$$T \ge 0, \ X = \infty : C_{ox} = 1, \ C_{red} = 1, \tag{10.8}$$

$$T > 0, \ X = 0 : \frac{\partial C_{red}}{\partial X} = 0, \ \frac{\partial C_{ox}}{\partial X} = 0$$

At the external electrode-electrolyte interface, the boundary condition is:

$$T > 0, \ X = 1: \begin{cases} \dfrac{j^{ext}}{F} = \left(D_{red} \left. \dfrac{\partial C_{red}}{\partial X} \right|_{X \to 1, (X>1)} - D_{eff}^{red} \left. \dfrac{\partial C_{red}}{\partial X} \right|_{X \to 1, (X<1)} \right) \dfrac{c_{red}^*}{L} \\[4mm] \dfrac{j^{ext}}{F} = -\left(D_{ox} \left. \dfrac{\partial C_{ox}}{\partial X} \right|_{X \to 1, (X>1)} - D_{eff}^{ox} \left. \dfrac{\partial C_{ox}}{\partial X} \right|_{X \to 1, (X<1)} \right) \dfrac{c_{ox}^*}{L} \end{cases}$$

(10.9)

The dimensional total current density in the system is given by two contributions:

One contribution is that produced inside the porous electrode (j^{int}) of thickness L:

$$j^{int}(t) = F \int_0^L a k^0 \left[c_{red}(x,t) e^{(1-\alpha)\frac{F}{RT}\eta} - c_{ox}(x,t) e^{-\alpha\frac{F}{RT}\eta} \right] dx$$

(10.10)

Another contribution is produced at the external electrode-electrolyte interface, thus outside the porous electrode (j^{ext}):

$$j^{ext}(t) = F k^0 \left[c_{red}(L) e^{(1-\alpha)\frac{F}{RT}\eta} - c_{ox}(L) e^{-\alpha\frac{F}{RT}\eta} \right]$$

(10.11)

Finally, the total current density (j^{tot}) at equimolar electrolyte concentration ($c_{red}^* = c_{ox}^* = c*$) can be written as:

$$j^{tot} = F k^0 c * \left(G^{ext} + \mu G^{int} \right) = F k^0 c * (G^{ext} + aL G^{int})$$

(10.12)

where, in order to simplify the numerical calculations, the current density is presented in term of dimensionless parameters (G^{ext}, G^{int}, and G^{tot}):

$$G^{ext} = C_{red}(1) e^{(1-\alpha)p} - C_{ox}(1) e^{-\alpha p}$$

(10.13)

$$G^{int} = \int_0^1 (C_{red}(X)e^{(1-\alpha)p} - C_{ox}(X)e^{-\alpha p})dX \qquad (10.14)$$

$$G^{tot} = G^{ext} + aLG^{int} = G^{ext} + \mu G^{int} \qquad (10.15)$$

For solving Equations (10.6) and (10.7), numerical methods based on explicit finite difference methods are employed. To guarantee stable integrations in the algorithm (see appendix), the following conditions were respected [1]:

$$\frac{\Delta T}{(\Delta X)^2} < 0.5$$

$$X_{max} \cong 6\sqrt{T_{max}}$$

with ΔT and ΔX, the time and space discretization steps.

Figure 10.1 shows the dimensionless total current (G^{tot}) as a function of the dimensionless potential p at fixed values of $\chi = 1$ and $\gamma = 1$, assuming $D_{eff}^{ox} = D_{eff}^{red} = D_{eff}$. What is changed is the ratio between the internal diffusion time and the electrochemical kinetics (the parameter λ', Equation (10.4)), and calculations were made at two different values of parameter μ. In case of uniform porosity, μ is a measure of loading. For instance, with straight ($\chi = 1$) cylindrical pores of diameter d, the parameter μ equals $L \cdot \pi \cdot N_p \cdot d$, where N_p is the number of pores per cm² external geometric surface.
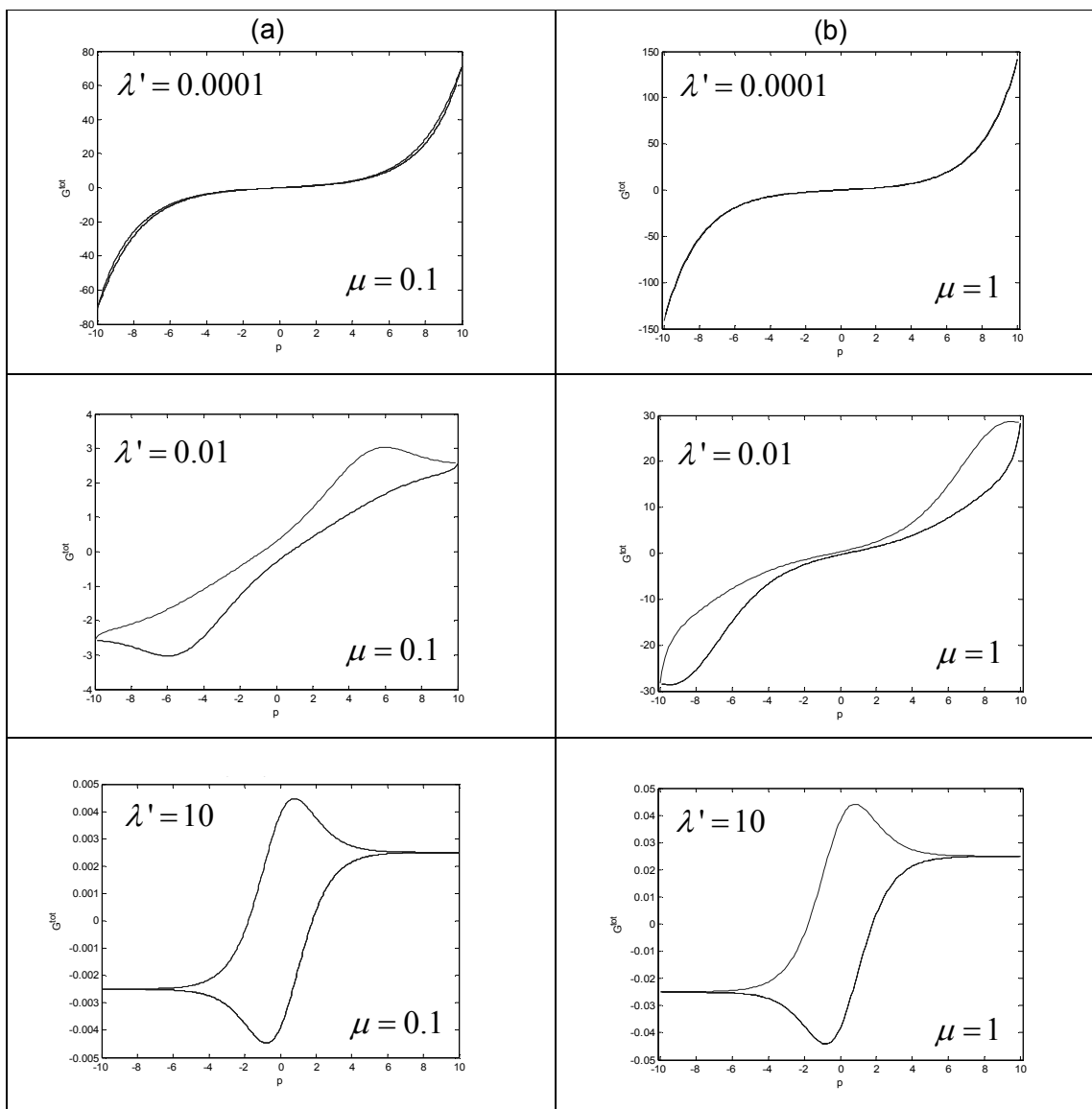
Figure 10.1: Variation of the dimensionless current (G^{tot}) as a function of the dimensionless potential p at fixed values of γ ($\gamma = 1$) and χ ($\chi = 1$) and for various values of λ'. (a) $\mu = 0.1$ and (b) $\mu = 1$.

Two extreme cases were simulated:

1st case: $\lambda' \ll 1$: (see Figure 10.1 first and second rows):

In this case, diffusion is much faster than the electrochemical reaction. Diffusion inside the pores is not the rate limiting step. This means that, since diffusion is fast, all the electroactive species consumed are immediately replaced by new ones. Under these circumstances, the quasi-totality of the wetted 3D surface of the coating is involved in the voltammetric measurements.

2nd case: $\lambda' \gg 1$; (see Figure 10.1 third row):

In this case, diffusion inside the pores is slower than the electrochemical reaction. Diffusion is the rate limiting step. This means that since there is slow diffusion, electroactive species are replaced only slowly. In this case the electrode behaves as a capacitor that charges and discharges. In addition, with higher λ', the reaction seems to be more reversible (peaks almost in front of each other), and the peaks are better distinguished. In a recent paper the decrease in peak separation in porous coating has been attributed to the change in the diffusion regime [2].

10.2 Conclusions

Considering a two-step model, external diffusion and pore diffusion, the numerical approach has shown that under certain conditions (high λ' values), the voltammetric peak-to-peak potential separation of the investigated redox couple decreases. This is not due to any electrocatalytic effect but it is certainly related to the fact that under these conditions, the purely semi-infinite diffusion model is no longer valid. In fact, it is expected that if the coating thickness L is smaller than the diffusion layer thickness for a given experimental time (t), that is:

$$L \ll \sqrt{D_{eff}t} \quad \text{or} \quad \gamma \gg 1,$$

mass transfer within the coating can be neglected. Under these conditions, the system behaves like a capacitor, i.e. the peak current, I_p, is proportional to scan rate.

10.3 References

1. D. Britz, in Digital Simulation in Electrochemistry, Lect. Notes, Phys., Springer-Verlag, **666**, Berlin, Heidelberg, 2005, 5-32.

2. I. Streeter, G. G. Wildgoose, L. Shao, R. G. Compton, *Sensors and Actuators B: Chemical*, 2008, in press.

Appendix. Visual C^{++} code

```cpp
//File:porous_electrode_3_regions_single_cyclogramm.cpp
//This program produces MATLAB code for ploting one graph of CV
//G=f(p) for a given combination of lambda' and miu

#include <iostream>
#include <fstream>
#include <math.h>
#include<cstdlib>
#define outFile "results.txt"
using namespace std;

const double Tf=80;        // time for the total number of cycles Tf=n*Tc
const double alpha = 0.5;
const double dt=0.0001;
const double dx=0.05;            // dx = 1/N
const int N=20;


int main()
{
ofstream out;
double lambda1=0.0001;
double lambda2=0.001;
double chi=1;
double gamma=1;
double T0=0;
double p0=-10.0;
```

```
double pf=10.0;
double T;
double p;
int j;
int n;
int points=400;
double cred[30*N+1];
double cox[30*N+1];
double tmpRed[30*N+1];
double tmpOx[30*N+1];

double R;
double Gint;
double Gext;
double G;
bool flag;



double Tc=20/gamma;          //time for one cycle

//Prepare output file
out.open(outFile);
if (out.fail())
{
    cerr<<"ERROR:Cannot open "<<outFile<<" for output."<<endl;
    out.close();
    return EXIT_FAILURE;
}



//set values of T,p,n, and flag
T=T0;
p=p0;
n=1;             //number of the current vector to be computed
flag=true;       //=> p=p0+dt;



out<<"clear; grid off; close all; hold on"<<endl;
```

```
//set initial conditions
for (int i=0;i<30*N+1;i++)
{
        cred[i]=1;
        cox[i]=1;
}
//Print the values for vectors Gi
while (T<=Tf)
{
    out<<"G=["<<endl;

        //restore value of j
        j=points;

        while (T<=n*Tc)     //subcycles
        {
                for ( i=0;i<30*N+1;i++)
                {
                        tmpRed[i]=cred[i];
                        tmpOx[i]=cox[i];
                }


                //REACTION INSIDE THE ELECTRODE of thickness L=N

                Gint=0;
                for (i=1;i<N;i++)
                {
                        R = -lambda1*(cred[i]*exp((1-alpha)*p) - cox[i]*exp(-alpha*p));
                        tmpRed[i] = tmpRed[i] + dt*(cred[i-1] -2*cred[i] +cred[i+1])/(dx*dx*chi*chi) +
R*dt;

                        tmpOx[i]   = tmpOx[i]   + dt*(cox[i-1] -2*cox[i] +cox[i+1])/(dx*dx*chi*chi) -
R*dt;

                        Gint=Gint-R*dx/lambda1;
                }
```

```
//REACTION OUTSIDE THE ELECTRODE

for (i=N+1;i<30*N;i++)
{
        tmpRed[i]=tmpRed[i] + dt*(cred[i-1]-2*cred[i]+cred[i+1])/(dx*dx);
        tmpOx[i]=tmpOx[i] + dt*(cox[i-1]-2*cox[i]+cox[i+1])/(dx*dx);
}


//REACTION AT THE SURFACE OF THE ELECTRODE

//              a11*Cred + a12*Cox =b1;
//              a21*Cred + a22*Cox =b2;
//
//Below is given algorithm for solving the system of linear equations using Cramer's
rule

        double a11 = lambda2*dx*exp((1-alpha)*p) + 1.0/(chi*chi)+1.0;
        double a12 = -lambda2*dx*exp(-alpha*p);
        double b1  = tmpRed[N+1] + tmpRed[N-1]/(chi*chi);
        double a21 = lambda2*dx*exp((1-alpha)*p);
        double a22 = -lambda2*dx*exp(-alpha*p) - 1.0 - 1.0/(chi*chi);
        double b2  = -(tmpOx[N+1] + tmpOx[N-1]/(chi*chi));


        double D = a11*a22 - a12*a21;

tmpRed[N] = (b1*a22 - b2*a12)/D;
tmpOx[N]  = (a11*b2 - a21*b1)/D;


for (i=1;i<30*N;i++)
{
        cred[i]=tmpRed[i];
        cox[i]=tmpOx[i];
}

Gext=cred[N]*exp((1-alpha)*p) - cox[N]*exp(-alpha*p);
```

```
        //Boundary conditions (first and last points)


        cred[0]=cred[1];
        cred[3*N]=1;


        cox[0]=cox[1];
        cox[3*N]=1;


        G=lambda1/lambda2*Gint+Gext;


        //Print results in the output file (each 10th point)


if (j==points)
        {
                //output the value of p and G in two columns
                out<<p<<"  "<< Gext <<"  "<< Gint <<"  "<< G << endl;


                j=0;
        }
        j++;


        if (flag==true) //when the flag is "true" increase p from -10 to 10
                p=p+gamma*dt;
        else        // when flag is "false" decrease p from 10 to -10
                p=p-gamma*dt;


        T=T+dt;


}


        out<<"];"<<endl;
        flag=!(flag);    //negate (invert ) the value of flag


        if (n>1)        //initial solution is not stable and will not be plotted
        {
   out<<"hold on; figure(1); xlim([-10 10]); box on;"<<endl;
                out<<"plot(G(:,1),G(:,2),'-');"<<endl;
                out<<"xlabel('p');"<<endl;
```

```
out<<"ylabel('G^{ext}');"<<endl;
out<<"title('lambda1"<<lambda1<<", lambda2="<<lambda2<<", \\chi="<< chi <<
", gamma=" << gamma << "');"<<endl;


out<<"hold on; figure(2); xlim([-10 10]); box on;"<<endl;
out<<"plot(G(:,1),G(:,3),'-');"<<endl;
out<<"xlabel('p');"<<endl;
out<<"ylabel('G^{int}');"<<endl;
out<<"title('lambda1="<<lambda1<<", lambda2="<<lambda2<<", \\chi="<< chi <<
", gamma=" << gamma << "');"<<endl;


out<<"hold on; figure(3); xlim([-10 10]); box on;"<<endl;
out<<"plot(G(:,1),G(:,4),'-');"<<endl;
out<<"xlabel('p');"<<endl;
out<<"ylabel('G^{tot}');"<<endl;
out<<"title('lambda1="<<lambda1<<", lambda2="<<lambda2<<", \\chi="<< chi <<
", gamma=" << gamma << "');"<<endl;
}
cout<<"G"<<n<<"computed"<<endl;


n++;
}


cout <<"Open file results.txt"<<endl;
return 0;
}
```

Curriculum Vitae

Erika Herrera Calderon

Single · born 11/14/1978 · Mexican

erika_herrera_calderon@hotmail.com

Education

2005-2008 · PhD thesis in Electrochemistry · *"Ecole Polytechnique Fédérale de Lausanne (EPFL)"* Switzerland.

2002-2004 · MSc. in Materials and Process Engineering (Electrochemistry) · *"Institut National Polytechnique de Grenoble (INPG)": "Ecole Nationale Supérieure d'Electrochimie et Electrométallurgie de Grenoble (ENSEEG)"* · France.

1996-2001 · BSc. in Chemical Engineering (Environment) · *"Institute of Technology at Aguascalientes"* · Mexico.

Professional Experience

2004- 2008 · *PhD assistant at "EPFL"* · *Switzerland*

- Practical laboratory work for EPFL students of Chemical Engineering and Criminology Science.
- Semester, master and monthly projects.

Internships

07-08.2007 · *University of Concordia at Montreal* · *Canada*

- Project related to PhD work: "Study of the relative internal and external electrochemical active surface area of porous electrodes by numerical simulation".

08-10.2004 · *Ecole Polytechnique Fédérale de Lausanne* · *Switzerland*

- Research project: "Study of intermediaries of reactions like oxalic, maleic and formic acids on a boron doped diamond electrode".

03-07.2004 · *Ecole Nationale Supérieure d'Electrochimie et Electrométallurgie de Grenoble* · *France*

- Research project: "Electrochemical reduction of carbon dioxide with a boron doped diamond electrode using molecular electrocatalysts".

06-07.2000 · *Research Centre in Electrochemistry (CIDETEQ)* · *Queretaro, Mexico*

- Science summer project: "Comparative Studies of the Techniques of Coagulation-Flocculation and Electroflotation of Textile Industrial Waste Water".

02-07.2000 · *Research Centre of Optics (CIO)* · *Aguascalientes, Mexico*

- Research BSc project: Biophysics of lasers: "The applications of infrared lasers for corneal collagen shrinkage".

08-12.2000 · *Research Centre of Optics (CIO)* · *Aguascalientes, Mexico*

- BSc. thesis project: "Formation and preparation of organometallic thin films and marking on with laser".

08-12.1999 · *Institute of Technology at Aguascalientes* · *Aguascalientes, Mexico*

- Semester research project: "Fluoride Removal from Thermal Water in Aguascalientes".

Publications

- S. Fierro, L. Ouattara, E. Herrera Calderon, Ch. Comninellis, "Influence of temperature on the charging/discharging process of IrO_2 coating deposited on p-Si substrate", *Electrochem. Comm*., 2008, **10**, 955-959.
- S. Fierro, L. Ouattara, E. Herrera Calderon, E. Passas-Lagos, H. Baltruschat, Ch. Comninellis, "Influence of formic acid oxidation on Ti/IrO_2 electrodes, in press.
- E. Herrera Calderon, S. Fierro, A. Kapalka, Ch. Comninellis, "Electrochemical oxidation of formic acid on Ti/IrO_2 and Boron Doped Diamond (BDD) electrodes", in preparation.
- E. Herrera Calderon, R. Wüthrich, P. Mandin, Ch. Comninellis, "Issues with an outer-sphere redox couple (Fe^{3+}/Fe^{2+}) using Ti/IrO_2 electrodes", in preparation.
- E. Herrera Calderon, R. Wüthrich, P. Mandin, Ch. Comninellis, "Estimation of the effectiveness factor of rotating disk Ti/IrO_2 electrodes for an outer-sphere redox couple (Fe^{3+}/Fe^{2+})", in preparation.
- E. Herrera Calderon, R. Wüthrich, P. Mandin, Ch. Comninellis, "Estimation of the effectiveness factor of Ti/IrO_2 electrodes for slow reactions (O_2 and Cl_2 evolution)", in preparation.
- E. Herrera Calderon, R. Wüthrich, P. Mandin, Ch. Comninellis, "Investigation of isopropanol oxidation on Ti/IrO_2 electrodes", in preparation.
- E. Herrera Calderon, H. Petrov Angelov, R. Wüthrich, Ph. Mandin, "Study of the Relative External Electrochemical Active Surface of Porous Electrodes by Numerical Simulation", in preparation.
- R. A. Torres-Palma, E. Herrera Calderon, J. A. Rengifo-Herrera, Ch. Pétrier, C. Pulgarin, "Comparative structure-reactivity relationship assessment for the electrochemical, sonochemical, and photocatalytical degradation of p-substituted phenols", in preparation.
- Ph. Mandin, H. Matsushima, Y. Fukunaka, R. Wüthrich, E. Herrera Calderon, D. Lincot, "One to two-phase electrolysis processes behavior under spatial conditions", in press.

Oral presentations

- E. Herrera Calderon, R. Wüthrich, Ch. Comninellis, "Electrochemical Characterization of Dimensionally Stable Anodes (DSA®)", 56th Annual Meeting of the International Society of Electrochemistry, 09.25-30.2005, Busan, Korea.
- E. Herrera Calderon, R. Wüthrich, H. Bleuler, Ch. Comninellis, "Study of DSA® deactivation", The 9th International Symposium on the Passivation of Metals and Semiconductors, and the Properties of Thin Oxide Layers, 06. 27- 07.01. 2005, Paris, France.

Posters

- E. Herrera Calderon, R. Wüthrich, Ch. Comninellis, "Do DSA® electrodes behave as microelectrodes?", 4th European Summer School on Electrochemical Engineering, 09.17-22.2006, Palic, Serbia and Montenegro.

…Posters

- R. Wüthrich, E. Herrera Calderon, Ch. Comninellis, H. Bleuler, "Micro-usinage de verre avec décharges électrochimiques", Journées d'Électrochimie, 07.05-08.2005, Saint Malo, France.
- E. Herrera Calderon, J. Medina Valtierra, T. Dascalu, "Preparation and Characterization of Organometallic Thin Films", VII Symposium of Research on Science and Technology at the University of Aguascalientes, 09.19.2000, Aguascalientes, Mexico.
- E. Herrera Calderon, A. Rodriguez Garcia, Y. Meas, "Comparative Studies of the Techniques of Coagulation-Flocculation and Electro flotation of Textile Industrial Wastewater", XV Congress on Analytical Chemistry of the University of Guanajuato, 08.16-18.2000, Guanajuato, Mexico.